# Spins in motion
## New methods for the visualization of intracranial flow

**Inauguraldissertation**

zur Erlangung der Würde eines Doktors der Philosophie
vorgelegt der
Philosophisch-Naturwissenschaftlichen Fakultät
der Universität Basel

von
**Francesco Santini**
aus Florenz, Italien

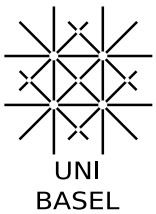


Basel, 2009

Genehmigt von der Philosophisch-Naturwissenschaftlichen Fakultät

auf Antrag von:

Prof. Dr. Klaus Scheffler
*Referent*
Prof. Dr. Jürgen Hennig
*Korreferent*

Basel, den 23.6.2009

Prof. Dr. Eberhard Parlow
*Dekan*

# Abstract

Magnetic resonance imaging has become a widely used imaging technique for diagnostic purposes, with applications in the whole human body. For many pathologies of the central nervous system, it is in fact the method of choice, due to high soft tissue contrast and the possibilities of generating images related to organ function rather than pure morphology.

In this thesis, the focus will be on methods designed to deal with a specific aspect of the central nervous system, which is the circulation of fluids (blood and cerebrospinal fluid) inside the skull. These two fluid compartments interact with each other, and a disease affecting one has good chances of affecting the other as well. This is the reason why the thesis is divided in two parts: the first part, titled ANGIOGRAPHY, is mainly related to the visualization of arteries and veins by means of angiographic sequences, and to the presentation of a novel method to enhance the visualization of datasets, by including the functional information deriving from time-resolved angiography into a single color-coded set of images. The second part, titled FLOW QUANTIFICATION, is presenting a new bSSFP-based method for 3D time-resolved acquisition of quantitative flow information. This technique can be used for blood flow assessment, but it is especially suited for the measurement of cerebrospinal fluid. In the end, preliminary clinical results from a clinical study that applies this quantification technique to flow inside the cerebral ventricles are presented.

# Publications arising from this thesis

## Journal papers

- **Santini F**, Patil S, Meckel S, Scheffler K, Wetzel SG. *Double-reference cross-correlation algorithm for separation of the arteries and veins from 3D MRA time series.* Journal of Magnetic Resonance Imaging. 2008 ;28(3):646-654.
- Meckel S, Stalder A, **Santini F**, Radü EW, Rüfenacht DA, Markl M, Wetzel SG, *In-vivo Visualization and Analysis of 3D Hemodynamics in Cerebral Aneurysms with Flow-sensitized 4D MR Imaging at 3T*, Neuroradiology. 2008 Jun;50(6):473-84.
- **Santini F**, Wetzel SG, Bock J, Markl M, *Scheffler K. Time-resolved three-dimensional phase-contrast balanced SSFP*, Magnetic Resonance in Medicine, *in press.*
- **Santini F**, Schubert T, Patil S, Meckel S, Wetzel SG, Scheffler K, Automatic reference selection for artery/vein separation from time-resolved 3D contrast-enhanced MRA datasets, Journal of Magnetic Resonance Imaging, *submitted.*

## Conference proceedings

- **Santini F**, Patil S, Meckel S, Wetzel S G, .Scheffler K, *Double-reference correlation algorithm for artery and vein separation in contrast-enhanced MR angiography*, Proceedings of the 23rd annual scientific meeting of ESMRMB, Warsaw, Poland, 2006, pp. 47-48.
- **Santini F**, Patil S, Meckel S, Scheffler K, Wetzel S G, *Artery/vein separation and fistula detection in MR angiography through double-reference correlation analysis*, Proceedings of the 31st Congress of ESNR, Geneva, Switzerland, 2006.
- **Santini F**, Wetzel S G, Scheffler K, *Automatic Reference Selection Method for Unsupervised Artery/Vein Separation in Time-Resolved Contrast-Enhanced Magnetic Resonance Angiography*, Proceedings of the Joint Annual Meeting ISMRM-ESMRMB 2007.
- **Santini F**, Scheffler K, *Assessment of Respiration- and Cardiac-Related Flow Patterns of Cerebro-Spinal Fluid Using Balanced Steady-State Free Precession*

*and Breathing-ECG Synchronization*, Proceedings of the Joint Annual Meeting ISMRM-ESMRMB 2007.

- **Santini F**, Wetzel SG, Scheffler K, *TrueFISP for 7D flow quantification: a solution to saturation-induced signal loss*, Proceedings of the 19th Annual International Conference on Magnetic Resonance Angiography, Istanbul, Turkey, 3-5 October 2007.

- Meckel S, **Santini F**, Stalder A, Markl M, Scheffler K, Wetzel SG, *In vivo visualization of flow in intracranial aneurysms*, Proceedings of the 19th Annual International Conference on Magnetic Resonance Angiography, Istanbul, Turkey, 3-5 October 2007.

- **Santini F**, Bieri O, Scheffler K, *Flow compensation in non-balanced SSFP*, Proceedings of the Annual Meeting ISMRM 2008.

- **Santini F**, Wetzel SG, Scheffler K, *Three-dimensional time-resolved flow quantification with balanced SSFP*, Proceedings of the Annual Meeting ISMRM 2008.

- Meckel S, Stalder A, **Santini F**, Markl M, Scheffler K, Wetzel SG, *In-vivo visualization and analysis of 3D hemodynamics in cerebral aneurysms*, Proceedings of the Annual Meeting ISMRM 2008.

- **Santini F**, Schubert T, Scheffler K, Wetzel SG, *In vivo assessment of CSF flow patterns through 4D flow-sensitive bSSFP sequence*, Proceedings of the 25th annual meeting of ESMRMB, Valencia, Spain, 2008.

- **Santini F**, Schubert T, Scheffler K, Wetzel SG, *In vivo 4D visualization of CSF flow: healthy volunteers and hydrocephalus*, Proceedings of the Annual Meeting ISMRM 2009.

- **Santini F**, Markl M, Scheffler K, *On optimal encoding of flow in three-directional phase-contrast sequences*, Proceedings of the Annual Meeting ISMRM 2009.

# Contents

# Chapter 1

# Introduction

Magnetic resonance imaging is a relatively new diagnostic imaging method, being hypothesized by Raymond Damadian in 1971 [1] as a possible method for tumor detection, and introduced in clinical routine only in the 1980s when the first commercial MRI scanners became available. However, the success of this technique has increased steadily during the years, and nowadays there is an active scientific community developing new methods and concepts. The biggest international conference in the fields of MRI, promoted by the International Society of Magnetic Resonance in Medicine (ISMRM), counts thousands of original contributions each year.

The reasons for the success of MRI for diagnostic imaging are multiple: first of all, the image formation does not rely on the usage of ionizing radiations, and up to date there is no scientific proof of harmful biological effects due to the use of clinical scanners. Secondly, MRI offers a vast range of possibilities for the imaging of soft tissues, enabling the differentiation of structures and the identification of a wide range of lesions. Lastly, the field of application of MRI spans beyond the standard morphological imaging offered by other radiation-based methods, and can provide useful functional information about the organs.

In neuroradiology, MRI is often the tool of choice for the diagnosis, as it can be used to easily differentiate gray and white matter, and techniques for multimodal imaging of the brain are available.

## 1.1 MRI for functional imaging

While other techniques like computed tomography (CT) of X-ray fluoroscopy offer high spatial resolution imaging of the central nervous system, the choice of methods providing functional information is rather limited, and often requires the usage of specialized equipment. For example, digital subtraction angiography is the method of choice for the diagnosis of neurovascular pathologies, but it requires a dedicated machine, ionizing radiation, and the insertion of an intraarterial catheter; positron emission tomography (PET) is a nuclear medicine technique able to visualize tissue perfusion, but with a lack of morphological reference information and the need for a radioactive tracer.

MRI offers a wide range of possibilities to obtain functional information, available on most commercial scanners, often only requiring the selection of an appropriate acquisition method (pulse sequence), or at most the intravenous injection of a gadolinium- or iron-based contrast agent.

Although the term "functional MRI" (fMRI) commonly refers to MR imaging of neural activation, possibly measured through the hemodynamic response indicated by the BOLD effect (change in magnetic properties of oxygenated/deoxygenated hemoglobin), "functional imaging" is a more generic term, relating to all methods that give information about an organ that go beyond the morphological characteristics and explore the actual physiology.

Examples of functional imaging available through MRI are perfusion measurements, time-resolved or cardiac-gated acquisitions of moving organs, chemical shift imaging, diffusion imaging, angiography and flow measurements.

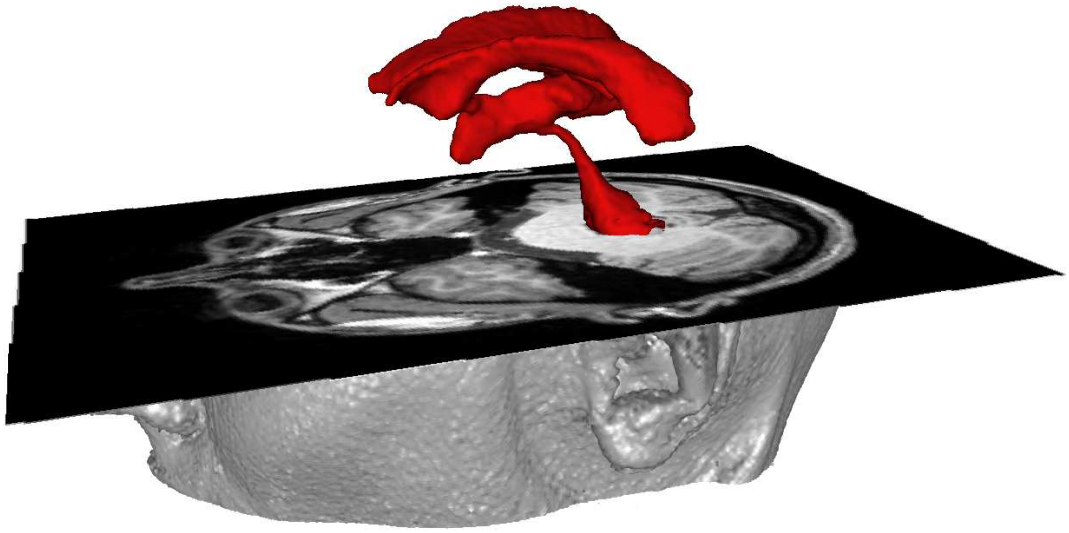

Figure 1.1: Ventricular system of a normal subject.

## 1.2 Flow in the central nervous system

The central nervous system contains two important compartments that are composed of fluids: the neurovascular system, in which blood circulates, and the cerebrospinal fluid (CSF) compartment, which provides mechanical support and protection.

These two compartments are linked together, as CSF is produced by blood filtration inside the choroid plexus in the ventricular system (see fig. 1.1), and subsequently reabsorbed in the venous system. CSF movement is also mainly driven by blood pulsation, that expands the brain vessels and therefore reduces the ventricular space during systole, pushing the CSF outside the ventricular space.

An important pathology, the normal pressure hydrocephalus (NPH) is believed to be a consequence of the driving effect of blood over CSF pulsation. [2, 3]. In normal subjects, the compliance of the brain parenchyma acts as a damper for the blood pulsation, therefore reducing the CSF pulsatility. If the brain tissue becomes stiffer, CSF pulsatility is forced to increase, which leads to enlargement of the ventricular space.

Despite the need for good imaging of CSF flow, in order to correctly define this kind of pathologies, the relaxation characteristics of CSF, which shows very long longitudinal and transversal relaxation times, make it very difficult to measure with conventional fast $T_1$-weighted sequences. For this reason, either long repetition times are required (in the order of seconds), or non-spoiled steady-state sequences (like the balanced steady-state

free precession [bSSFP] sequence) need to be used.

In order to study the flow dynamics of the CNS, it is therefore important to study both the vascular compartment, through angiography and blood flow quantification, and the CSF compartment, whose geometry is simpler, but which requires dedicated technique to be successfully evaluated.

## 1.3 Angiography

Angiography is traditionally defined as "*the radiographic visualization of the blood vessels after injection of a radiopaque substance*" [4]. By extension, Magnetic Resonance Angiography (MRA) refers to "*magnetic resonance imaging used to visualize noninvasively the heart, blood vessels, or blood flow in the circulatory system*" [5], which may or may not involve the use of an exogenous contrast agent.

Even though, strictly speaking, angiography belongs to morphological imaging, the depiction of the vessels generally relies on the effects generated by the blood flowing inside them rather than the actual vascular morphology.

This is often desirable, as the main clinical interest is to study the blood flow itself, in order to evaluate whether the blood supply to areas of the body is adequate, insufficient, lacking, or present but abnormal.

Examples of causes of insufficient or absent blood supply to tissues are thrombosis and stenoses, whereas arteriovenous fistulas are possible examples of abnormal blood supply to body regions. In this latter case, arterial (oxygenated) and venous (deoxygenated) blood get mixed because of a pathological shunt between an artery and a vein. This results in a reduced oxygen supply to the region downstream of the interested artery, and risk of rupture because of an increased blood pressure in the venous system [6–8].

MRI offers various alternatives for obtaining angiographic datasets: some exploit the blood flow velocity to discriminate between fluid and static tissues; others rely on the injection of an intravascular contrast agent that significantly changes the relaxation characteristics of blood, so that it can be easily identified using sequences with conventional weighting.

### 1.3.1 Nonenhanced MRA techniques

Angiography sequences that do not need any contrast agent injection rely on effects that generally go beyond the classical relaxation characteristics of tissues. As a general principle, blood and fluids move inside the body, therefore they experience radiofrequency pulses and magnetic field gradients in a different manner with respect to static tissues.

This can be exploited to enhance the contrast between blood and surrounding tissues.

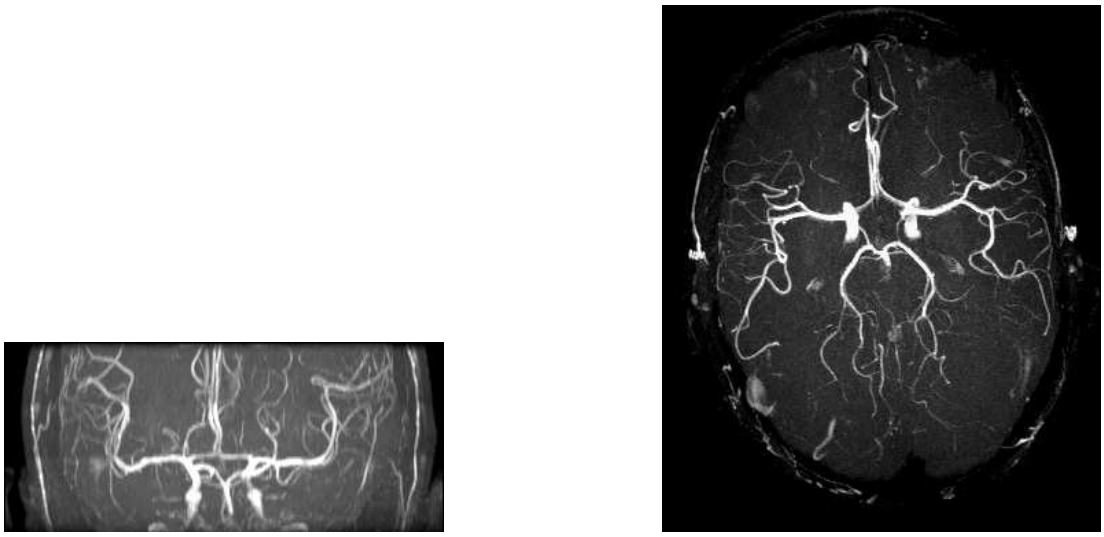

Figure 1.2: Time-of-flight angiography of the brain vessels. Left: coronal maximum intensity projection (MIP); right: transversal MIP.

#### 1.3.1.1 Time-of-flight angiography

The first sequence for angiographic imaging to be introduced was the "time-of-flight" (TOF) technique [9,10]. It is a $T_1$-weighted sequence with a two-dimensional acquisition, or thin-slab three-dimensional acquisition, with slice orientation perpendicular to the main flow direction. Short repetition times produce very low signal from all tissues because of saturation effects. Blood, on the other hand, benefits from the so-called *inflow effect*, which means that at every TR the excited volume of blood leaves the imaging slice, and a new volume enters. The next radiofrequency pulse will therefore excite non-saturated blood, thus resulting in maximum available signal (see fig. 1.2). Sometimes off-resonance saturation pulses are played before the actual excitation to exploit magnetization transfer effects that contribute to the saturation of static tissues [11–13].

This sequence is conceptually simple and easily implemented, and also gives good results in regions were blood flow is mainly directed along a single axis. On the other hand, in regions were vessels bend significantly (see fig. 1.3), a portion of the vessel might fall inside one single slice, causing the inflow effect to cease. In this case, a signal drop is observed and it might be mistaken for a vessel pathology like a stenosis.

#### 1.3.1.2 Phase-contrast angiography

Phase-contrast is a method for velocity quantification, and will be presented in detail in section 1.4. However, it can also be used as a method for the depiction of vessel structure. To achieve this, time-averaged velocity is measured along one or more directions, and then to every voxel in the dataset a gray level value proportional to the measured

Figure 1.3: In-plane saturation in anterior tibial artery mimicking stenosis in TOF acquisition (left), not seen on Gd-enhanced MR angiogram (right). (Source: [14])

velocity is assigned. In case of multiple direction encoding, a sum of squares of the velocities in the measured directions is considered [15, 16]. This angiography method is more accurate than TOF when more than one encoding direction is implemented, but this results in longer scan times, the duration of the acquisition being (roughly) proportional to the number of directions encoded.

#### 1.3.1.3 ECG-gated fast spin-echo

Introduced as a concept in 1985 [17], angiography based on ECG-gated spin echo is now becoming clinically feasible in acceptable scan times thanks to the development of single-shot partial-Fourier fast spin-echo acquisitions [18, 19]. The principle of this technique relies on acquiring two datasets at different instants of the cardiac cycle. In the dataset acquired during systole, the fast flow in the arteries generates flow voids in the vessels, which appear black. In the diastolic phase, the flow is slower and therefore the signal from the artery appears bright. The background and venous signals appear unchanged in the two datasets due to the low velocities of venous flow. Subtracting the systolic dataset from the diastolic one results into a pure arteriogram (see fig. 1.4).

This technique has been successfully applied to thoracic vessels [20] and promising preliminary results have been obtained with peripheral angiography [14, 21].

#### 1.3.1.4 Balanced-SSFP-based methods

balanced steady-state free precession (bSSFP) is a fast sequence characterized by a $T_2/T_1$ contrast. This weighting gives very high signal from fluids, thus making bSSFP an ideal choice for the depiction of vessels, as shown also in chapter 4. This sequence, maybe in conjunction with $T_2$ preparation can be directly used for the depiction of vessels, for example in the imaging of coronary arteries [22, 23]. In alternative, an inversion pulse can be used for background suppression and vessel selection. This technique is termed *arterial spin labeling*, and consists of applying a non-selective inversion pulse

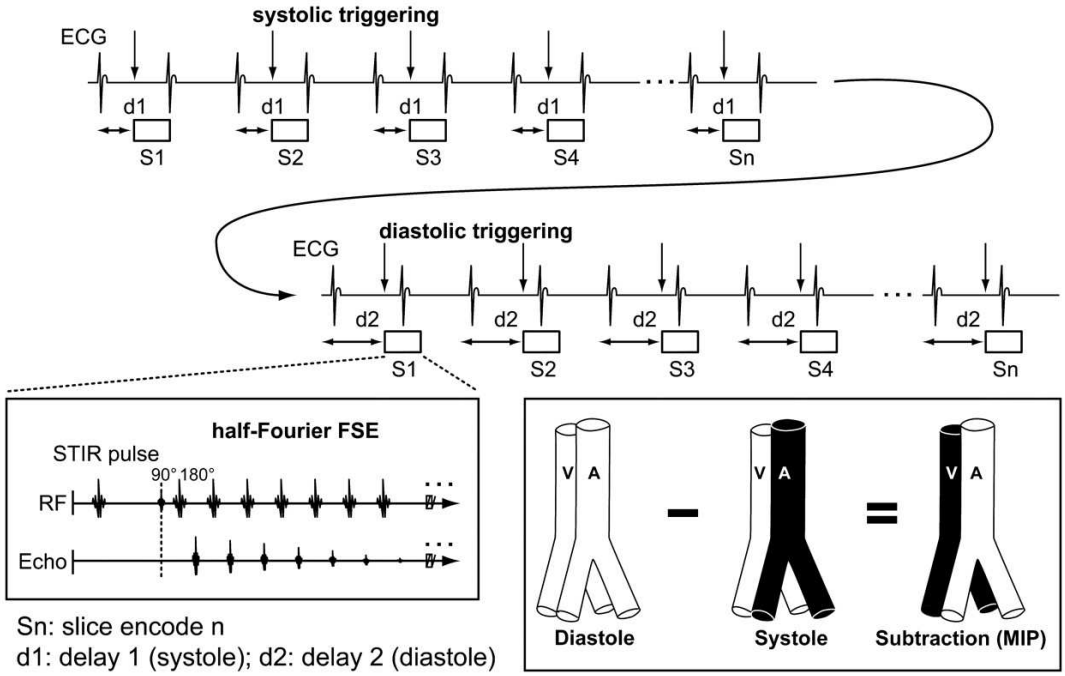


Figure 1.4: Three-dimensional partial-Fourier FSE imaging with systolic and diastolic acquisition. Each section (S1, S2, ... Sn) is imaged in one single-shot acquisition. One trigger delay (d1) is timed for systole for one 3D acquisition, while a second delay (d2) is timed for diastole. Acquisitions are performed every other or every third heartbeat. A short tau inversion-recovery (STIR) pulse can be used for improved fat suppression. To generate a bright-blood angiogram, systolic images (where arterial flow appears dark) are subtracted from diastolic images. A = arteries, RF = radiofrequency, V = veins. (Source: [14])

immediately followed by a slice-selective inversion. The second pulse is targeted to a specific artery. After an inversion time TI that would null the background signal, a fast bSSFP acquisition is performed downstream to the tagging point [24,25]. The result of this acquisition will be a high-contrast arteriogram.

### 1.3.2 Contrast-enhanced MRA techniques

The usage of intravascular contrast agents is highly beneficial from a technique point of view. The contrast media that are normally used for angiography are gadolinium-based, and they reduce the longitudinal relaxation time $T_1$. This allows the acquisition to be performed without exploiting velocity-induced effects, but with standard $T_1$-weighted sequences, which are well-suited for fast imaging [26]. With this method, the depiction of the vessels is not related to flow direction. Contrast-enhanced angiography (CE-MRA) has been widely used, when no contraindication to the use of contrast agent persists [14,27,28].

#### 1.3.2.1 Standard contrast-enhanced MR angiography

Standard contrast-enhanced angiography is performed by intravenous injection of a bolus of contrast agent, followed by a radiofrequency-spoiled gradient recalled echo (RF-spoiled GRE) acquisition [26,29]. With conventional "extracellular" contrast agents (molecules that diffuse from the blood vessels to the extracellular space), the acquisition is normally limited as "first pass" of the contrast agent bolus, as imaging in the "steady-state" angiography is not useful because of rapid extravasation of such extracellular contrast media resulting in decreasing vascular and increasing background signal [26,27]. More recently [27], a new class of contrast agents, named *blood pool* contrast agents, has been introduced. Molecules of this family are bound to macromolecules that do not diffuse in the extravascular space (albumin, dextran, polylisine, etc. [30,31]). These contrast agents allow acquisition of an arteriovenous angiogram during up to 42 minutes after injection [27].

With a standard first-pass angiography acquisition, one three-dimensional dataset is acquired. The sequence timing is adjusted in order to have the center of the k-space acquired either during the arterial phase (all arteries are enhanced but no venous enhancement is visible yet), or during a later phase when all the vessels are enhanced.

The critical point in this kind of acquisition is to time the sequence correctly in order to have all the desired vessels properly enhanced. Early acquisition of the k-space center can result in "ringing" artifacts at the vessel boundaries (see fig. 1.5), whereas late acquisition results in decreased arterial signal and venous contamination [29]. The most used timing technique is the injection of a low-dose test bolus, imaged with a time-resolved sequence, in order to calculate the time needed for the bolus to reach the region of interest. This time is then introduced as a delay for the second acquisition. with the actual contrast agent bolus.

In order to avoid dealing with bolus timing, or to image areas where arterial enhancement can occur at different time points, a complete time-resolved approach can

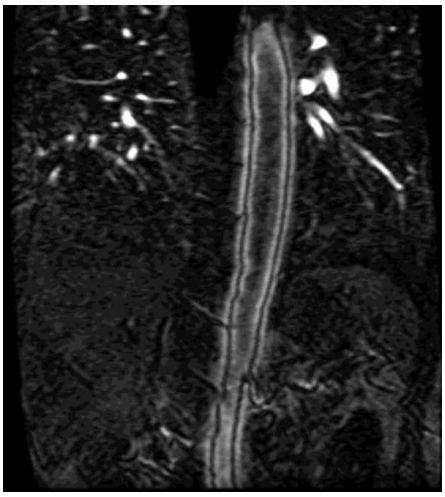

Figure 1.5: Ringing artifact due to early acquisition of k-space center in CE-MRA (Source: [29])

be used.

#### 1.3.2.2 Time-resolved angiography

Time-resolved acquisition protocols have been available since 1996 [32], and are getting more and more used as newer acquisition acceleration techniques implemented on commercial MRI scanners. Most of these techniques rely on view sharing (Time-Resolved imaging of Contrast KineticS [TRICKS] [32], Time-Resolved Echo-shared Angiographic Technique [TREATS] [33, 34], Time-resolved imaging With Stochastic Trajectories [TWIST] [21], 4-Dimensional Time-Resolved Angiography using Keyhole [4D-TRAK] [35]).

The acquisition is still a three-dimensional $T_1$-weighted sequence, but several datasets are acquired subsequently, each with an acquisition time ranging from one to few seconds.

The acquired datasets are normally reconstructed separately, providing hemodynamic flow information. With time-resolved MRA it is possible to depict phenomena with short arterial-to-venous transit times, distinguish arterial from venous structures and determine direction of flow.

With this acquisition method, multiple datasets of arterial and arteriovenous phases are obtained. In order to obtain a pure arteriogram or venogram, a postprocessing algorithm for artery/vein separation is needed. The existing algorithms are semiautomatic, needing a certain degree of user interaction for selection of reference points or images [36–38]. A novel method for completely automatic artery/vein separation is presented in chapter 2.

## 1.4 Flow quantification

MRI allows for another method of assessment and visualization of the characteristics of flow inside vessels and organs. By using the characteristics of the MR signal, it is possible to encode the actual velocity of a moving set of protons (isochromat) in the "phase" component of the reconstructed image. This is useful, for example, in cardiology to calculate the ventricular stroke volume, valve regurgitation, etc. [39, 40] or in neuroradiology to assess the flow characteristics of the cerebrospinal fluid in pathologies like hydrocephalus and Chiari malformation [41, 42].

Recently, the study of three-dimensional flow patterns allowed for the study of other flow-related parameters like wall shear stress and vorticity, that are believed to correlate with the severity or the prognosis of vascular pathologies like plaque formation or aneurysm development [43, 44].

### 1.4.1 Phase and motion

Moving isochromats interact with the imaging gradients in a different way with respect to stationary spins. The standard imaging concepts assume that every isochromat experiences a magnetic field generated by gradients whose intensity is only determined by the spin's spatial position. This results in a phase evolution of the signal given by the isochromat that is directly proportional to the spatial position and to the zeroth moment of the applied gradient.

In general, the phase evolution is given by:

$$\phi(t) = \int_0^t \omega_L(\tau)d\tau = \gamma \int_0^t B(\tau)d\tau = \gamma \int_0^t G_x(\tau)x(\tau)d\tau, \tag{1.1}$$

where $\omega_L$is the local Larmor pulsation, $\gamma$ is the gyromagnetic ratio, $B(t)$ is the local magnetic field, $G_x(t)$ is the gradient amplitude, $x(t)$ is the spatial position of the isochromat along the gradient axis. Assuming a constant position over time $x(t) = x_0$:

$$\phi(t) = \gamma \left( \int_0^t G_x(\tau)d\tau \right) x_0 = \gamma M_0 x_0, \tag{1.2}$$

where $M_0 = \int_0^t G_x(\tau)d\tau$ is named "zeroth moment" of the gradient.

If the spatial position is not constant, but the isochromat is moving a constant velocity, i.e. $x(t) = x_0 + v_x t$, eq. (1.1) becomes:

$$\begin{aligned} \phi(t) &= \gamma \int_0^t G_x(\tau) \left(x_0 + v_x \tau\right) d\tau \\ &= \gamma \left( \int_0^t G_x(\tau)d\tau \right) x_0 + \gamma \left( \int_0^t G_x(\tau)\tau d\tau \right) v_x \\ &= \gamma M_0 x_0 + \gamma M_1 v_x, \end{aligned} \tag{1.3}$$

where $M_1 = \int_0^t G_x(\tau)\tau d\tau$ is named "first moment" of the gradient.

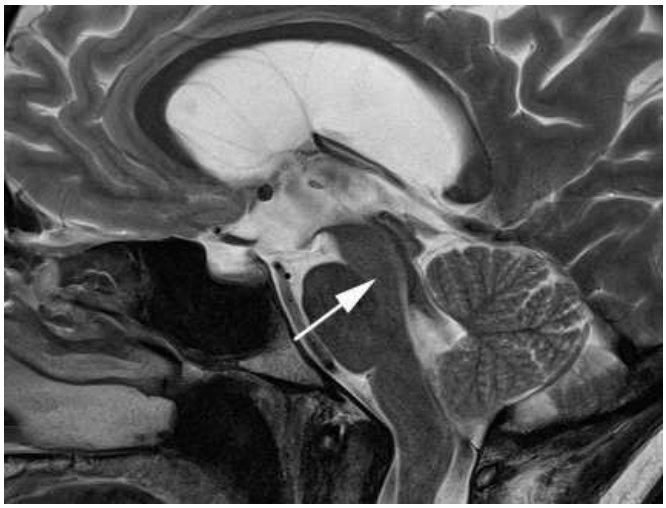

Figure 1.6: Flow void (arrow) due to intra-voxel dephasing related to flow in the Aqueduct of Sylvius.

As shown in the formula, a moving isochromat acquires a phase that is normally unwanted, and this can be a cause of artifacts, like signal loss due to intra-voxel dephasing (given by different phases accumulated by spins inside one voxel moving at different speeds, see fig. 1.6), or shifting of anatomical structures [45].

#### 1.4.1.1 Phase contrast

In the approximation of constant flow velocity, the phase of the isochromat assumes a value that is proportional to the first moment of the gradient along the flow direction and to the velocity itself. If the imaging sequence is designed in a way that the first moment of the gradients is kept constant throughout the whole k-space, then this phase shift does not cause any artifact but will be encoded in the reconstructed phase image, and can be used to obtain direct information about flow velocity.

However, phase images may have spurious errors due to field inhomogeneities or radiofrequency penetration effects [45], that would interfere with the possibility of quantifying velocity from a single scan. These background phases are independent of the gradient pulses and can be eliminated if two phase images are collected and subtracted. If the first moment of the gradients is changed between two such scans, there will be velocity dependent phase information in the subtracted image. This method is named *phase contrast* and was introduced in 1960 by Hahn [46].

The practical realization of a phase contrast sequence, in the most classical form, consists of a standard imaging sequence, normally based on gradient-echo in order to achieve short acquisition times [47], in which a bipolar gradient pulse is added (on any axis) before signal acquisition (see fig. 1.7). This bipolar pulse has $M_0 = 0$, therefore it does not contribute to the spatial encoding, and has a $M_1$ that depends on the

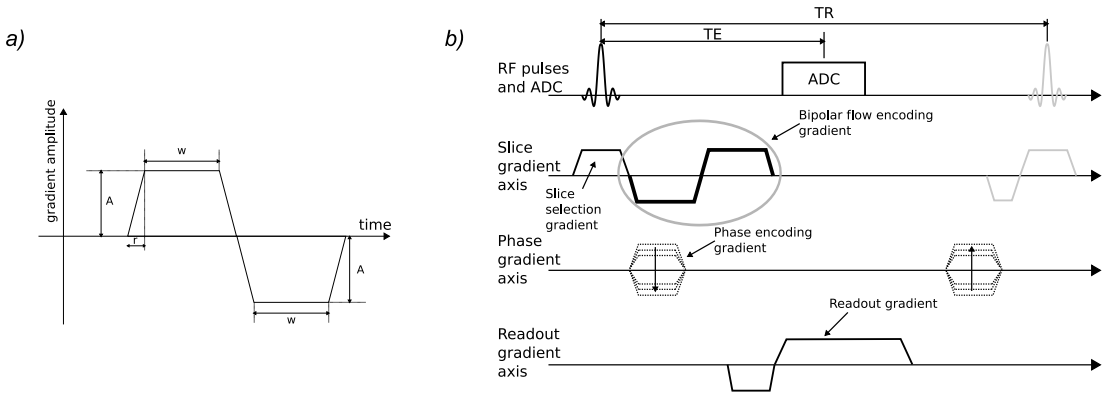


Figure 1.7: *a)* Bipolar gradient pulse; *b)* Typical pulse sequence with flow encoding in the through-plane direction.

parameters of the gradient pulse (see fig. 1.7a for symbol reference):

$$M_1 = A(w + r)(w + 2r). \tag{1.4}$$

The second acquisition is either performed without the flow-sensitizing gradient (reference acquisition), or with inverted polarity, and therefore opposite $M_1$ (balanced acquisition).

The $M_1$ value also poses a limit on the maximum velocity that can be encoded by the sequence, as the phase can only assume values between $-\pi$ and $+\pi$. This velocity limit is called Venc (sometimes referred to velocity anti-aliasing limit), and is the velocity value that gives a phase shift of $\pi$, and can be obtained with the following formula:

$$v_{enc} = \pi/\gamma \Delta M_1, \tag{1.5}$$

where $\gamma$ is the gyromagnetic ratio and $\Delta M_1$ is the difference of the first moments of the flow-sensitizing gradients of the two scans. It is important to correctly choose a Venc not lower than the maximum expected velocity, otherwise phase wrapping occurs, and not too much higher, otherwise the signal-to-noise ratio decays.

The velocity can be extracted from the phase contrast image by simple scaling of the phase value of the image resulting from the subtraction of the phase images:

$$v = \phi/\gamma \Delta M_1, \tag{1.6}$$

where $\phi$ is the measured phase. An example of phase contrast data from the head vessels is shown in figure 1.8.

### 1.4.2 Three-directional, three-dimensional, time-resolved

Since the beginning of the 1990s, the phase contrast method was extended in order to encode flow in multiple directions in a single acquisition session [47–49]. All the

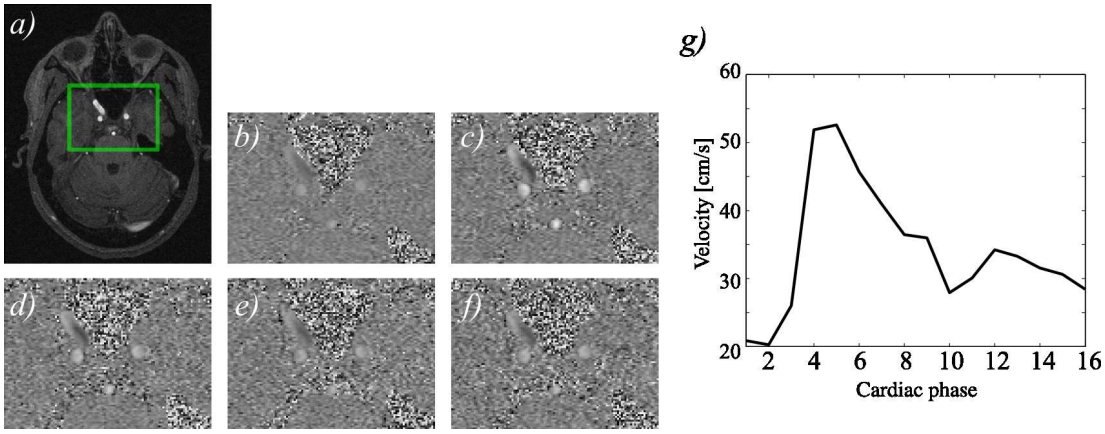


Figure 1.8: Two-dimensional phase contrast data of the internal carotid arteries and of the basilar artery. *a)* Magnitude image. *b-f)* Phase contrast images of the highlighted region, at five different cardiac phases. The arteries look brighter in the systolic phase due to higher velocities. *g)* Velocity time course in the right internal carotid artery extracted from the phase contrast images.

| | x | y | z |
|---|---|---|---|
| 1 | 0 | 0 | 0 |
| 2 | + | 0 | 0 |
| 3 | 0 | + | 0 |
| 4 | 0 | 0 | + |

| | x | y | z |
|---|---|---|---|
| 1 | - | - | - |
| 2 | + | + | - |
| 3 | + | - | + |
| 4 | - | + | + |

Table 1.1: Tables representing the signs of the encoding moments in three-directional flow assessment. Rows are encoding steps, columns are encoding direction. A "+" sign represents positive encoding moment; a "-" sign represents negative encoding moment; a "0" sign means no encoding. On the left, four-point referenced acquisition scheme; on the right, four-point balanced acquisition scheme.

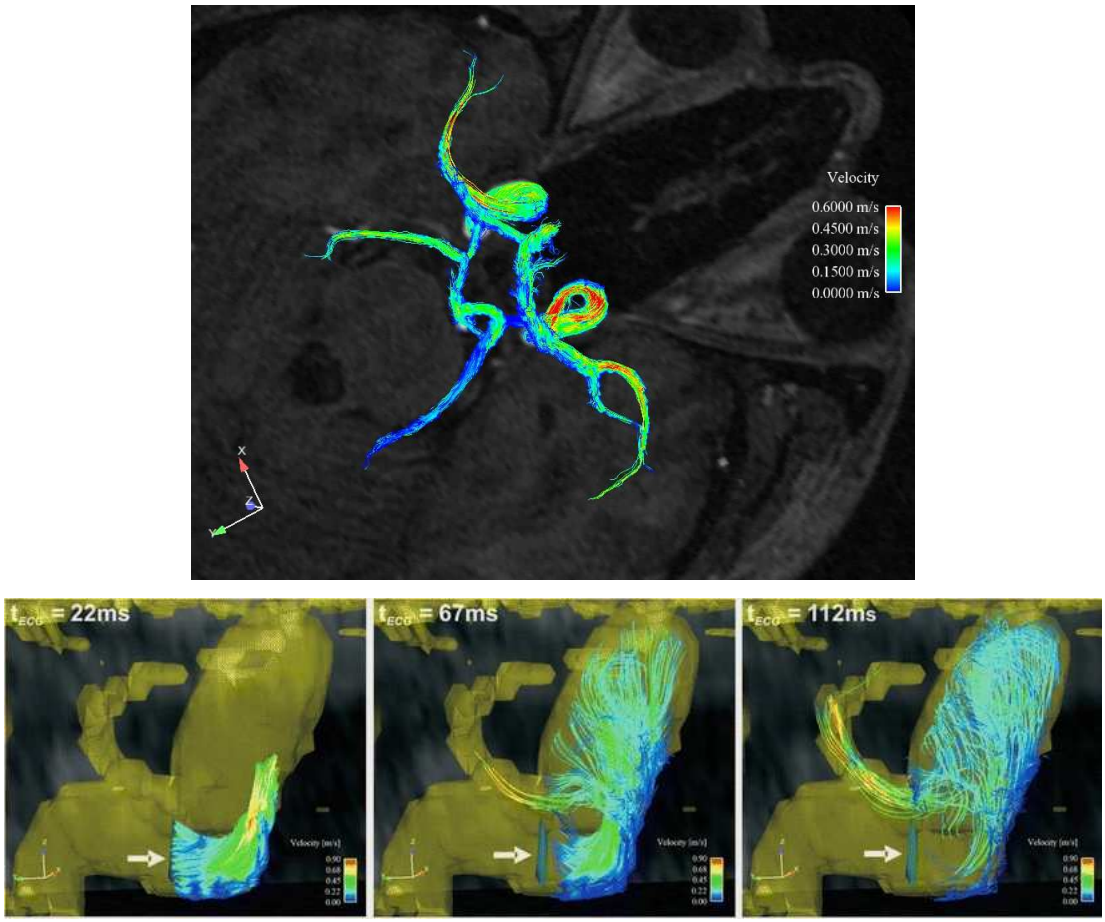


Figure 1.9: Three-dimensional, three-directional, time-resolved flow measurement of the cerebral vessels. *top:* streamlines in the circle of Willis of a healthy volunteer. *bottom:* streamlines in a large, wide-necked, oval-shaped parophthalmic aneurysm of the right internal cerebral artery (adapted from [43]).

presented methods rely on acquiring four steps, with different flow sensitivities (see table 1.1).

In 2003, Markl *et al* [50] demonstrated the feasibility of a time-resolved three-dimensional technique for flow acquisition, based on RF-spoiled gradient echo, together with a visualization procedure able to depict flow patterns in three dimensions. This approach allows a more flexible definition of areas of interest inside the acquired dataset, and the possibility of extracting indirect flow-related parameters like wall shear stress.

Two examples of three-directional, three-dimensional, time-resolved flow quantification of the brain vessels is shown in figure 1.9.

## 1.5 Aim of the thesis

As mentioned above, MRI is a major tool for the diagnosis of brain diseases, and in fact a very significant portion of research efforts from the international community is focused on head imaging. BOLD fMRI, perfusion MRI were primarily developed for monitoring the activity and viability of the central nervous system. However, most of the methods still hold room for improvement. One major issue is the increase of signal-to-noise, for multiple reasons: apart from the obvious increase in image quality, signal gain can also be traded for higher resolutions and for faster acquisitions. Therefore the general goal of method development is to obtain better, more detailed images, and faster. However, signal-to-noise does not necessarily mean higher diagnostic potential. The other crucial aspect derives from image contrast. An optimal sequence will have a high contrast between the desired target of the imaging (a lesion, a vessel, etc.) and the background.

In this thesis, new methods are presented that aim to enhance image quality in the visualization of intracranial flow. The aim of the methods hereby presented is to achieve a higher diagnostic potential by enhancing signal characteristics and image contrast with respect to unwanted background.

For angiographic acquisition, this is achieved by introducing a postprocessing method for time-resolved contrast-enhanced MR angiography datasets which enables, in an operator-independent way, the suppression of unwanted background structures and the enhancement of potential pathological conditions.

For flow quantification, a new technique for three-dimensional flow, based on balanced-SSFP, is presented. bSSFP is a fast acquisition sequence that gives optimal signal for the imaging of fluids (and for this reason it can also directly used for angiography, as mentioned in section 1.3.1.4). From a SNR point of view, it has ideal characteristics to be used as a flow quantification sequence. This sequence can be used to explore the blood flow in intracranial vessels, and the flow of CSF in the ventricular and subarachnoid space.

The goal of the thesis is to present these novel methods, and evaluate their applicability in a real clinical environment. For this reasons, experiments on healthy subjects and on patients are considered in this work.

## 1.6 Outline of the thesis

This thesis is divided in two parts, each focusing mainly on one of the two fluid compartments of the CNS: the blood and the CSF. The first part, titled Angiography, presents a novel method for the study of time-resolved contrast-enhanced MRA datasets. From a time series of three-dimensional angiography datasets, acquired during the first pass of the contrast agent bolus, a single color-coded dataset is obtained, in which arteries and veins are separated and pathologies that impair the blood flow, like arteriovenous malformations, are highlighted. In particular, in **chapter 2** the algorithm double-reference cross-correlation that performs the separation and the color-coding is presented, while **chapter 3** demonstrates a method for automatic reference selection to be used with

the previous algorithm in order to achieve unsupervised analysis of the time-resolved datasets. The method is based on the analysis of the time courses of the signal intensity of each voxel in the dataset. These time courses reflect the bolus shape and timing at each anatomical location. The comparison with two reference functions, representing the time course of the signal intensity in arteries and veins respectively, gives a probability index that the considered test voxel belongs to an artery, to a vein, or to the background. The algorithm presented in this thesis uses cross-correlation as similarity test, hence the name of the method, but also introduces a way of taking into account the mutual correlation between references to achieve a more accurate separation. This is realized by applying a red-green-blue colormap to the output dataset, which changes its characteristics depending on the reference correlation value.

The identification of the reference time courses can be done manually, or with an automatic algorithm. The proposed automatic algorithm for reference selection is based on a modified *k-means* clustering technique that performs an approximate unsupervised separation on a subset of the acquired voxels. Chapter 3 introduces this algorithm and demonstrates that there is no statistical difference in the quality of the final angiograms

In the second part, termed FLOW QUANTIFICATION, a novel method for time-resolved three-dimensional, three-directional flow quantification is presented. This method is based on bSSFP, and is especially suited for the investigation of CSF flow patterns. In **chapter 4** the sequence is introduced; in **chapter 5** a reconstruction method able to enhance the temporal resolution of flow quantification sequences is presented. Balanced SSFP, with a $T_2/T_1$ contrast and short repetition times (in the order of few milliseconds), is an ideal sequence for fast acquisition of fluids, which present long longitudinal and transversal relaxation constants, because at the end of TR the transversal magnetization is refocused and preserved in a steady-state. Flow quantification based on this sequence can have high SNR, thus allowing the usage of acceleration techniques for reducing the total acquisition times. However, the steady-state of bSSFP is very sensitive to dephasing due to flow or eddy currents, therefore special measures need to be taken in the sequence design in order to minimize the artifacts arising from these two phenomena. In chapter 4 the two main methods for eddy current compensation are presented and compared, and the optimal implementation is identified. Unfortunately, these methods introduce a penalty in the temporal resolution. The reconstruction technique presented in chapter 5 is an efficient reconstruction method to compensate for this penalty.

Finally **chapter 6** shows preliminary results of the clinical application of the aforementioned flow encoding sequence. This sequence is used to image the ventricular system of healthy volunteers, in order to identify physiologic flow patterns of the CSF, and to image the CSF circulation in a patient suffering of three-ventricular hydrocephalus, before a ventriculostomy operation was performed, and after surgery, in order to confirm the diagnosis and to assess the outcome of the operation.

## References

[1] R. Damadian, "Tumor detection by nuclear magnetic resonance," *Science (New York, N.Y.)*, vol. 171, pp. 1151–1153, Mar. 1971. PMID: 5544870.

[2] A. Lavinio, Z. Czosnyka, and M. Czosnyka, "Cerebrospinal fluid dynamics: disturbances and diagnostics," *European Journal of Anaesthesiology. Supplement*, vol. 42, pp. 137–141, 2008. PMID: 18289431.

[3] H. Williams, "The venous hypothesis of hydrocephalus," *Med Hypotheses*, vol. 70, pp. 743–7, 2008. Williams, Helen Scotland Medical hypotheses Med Hypotheses. 2008;70(4):743-7. Epub 2007 Oct 4.

[4] "angiography - definition from merriam-webster's medical dictionary (http://www.merriam-webster.com/)."

[5] "magnetic resonance angiography - definition from merriam-webster's medical dictionary (http://www.merriam-webster.com/)."

[6] P. Moftakhar, J. S. Hauptman, D. Malkasian, and N. A. Martin, "Cerebral arteriovenous malformations. part 2: physiology," *Neurosurgical Focus*, vol. 26, p. E11, May 2009. PMID: 19408989.

[7] Y. Miyasaka, A. Kurata, K. Tokiwa, R. Tanaka, K. Yada, and T. Ohwada, "Draining vein pressure increases and hemorrhage in patients with arteriovenous malformation," *Stroke*, vol. 25, pp. 504–507, Feb. 1994.

[8] M. Marks, B. Lane, G. Steinberg, and P. Chang, "Hemorrhage in intracerebral arteriovenous malformations: angiographic determinants," *Radiology*, vol. 176, pp. 807–813, Sept. 1990.

[9] G. A. Laub and W. A. Kaiser, "Mr angiography with gradient motion refocusing," *Journal of Computer Assisted Tomography*, vol. 12, pp. 377–382, June 1988. PMID: 3366945.

[10] D. G. Nishimura, "Time-of-flight mr angiography," *Magnetic Resonance in Medicine: Official Journal of the Society of Magnetic Resonance in Medicine / Society of Magnetic Resonance in Medicine*, vol. 14, pp. 194–201, May 1990. PMID: 2345502.

[11] G. B. Pike, B. S. Hu, G. H. Glover, and D. R. Enzmann, "Magnetization transfer time-of-flight magnetic resonance angiography," *Magnetic Resonance in Medicine: Official Journal of the Society of Magnetic Resonance in Medicine / Society of Magnetic Resonance in Medicine*, vol. 25, pp. 372–379, June 1992. PMID: 1614322.

[12] M. Miyazaki, F. Kojima, N. Ichinose, Y. Onozato, and H. Igarashi, "A novel saturation transfer contrast method for 3d time-of-flight magnetic resonance angiography: a slice-selective off-resonance sinc pulse (sors) technique," *Magnetic Resonance in Medicine: Official Journal of the Society of Magnetic Resonance in Medicine / Society of Magnetic Resonance in Medicine*, vol. 32, pp. 52–59, July 1994. PMID: 8084237.

[13] D. Atkinson, M. Brant-Zawadzki, G. Gillan, D. Purdy, and G. Laub, "Improved mr angiography: magnetization transfer suppression with variable flip angle excitation and increased resolution," *Radiology*, vol. 190, pp. 890–894, Mar. 1994. PMID: 8115646.

[14] M. Miyazaki and V. S. Lee, "Nonenhanced mr angiography," *Radiology*, vol. 248, pp. 20–43, July 2008. PMID: 18566168.

[15] C. L. Dumoulin, "Phase contrast mr angiography techniques," *Magnetic Resonance Imaging Clinics of North America*, vol. 3, pp. 399–411, Aug. 1995. PMID: 7584246.

[16] C. L. Dumoulin, S. P. Souza, M. F. Walker, and W. Wagle, "Three-dimensional phase contrast angiography," *Magnetic Resonance in Medicine: Official Journal of the Society of Magnetic Resonance in Medicine / Society of Magnetic Resonance in Medicine*, vol. 9, pp. 139–149, 1989. PMID: 2709992.

[17] V. J. Wedeen, R. A. Meuli, R. R. Edelman, S. C. Geller, L. R. Frank, T. J. Brady, and B. R. Rosen, "Projective imaging of pulsatile flow with magnetic resonance," *Science (New York, N.Y.)*, vol. 230, pp. 946–948, Nov. 1985. PMID: 4059917.

[18] M. Miyazaki, S. Sugiura, F. Tateishi, H. Wada, Y. Kassai, and H. Abe, "Non-contrast-enhanced mr angiography using 3d ecg-synchronized half-fourier fast spin echo," *Journal of Magnetic Resonance Imaging: JMRI*, vol. 12, pp. 776–783, Nov. 2000. PMID: 11050650.

[19] M. Miyazaki, H. Takai, S. Sugiura, H. Wada, R. Kuwahara, and J. Urata, "Peripheral mr angiography: separation of arteries from veins with flow-spoiled gradient pulses in electrocardiography-triggered three-dimensional half-fourier fast spin-echo imaging," *Radiology*, vol. 227, pp. 890–896, June 2003. PMID: 12702824.

[20] J. Urata, M. Miyazaki, H. Wada, T. Nakaura, Y. Yamashita, and M. Takahashi, "Clinical evaluation of aortic diseases using nonenhanced mra with ecg-triggered 3d half-fourier fse," *Journal of Magnetic Resonance Imaging: JMRI*, vol. 14, pp. 113–119, Aug. 2001. PMID: 11477668.

[21] R. P. Lim, M. Shapiro, E. Y. Wang, M. Law, J. S. Babb, L. E. Rueff, J. S. Jacob, S. Kim, R. H. Carson, T. P. Mulholland, G. Laub, and E. M. Hecht, "3d time-resolved mr angiography (mra) of the carotid arteries with time-resolved imaging with stochastic trajectories: comparison with 3d contrast-enhanced bolus-chase mra and 3d time-of-flight mra," *AJNR. American Journal of Neuroradiology*, vol. 29, pp. 1847–1854, Nov. 2008. PMID: 18768727.

[22] V. S. Deshpande, S. M. Shea, G. Laub, O. P. Simonetti, J. P. Finn, and D. Li, "3d magnetization-prepared true-fisp: a new technique for imaging coronary arteries," *Magnetic Resonance in Medicine: Official Journal of the Society of Magnetic Resonance in Medicine / Society of Magnetic Resonance in Medicine*, vol. 46, pp. 494–502, Sept. 2001. PMID: 11550241.

[23] S. M. Shea, V. S. Deshpande, Y.-C. Chung, and D. Li, "Three-dimensional true-fisp imaging of the coronary arteries: improved contrast with t2-preparation," *Journal of Magnetic Resonance Imaging: JMRI*, vol. 15, pp. 597–602, May 2002. PMID: 11997902.

[24] M. Katoh, A. Buecker, M. Stuber, R. W. G. unther, and E. Spuentrup, "Free-breathing renal mr angiography with steady-state free-precession (ssfp) and slab-selective spin inversion: initial results," *Kidney International*, vol. 66, pp. 1272–1278, Sept. 2004. PMID: 15327427.

[25] K. Scheffler and S. Lehnhardt, "Principles and applications of balanced ssfp techniques," *European Radiology*, vol. 13, pp. 2409–2418, Nov. 2003. PMID: 12928954.

[26] M. R. Prince, "Gadolinium-enhanced mr aortography," *Radiology*, vol. 191, pp. 155–164, Apr. 1994. PMID: 8134563.

[27] J. Bremerich, D. Bilecen, and P. Reimer, "Mr angiography with blood pool contrast agents," *European Radiology*, vol. 17, pp. 3017–3024, Dec. 2007. PMID: 17639407.

[28] E. A. Sadowski, L. K. Bennett, M. R. Chan, A. L. Wentland, A. L. Garrett, R. W. Garrett, and A. Djamali, "Nephrogenic systemic fibrosis: risk factors and incidence estimation," *Radiology*, vol. 243, pp. 148–157, Apr. 2007. PMID: 17267695.

[29] H. Zhang, J. H. Maki, and M. R. Prince, "3d contrast-enhanced mr angiography," *Journal of Magnetic Resonance Imaging: JMRI*, vol. 25, pp. 13–25, 2007. PMID: 17154188.

[30] C. Burtea, S. Laurent, J.-M. Colet, L. V. Elst, and R. N. Muller, "Development of new glucosylated derivatives of gadolinium diethylenetriaminepentaacetic for magnetic resonance angiography," *Investigative Radiology*, vol. 38, pp. 320–333, June 2003. PMID: 12908699.

[31] H. Kobayashi, S. Kawamoto, S.-K. Jo, H. L. Bryant, M. W. Brechbiel, and R. A. Star, "Macromolecular mri contrast agents with small dendrimers: pharmacokinetic differences between sizes and cores," *Bioconjugate Chemistry*, vol. 14, pp. 388–394, Apr. 2003. PMID: 12643749.

[32] F. R. Korosec, R. Frayne, T. M. Grist, and C. A. Mistretta, "Time-resolved contrast-enhanced 3d mr angiography," *Magnetic Resonance in Medicine: Official Journal of the Society of Magnetic Resonance in Medicine / Society of Magnetic Resonance in Medicine*, vol. 36, pp. 345–351, Sept. 1996. PMID: 8875403.

[33] M. A. Griswold, P. M. Jakob, R. M. Heidemann, M. Nittka, V. Jellus, J. Wang, B. Kiefer, and A. Haase, "Generalized autocalibrating partially parallel acquisitions (grappa)," *Magnetic Resonance in Medicine: Official Journal of the Society of Magnetic Resonance in Medicine / Society of Magnetic Resonance in Medicine*, vol. 47, pp. 1202–1210, June 2002. PMID: 12111967.

[34] C. Pinto, R. Hickey, T. J. Carroll, K. Sato, K. Dill, R. A. Omary, R. Kroeker, O. Simonetti, and J. C. Carr, "Time-resolved mr angiography with generalized autocalibrating partially parallel acquisition and time-resolved echo-sharing angiographic technique for hemodialysis arteriovenous fistulas and grafts," *Journal of Vascular and Interventional Radiology: JVIR*, vol. 17, pp. 1003–1009, June 2006. PMID: 16778234.

[35] W. A. Willinek, D. R. Hadizadeh, M. von Falkenhausen, H. Urbach, R. Hoogeveen, H. H. Schild, and J. urgen Gieseke, "4d time-resolved mr angiography with keyhole (4d-trak): more than 60 times accelerated mra using a combination of centra, keyhole, and sense at 3.0t," *Journal of Magnetic Resonance Imaging: JMRI*, vol. 27, pp. 1455–1460, June 2008. PMID: 18504736.

[36] M. Bock, S. O. Schoenberg, F. Floemer, and L. R. Schad, "Separation of arteries and veins in 3d mr angiography using correlation analysis," *Magn Reson Med*, vol. 43, pp. 481–7, 2000. 0740-3194 (Print) Journal Article.

[37] J. Kim and R. Zabih, "Automatic segmentation of contrast-enhanced time resolved image series," *Journal of X-Ray Science and Technology*, vol. 9, pp. 1–11, 2000.

[38] A. L. Martel, D. Fraser, G. S. Delay, P. S. Morgan, and A. R. Moody, "Separating arterial and venous components from 3d dynamic contrast-enhanced mri studies using factor analysis," *Magn Reson Med*, vol. 49, pp. 928–33, 2003. 0740-3194 (Print) Journal Article.

[39] M. B. Srichai, R. P. Lim, S. Wong, and V. S. Lee, "Cardiovascular applications of phase-contrast mri," *AJR. American Journal of Roentgenology*, vol. 192, pp. 662–675, Mar. 2009. PMID: 19234262.

[40] P. D. Gatehouse, J. Keegan, L. A. Crowe, S. Masood, R. H. Mohiaddin, K.-F. Kreitner, and D. N. Firmin, "Applications of phase-contrast flow and velocity imaging in cardiovascular mri," *European Radiology*, vol. 15, pp. 2172–2184, Oct. 2005. PMID: 16003509.

[41] A. A. Linninger, M. Xenos, D. C. Zhu, M. R. Somayaji, S. Kondapalli, and R. D. Penn, "Cerebrospinal fluid flow in the normal and hydrocephalic human brain," *IEEE Trans Biomed Eng*, vol. 54, pp. 291–302, 2007.

[42] O. Algın, B. Hakyemez, G. Gokalp, E. Korfalı, and M. Parlak, "Phase-contrast cine mri versus mr cisternography on the evaluation of the communication between intraventricular arachnoid cysts and neighbouring cerebrospinal fluid spaces," *Neuroradiology*, vol. 51, pp. 305–312, May 2009. PMID: 19172255.

[43] S. Meckel, A. F. Stalder, F. Santini, E.-W. R. u, D. A. R. ufenacht, M. Markl, and S. G. Wetzel, "In vivo visualization and analysis of 3-d hemodynamics in cerebral aneurysms with flow-sensitized 4-d mr imaging at 3 t," *Neuroradiology*, vol. 50, pp. 473–484, June 2008. PMID: 18350286.

[44] M. A. Castro, C. M. Putman, M. J. Sheridan, and J. R. Cebral, "Hemodynamic patterns of anterior communicating artery aneurysms: a possible association with rupture," *AJNR. American Journal of Neuroradiology*, vol. 30, pp. 297–302, Feb. 2009. PMID: 19131411.

[45] E. M. Haacke, R. W. Brown, M. R. Thompson, and R. Venkatesan, *Magnetic Resonance Imaging: Physical Principles and Sequence Design. 1999.* John Wiley & Sons, New York.

[46] E. L. Hahn, "Detection of sea-water motion by nuclear precession," *Journal of Geophysical Research*, vol. 65, p. 776, 1960.

[47] R. Hausmann, J. S. Lewin, and G. Laub, "Phase-contrast mr angiography with reduced acquisition time: new concepts in sequence design," *Journal of Magnetic Resonance Imaging: JMRI*, vol. 1, pp. 415–422, Aug. 1991. PMID: 1790363.

[48] N. J. Pelc, M. A. Bernstein, A. Shimakawa, and G. H. Glover, "Encoding strategies for three-direction phase-contrast mr imaging of flow," *Journal of Magnetic Resonance Imaging*, vol. 1, pp. 405–413, 1991.

[49] C. L. Dumoulin, S. P. Souza, R. D. Darrow, N. J. Pelc, W. J. Adams, and S. A. Ash, "Simultaneous acquisition of phase-contrast angiograms and stationary-tissue images with hadamard encoding of flow-induced phase shifts," *Journal of Magnetic Resonance Imaging*, vol. 1, pp. 399–404, 1991.

[50] M. Markl, F. P. Chan, M. T. Alley, K. L. Wedding, M. T. Draney, C. J. Elkins, D. W. Parker, R. Wicker, C. A. Taylor, R. J. Herfkens, and N. J. Pelc, "Time-resolved three-dimensional phase-contrast mri," *Journal of Magnetic Resonance Imaging: JMRI*, vol. 17, pp. 499–506, Apr. 2003. PMID: 12655592.

# Part I

# Angiography

# Chapter 2

# Artery/vein separation in contrast-enhanced MR angiography

An adapted version of this chapter is published as: Santini F, Patil S, Meckel S, Scheffler K, Wetzel SG. *Double-reference cross-correlation algorithm for separation of the arteries and veins from 3D MRA time series.* Journal of Magnetic Resonance Imaging. 2008 ;28(3):646-654.

## 2.1 Introduction

Time-resolved contrast-enhanced magnetic resonance angiography (CE-MRA) [1–3] with high temporal resolution has become a widely used technique to visualize the dynamic transit of a contrast bolus from the arterial to the arteriovenous phase. To improve the visualization of vascular structure compared to background, usually magnitude or complex subtraction is performed [4]. This method, either implemented as a 2D or 3D sequence, has been extensively used, for example, for the work-up of neurovascular disorders (e.g. arteriovenous fistula) [5–11]. However, there are important limitations of the technique. First, due to the short arteriovenous transit time (e.g. 8 sec for the cerebral vessels) and the small diameter of many important vessels, there is a trade-off between the spatial and temporal resolutions of CE-MRA even if accelerated MR acquisitions with parallel imaging techniques are used. Second, in contrast to intra-arterial digital subtraction angiography (DSA), due to the arterial overlay in the venous phase, a separation of the arterial and venous phase is not possible, but merely the separation of an arterial and an "arteriovenous" phase. A display of the venous phase without superimposition of arteries is yet of interest for the evaluation of numerous vascular disorders.

Different postprocessing strategies have been proposed to deal with this task [12–19]. The most commonly applied is the simple subtraction of the arterial data sets from venous datasets. However, the signal-to-noise ratio (SNR) in the resultant image is reduced by a factor of if noise properties of the two images are similar. A method termed cross-correlation [12] was shown to be superior compared to the subtraction method both in terms of artery/vein separation and SNR. With this technique, the signal intensity time course of a region-of-interest (ROI) placed within an artery (vein) is cross-correlated with the time courses of all acquired datasets. The cross-correlation as an index of similarity ideally yields an arteriogram (venogram) only. This technique also leads to an increase in SNR by a factor of about two with respect to the subtraction technique. The implicit assumption of this technique is that the temporal behavior of the arterial phase does not overlap with the temporal behavior of venous phase significantly. However, this assumption is not always fulfilled and an unwanted depiction of venous signal in the arteriogram and vice versa can be observed.

In this chapter, the theory of the cross-correlation method is revised, and an extension of this method, termed *double-reference cross-correlation*, is introduced.

## 2.2 Theory

### 2.2.1 Cross-correlation

The cross-correlation between a discrete test function $T$ and discrete reference function $R$ can be defined as:

$$c(T,R) = \frac{\sum_{i=0}^{N-1} \left(R(t_i) - \bar{R}\right)\left(T(t_i) - \bar{T}\right)}{\sqrt{\sum_{i=0}^{N-1} \left(R(t_i) - \bar{R}\right)^2} \sqrt{\sum_{i=0}^{N-1} \left(T(t_i) - \bar{T}\right)^2}}, \tag{2.1}$$

where N is the number of measured 3D volume datasets and $\bar{R}$, $\bar{T}$ are means of the corresponding series. The coefficient $c(T,R)$ is maximal if $T = R$.

The mean-detrended and normalized value of a function $T$ can be defined as:

$$\hat{T(t_i)} = \frac{T(t_i) - \bar{T}}{\sqrt{\sum_{i=0}^{N-1} \left(T(t_i) - \bar{T}\right)^2}}. \tag{2.2}$$

Defining $\hat{R}$ in a similar way, we obtain:

$$c(T,R) = \hat{T} \cdot \hat{R}, \tag{2.3}$$

which is the scalar product between the two vectors $\hat{T}$ and $\hat{R}$. The correlation coefficient $c$ is always in the interval $[-1,1]$, being the scalar product between two vectors of unit norm. In general, the correlation coefficients are the cosine of the angle between the reference and test vector in N-dimensional space of the discrete time courses. Because of the normalization procedure of the test vector, the temporal behavior of the signal (for e.g. vascular structure) as well as background falls into the same dynamic range. This is undesirable as it discards the actual signal strength information (gray level value in the original image) of the test vector. Hence, in order not to lose SNR in the resultant correlation map, the scalar product between the normalized reference vector and non-normalized test vector is computed, ie $\tilde{T}(t_i) = T(t_i) - \bar{T}$.

Thus, the formula for correlation coefficients becomes:

$$c(T,R) = \tilde{T} \cdot \hat{R}. \tag{2.4}$$

### 2.2.2 Double-reference cross-correlation

With the standard cross-correlation technique, the cross-correlated coefficient can be interpreted as the length of the projection of the time course of the test vector on the axis of the reference vector. The correlation maps obtained with respect to arterial reference and venous reference are treated as independent of each other. However, because

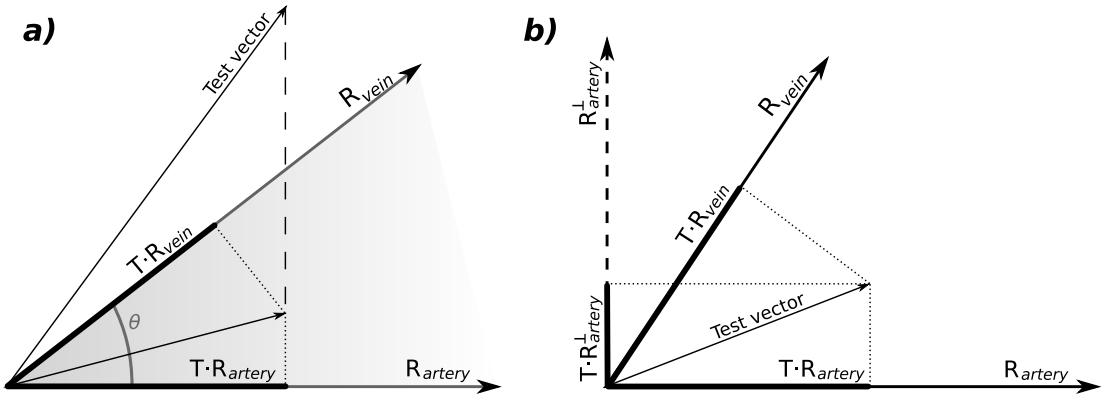


Figure 2.1: *a)* Vector representation of correlation coefficients in the standard cross-correlation technique. The correlation coefficients are projections of the test vector on the reference axes. The test vector components that are not coplanar with the references are discarded in the projection process. The "skew angle" $\theta$ is also shown. *b)* Orthogonal transformation of reference system. From the projection of test vector on the arterial and venous reference another coefficient is calculated, corresponding to the projection of vector on the axis normal to the arterial reference.

of significant overlapping of arterial and venous phase, there is sometimes a mutual dependency between the two correlation maps. In this case the arterial and venous reference time courses become similar to each other, and therefore the resulting correlation maps will show little difference. In the double-reference cross-correlation technique this dependency is decoupled by formulating the relation between the considered reference vectors. The aim of this approach is to classify a voxel as "arterial" or "venous" as the result of a comparison between the measures of similarity of the voxel time course with the arterial and venous references, represented by the standard cross-correlation maps. The classifier also uses a "soft margin" approach instead of a hard thresholding in order to take into account for voxels with mixed arterial and venous time courses. The classification is obtained through a nonlinear transformation of the correlation maps and through an application of an RGB color map to the transformed values.

Consider a 2-dimensional subspace formed by two reference vectors, which is called as "vessel plane". The two reference vectors form on this plane an angle $\theta = \arccos(R_{artery}, R_{vein})$ that is given by the arc cosine of the correlation coefficient between the references, which we termed as "skew angle" (see Fig. 2.1*a*).

The length of the projection vector of time course of the test vector onto this plane gives the signal strength information. The direction angle comparison with the skew angle indicates whether it is a part of an artery or a vein. The coordinates of projection vector in this plane are the cross-correlation coefficients $c(T, R_{artery})$ and $c(T, R_{vein})$ of the time course of the test vector obtained with respect to arterial reference and venous reference, respectively.

Thus, the calculation of length and direction of any vector in the vessel plane can be

performed provided its cross-correlation coefficients are known. In order to simplify this algebraic manipulation, the vessel plane is converted into an orthonormal (rectangular) coordinate system. Although any arbitrary orthonormal system can be chosen, for simplicity an orthonormal system formed by $(R_{artery}, R^{\perp}_{artery})$ is chosen (Fig. 2.1*b*). The coordinates of any vector in the new orthonormal system can be calculated from the correlation coefficients using the coordinate transformation formula given by

$$\begin{bmatrix} T_{R_{artery}} \\ T_{R^{\perp}_{artery}} \end{bmatrix} = \begin{bmatrix} 1 & 0 \\ -\cot(\theta) & \csc(\theta) \end{bmatrix} \begin{bmatrix} c(T, R_{artery}) \\ c(T, R_{vein}) \end{bmatrix} \tag{2.5}$$

where $T_{R_{artery}}$ and $T_{R^{\perp}_{artery}}$ are coordinates of the test vector in the new orthonormal reference system, and $\theta$ is the skew angle. The calculation of the length and direction of any vector in this rectangular coordinate system may be done by converting it into a polar coordinate system. The rectangular to polar coordinate transformation is given by:

$$r = \sqrt{(T_{R_{artery}})^2 + (T_{R^{\perp}_{artery}})^2}, \tag{2.6}$$

$$\alpha = \mathbf{sign}(T_{R^{\perp}_{artey}}) \arccos\left(\frac{T_{R_{artery}}}{r}\right), \tag{2.7}$$

where $0 \leq r < \infty$ and $-\pi < \alpha \leq \pi$. In order to form an image from length $r$ and direction angle $\alpha$, colormap encoding may be used.

### 2.2.3 RGB Encoding

Color maps have more degrees of freedom as compared to gray-level maps. For example, an RGB map synthetically represents three gray-level maps in one image. In the present case, two scalar values, the vector length $r$ and the direction angle $\alpha$ corresponding to each voxel are encoded using RGB colormap. The RGB colormap encoding leads to simultaneous visualization of both arteriogram (red) and venogram (blue); otherwise impossible with gray-level encoding.

The parameter $\alpha$ is an angle between a vector and the arterial reference in an orthogonal system formed by arterial and venous reference. Hence, it indicates the proximity of that vector with either the arterial reference or the venous reference. The comparison of the bisector of skew angle between arterial reference and venous reference and $\alpha$ categorizes the vector as part of an arteriogram (red) or a venogram (blue). If $\alpha$ is much higher than the arterial or venous reference direction angle, the voxel is identified as noise and mapped as background signal (black). Parameter $r$ represents the length of the projection of the test vector onto the vessel plane. Therefore, it is directly mapped as brightness of the voxel.

Figure 2.2 shows the color assigned to each vector lying on the vessel plane using the RGB color map. The region in proximity to the bisector of skew angle appears purple in color due to mixed mapping of red and blue colors.

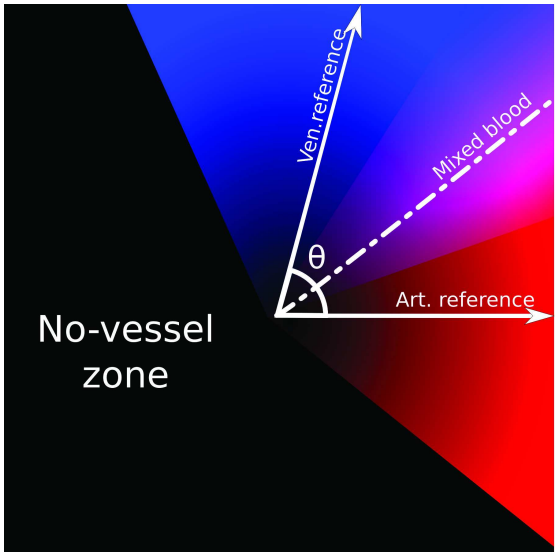


Figure 2.2: RGB color encoding of the vessel plane. The skew angle $\theta$ is indicated as the angle between the reference directions. Four zones are identified in the plane, a pure arterial blood zone (red), where phase ranges from $-\theta/2$ to $\theta/4$; a mixed blood zone (purple), with range $\theta/4$, $3/4\theta$; a pure venous blood zone (blue), with range $3/4\theta$, $3/2\theta$; and a "no vessel" zone (black), ranging outside the aforementioned ones.

## 2.3 Implementation

The double reference cross-correlation algorithm was implemented as ANSI C plug-ins for Matlab (The Mathworks Inc., Natick, MA). All programs were implemented on a 64-bit personal computer with 2 GB of RAM running GNU/Linux (kernel version 2.6.12) operating system. The effective computation time with this configuration was less than a minute for each dataset. In order to improve the workflow in a clinical environment, a user interface based on Qt graphic libraries (Nokia Qt Software, Norway) was specifically developed, which included a database interface where DICOM information was stored, and an interface to select the datasets to use for analysis (see fig. 2.3).

The algorithm requires the selection of reference time courses for arteries and veins. This can be done manually by a specific user interface (fig. 2.4), by selecting points in easily-identifiable vessels (carotid artery and superior sagittal sinus), or by using a clustering algorithm (described in chapter 3) that automatically identifies the reference time courses.

## 2.4 Experiments

To evaluate the double reference cross-correlation technique, ten randomly chosen time-resolved 3D cerebral CE-MRA datasets from patients in whom neurovascular disease was ruled out by MR and MRA workup were included in this analysis. In addition,

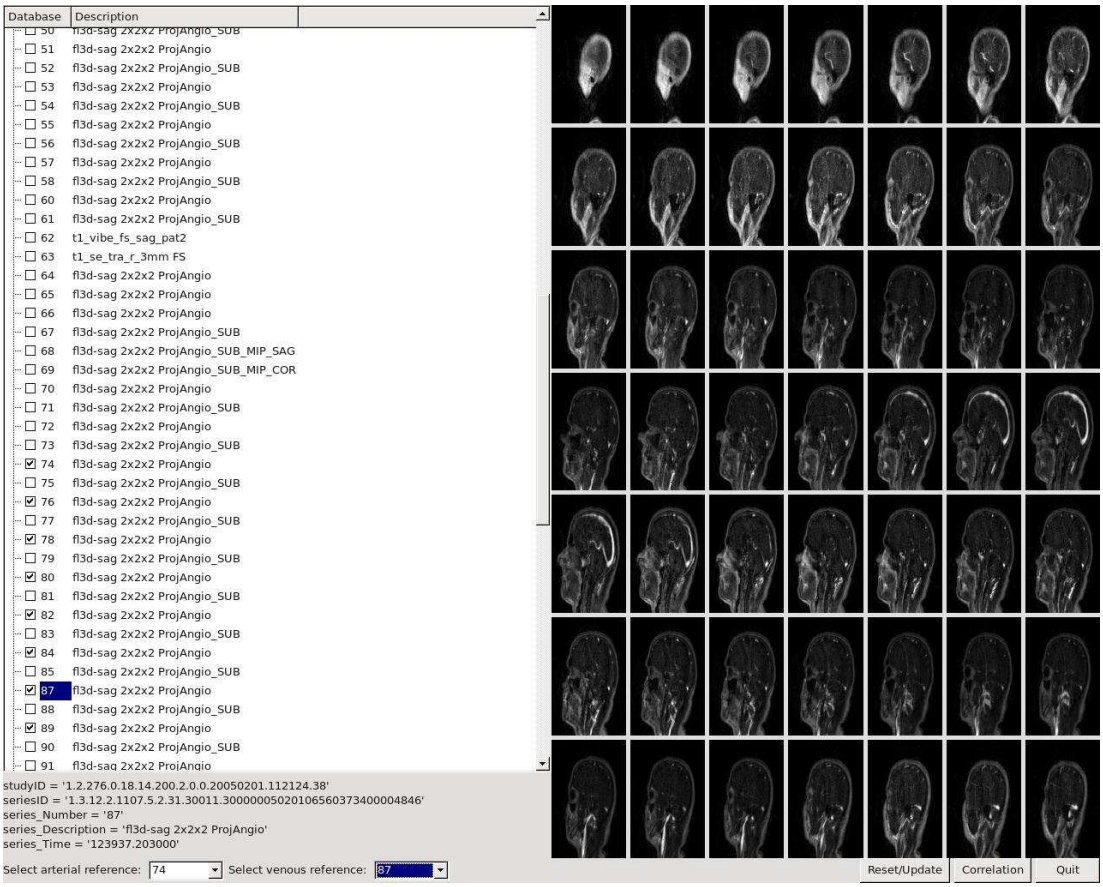


Figure 2.3: Dataset selection interface, with previews. It also include some basic DICOM functionality (DICOM send, save to disk, delete).

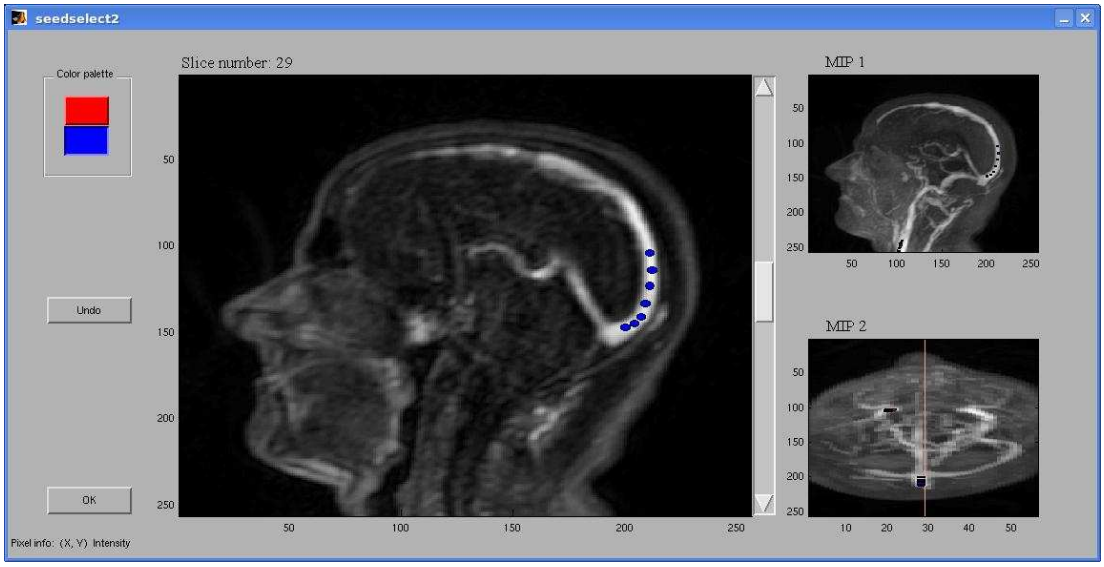


Figure 2.4: Interface for manual selection of reference points.

two datasets from patients with a cerebral dural arteriovenous fistula as proven by DSA were included. This retrospective analysis of the patient data was approved by the local ethics board.

### 2.4.1 MRI image acquisition

Cerebral time-resolved 3D-MRA datasets used for this study were acquired using 3D FLASH sequence implemented on a 1.5T MRI system (Magnetom Avanto, Siemens Medical Solutions, Erlangen, Germany) as described by Meckel et al [6,7]. An in-plane resolution of 2.0 mm x 2.0 mm with a slice thickness of 2.2 mm and a temporal resolution of 1.5 sec per 3D dataset were obtained. A single bolus of contrast agent (0.5 molar Gadolinium-DOTA) was administered using a power injector (20 ml, 3 ml/s) followed by a saline flush. In total, a series of 25 3D-datasets were acquired in 37.5 seconds, where the acquisition of the first dataset was started simultaneously with the injection of the contrast agent bolus.

To evaluate the effect of time resolution on the separation performance, one dataset was downsampled from the original time resolution (1.5s) to lower sampling periods (3.0s, 4.5s, 6.0s and 7.5s) to mimic multiple acquisitions at different time resolutions. The cross-correlation and the double-reference correlation algorithms were then independently applied on all obtained datasets.

In order to directly compare the results of the double-reference correlation algorithm with the cross-correlation technique, graylevel maps were also calculated from the RGB images. This was achieved by alternatively selecting the red channel and the blue channel information for direct comparison with the standard cross-correlation algorithm and quantitative analysis.

### 2.4.2 Data analysis and quality assessment

The results of the double-reference correlation algorithm were presented to two experienced radiologists for qualitative evaluation as red-green-blue maximum intensity projection images. They were asked to decide whether the artery/vein separation was correct, and to identify and describe possible pathologies.

Quantitative assessment of the separation efficiency was evaluated by calculating the contrast between arteries and veins in the arterial and venous graylevel maps. For this purpose, the sagittal maximum intensity projections (obtained with the double-reference correlation and with the cross-correlation algorithms) were calculated, and ROIs were selected in the arteries of the circle of Willis and in the superior sagittal sinus. Special attention was taken so to select areas where arteries and veins do not overlap in the projection. The mean intensities of the ROIs were calculated in the calculated arterial map and in the calculated venous map. The contrasts were calculated as artery/vein intensity ratio between the values obtained from the arterial map, and as vein/artery intensity ratio between the values obtained from the venous map. With this method, four values were obtained for each dataset, i.e. $AV_{DRC}$, $AV_{CC}$, $VA_{DRC}$, $VA_{CC}$, respectively representing the artery/vein contrast in the double-reference correlation arterial map, the artery/vein contrast in the cross-correlation arterial map, the vein/artery contrast in the double-reference correlation venous map and the vein/artery contrast in the cross-correlation venous map. In case of perfect separation, these indices would all assume an infinite value. The results were compared by calculating the difference between the contrast obtained with cross-correlation and the contrast obtained with double-reference correlation, divided by the contrast of the cross-correlation algorithm.

## 2.5 Results

### 2.5.1 Visual assessment of the vessels

The radiologists reported a correct visual separation of arteries and veins using the double reference cross-correlation algorithm on all datasets. Examples are shown in figure 2.5 , representing arteriograms and venograms of five datasets, and in figure 2.6, where the results obtained with the double reference cross-correlation algorithm on the dataset of a normal subject are compared to the results deriving from the cross-correlation technique.

The improvement on the separation of arteries and veins was visually pronounced if the skew angle was low, indicating a high bolus dispersion, as shown in figure 2.7 . In both datasets from patients suffering from dural cerebral arteriovenous fistulas, the radiologists were able to identify, in accordance to the findings from DSA, four "functional" types of vessels, as shown in figure 2.8 . The arteries were depicted in red; the veins with normal (late) venous outflow in blue; the "arterialized" veins, i.e. the veins with early filling with arterial blood due to the fistula, and no normal venous outflow in red; veins that showed early filling with arterial blood but also late venous

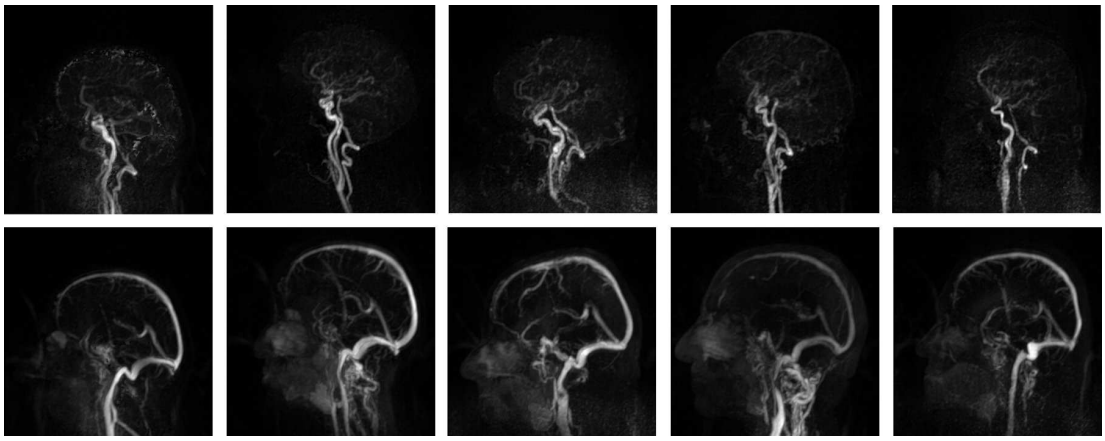

Figure 2.5: Sagittal grayscale MIPs of the arteriogram (top row) and venogram (bottom row) obtained by keeping alternatively the red and blue channel information of 3D RGB datasets of five normal subjects, computed with double-reference cross-correlation algorithm (skew angle values, from left to right: 44.0°,86.4°, 93.6°, 115.8°, 129.6°)

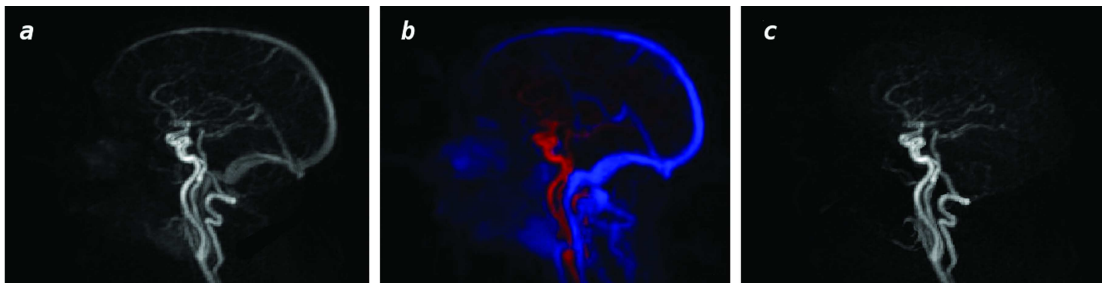


Figure 2.6: *a)* MIP (Maximum Intensity Projection) of arteriogram obtained using standard cross-correlation technique. In this case, the correlation value between arterial and venous reference was positive and a strong overlay of veins can be seen. *b)* Sagittal MIP representation of the entire angiogram of a normal subject, obtained using double reference cross-correlation algorithm. Red channel is used to depict arteriogram and blue channel is used to depict venogram. *c)* Sagittal MIP of the arteriogram. The image was computed from the 3-D RGB dataset generated by the algorithm by keeping the red channel information and displayed as a gray-scale MIP.

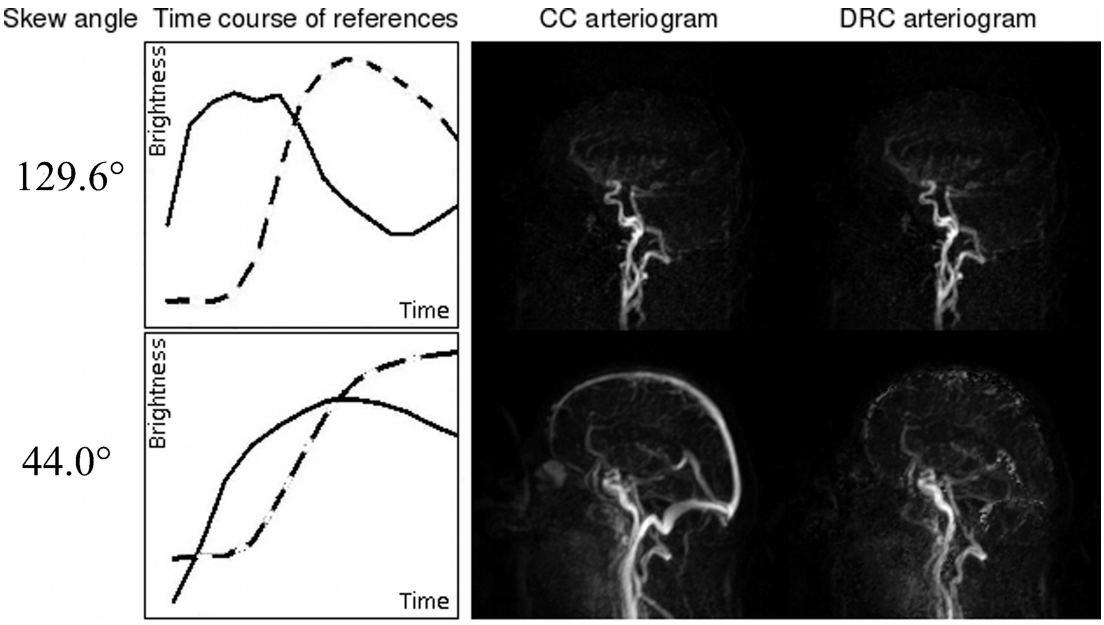


Figure 2.7: Different dispersion of contrast agent bolus in two subjects leads to different time courses of reference points (in solid line the arterial reference and in dashed line the venous reference). The upper panel shows that the standard cross-correlation (CC) and double reference cross-correlation (DRC) algorithms have similar performance when the skew angle is higher (129.6 degrees). The lower panel shows the performance of the two algorithms when the skew is lower (44.0 degrees) indicating dispersion is higher in level. In this case the standard cross-correlation algorithm almost completely fails in separating the vessels, while double reference cross-correlation succeeds, at the cost of lower SNR.

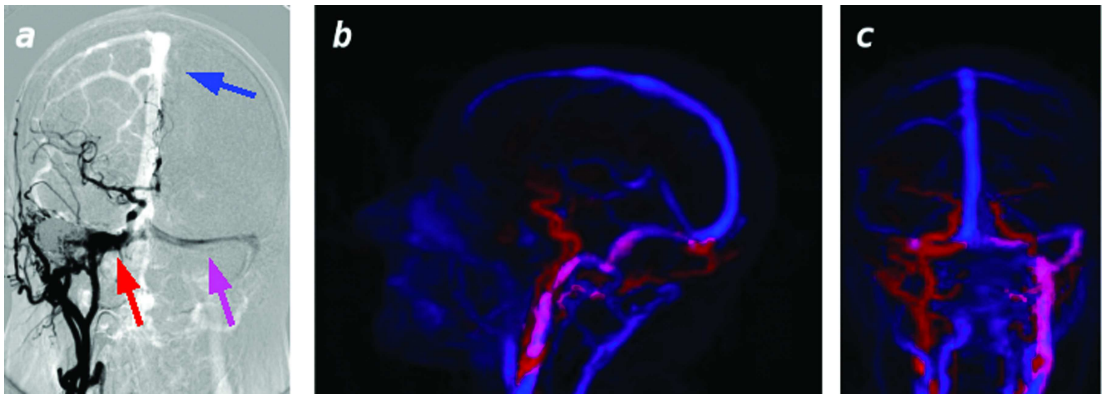


Figure 2.8: *a)* Mask subtracted conventional DSA image in anterior-posterior orientation of a patient with a dural fistula. The early appearing vessels appear black, the later ones white. Note that due to the fistula on the right side, the right transverse venous sinus appears early (red arrow) while the left transverse sinus shows a mixed black and white appearance (pink arrow). This indicates that shunted blood from the right side is mixed with the normal venous blood from the superior sagittal sinus (blue arrow). *b)* and *c)* Sagittal and Coronal MIP of a patient having a dural arteriovenous fistula involving the transverse sinus. The arteriovenous shunt is visible at the point where the occipital artery indicated in red enters into the right transverse sinus. The proximal part of the transverse sinus is depicted in red color indicating the arterialization of this vein. In addition, mixed blood flowing through the left jugular vein is highlighted in purple. The ipsilateral right jugular vein and sigmoid sinus is occluded after endovascular embolization therapy.

| Skew angle | $AV_{CC}$ | $AV_{DRC}$ | Change | $VA_{CC}$ | $VA_{DRC}$ | Change |
|---|---|---|---|---|---|---|
| 44.0° | 1.03 | 9.24 | 799.73% | 1.38 | 1.56 | 13.48% |
| 60.5° | 0.86 | 5.29 | 513.62% | 3.61 | 4.14 | 14.87% |
| 86.4° | 7.04 | 14.57 | 106.90% | 7.62 | 7.66 | 0.49% |
| 93.6° | 8.43 | 8.50 | 0.83% | 7.42 | 7.42 | 0.01% |
| 96.8° | 11.86 | 11.86 | 0.00% | 3.69 | 3.69 | 0.01% |
| 100.2° | 14.68 | 14.70 | 0.18% | 4.08 | 4.08 | 0.05% |
| 110.7° | 6.54 | 6.53 | -0.11% | 4.03 | 4.03 | -0.03% |
| 115.8° | 6.01 | 6.00 | -0.06% | 10.94 | 10.93 | -0.03% |
| 122.1° | 18.40 | 18.38 | -0.07% | 5.00 | 5.00 | 0.01% |
| 129.6° | 14.19 | 14.18 | -0.02% | 2.80 | 2.80 | 0.00% |

Table 2.1: Comparison between double reference cross-correlation (DRC) and standard cross-correlation (CC) algorithms for datasets of 10 different subjects having different values of skew angle.

outflow in purple.

### 2.5.2 Quantitative assessment

The performance of the double reference cross-correlation algorithm was compared in the non-pathological brain datasets with the standard cross-correlation algorithm by comparing the arteriogram artery/vein intensity ratio and the venogram vein/artery intensity ratio.

Out of ten analyzed datasets, three showed a skew angle smaller than 90°, which is the theoretical threshold for the performance decay of the cross-correlation algorithm, as described in the theory section.

In accordance to the qualitative results (figure 2.7), the performance for the double reference cross-correlation algorithm is significantly higher than for the standard cross-correlation algorithm at low skew angles ($<$90°), while both algorithms have similar performance (difference $<$1%) at higher skew angles (table 2.1).

As expected, the reduction in temporal resolution (increase of sampling period) of acquisition of the 3D MRA datasets also reduced the skew angle. As shown in table 2.2, the double reference correlation algorithm outperformed the cross-correlation algorithm at lower temporal resolutions. In particular, at the lowest temporal resolution (7.5s) the double reference cross-correlation had an improvement of up to 555% with respect to the standard cross-correlation algorithm.

| Time resolution | Skew angle | $AV_{CC}$ | $AV_{DRC}$ | Change | $VA_{CC}$ | $VA_{DRC}$ | Change |
|---|---|---|---|---|---|---|---|
| 1.5s | 86.4° | 7.04 | 14.57 | 106.90% | 7.62 | 7.66 | 0.49% |
| 3s | 79.6° | 2.70 | 13.21 | 388.41% | 6.81 | 7.02 | 3.12% |
| 4.5s | 74.5° | 1.95 | 11.83 | 506.28% | 5.87 | 7.14 | 21.77% |
| 6s | 68.1° | 1.54 | 7.98 | 418.52% | 4.52 | 7.74 | 71.21% |
| 7.5s | 48.8° | 0.93 | 6.10 | 555.81% | 2.52 | 5.24 | 67.94% |

Table 2.2: Separation performance of the double-reference correlation (DRC) algorithm compared to the standard cross-correlation (CC) algorithm for the same dataset sampled at different frame rates and thus having different skew angles. Top: separation performance for arteries; bottom: separation performance for veins.

## 2.6 Discussion

This chapter presented a postprocessing algorithm for the separation of arteries and veins in time resolved 3D CE-MRA datasets, termed double reference cross-correlation technique, an extension of the already established cross-correlation technique [12]. With this technique it was possible to improve the suppression of background structures and the separation of the arterial phase from the venous phase compared to the aforementioned technique. Utilizing RGB color encoding technique a display of mixed blood effect in fistulas was made, and a consistent and reliable 3D or MIP display of both arteriogram and venogram was provided.

As expected from the theoretical derivations, the performance of the double reference cross-correlation technique was equivalent to cross-correlation when the correlation between the two references is zero. When this correlation value is negative, the results are similar, provided that thresholding is applied to the output image of the cross-correlation algorithm. The advantage of the double reference cross-correlation technique over the standard cross-correlation technique can be appreciated when the correlation value between the two references is positive. This happens when the contrast agent bolus is dispersed due to subject's circulatory system characteristics or due to technical reasons, resulting in overlapping of the arterial and venous phase. An important feature of the double-reference correlation algorithm is the robustness towards lower time resolution of the acquired datasets, which leads to higher correlation between the references.

A drawback of this algorithm is that it does not allow a real-time implementation, requiring all time points to be acquired before the processing.

Various other postprocessing algorithms for artery/vein separation utilizing time resolved datasets are present in the literature [12, 16, 20]. All these algorithms rely on measuring the similarity between the time course of the dataset voxels with some reference function. Kim and Zabih [20] described an approach termed as "model based segmentation", in which the temporal behavior of each time-series pixel was compared

with a standard model such as straight line or series of straight lines. As a major advantage, this method required no manual selection of a reference ROIs as the reference waveform is a priori defined; however, this assumption, together with the assumption that the time series can be described as a series of straight lines, might lead to reduced performance in some cases as a tradeoff for the lesser need for user interaction.

Another approach for artery/vein segmentation is based on different types of connectivity algorithms [13–15, 17–19, 21], which utilizes a high resolution dataset to segment out the arteries and veins. It exploits the geometrical characteristics of the arterial and venous vessel trees, comparing the brightness of every voxel with its neighbors and thus deciding whether they belong to the same structure or not. Different decision-making algorithms lead to different implementations and different performances. Though similar in purpose, this class of techniques for artery/vein segmentation is very different from the class to which the double-reference algorithm belongs. In the former case, separation is obtained by pure image processing techniques and is directly related to the geometry of the acquired dataset, and not to the flow characteristics; it allows the acquisition of the MR dataset during the steady-state phase of the contrast agent, with longer scan times and higher resolution, because no time-resolved acquisition is needed. In the latter case, separation is obtained through the analysis of flow patterns as detected from a time-resolved scan, and therefore direct information about blood flow is obtained. For these reasons, direct comparison between these two classes of algorithms cannot be performed.

In conclusion, the results of the double-reference correlation technique were promising for the application to CE-MRA, as shown in the example of neurovascular applications. The ability of this algorithm to compensate for higher correlation between the selected reference time courses can be exploited to acquire datasets with lower time resolution and therefore higher spatial detail.

## References

[1] F. R. Korosec, R. Frayne, T. M. Grist, and C. A. Mistretta, "Time-resolved contrast-enhanced 3d mr angiography," *Magn Reson Med*, vol. 36, pp. 345–51, 1996. 0740-3194 (Print) Journal Article.

[2] M. R. Prince, "Contrast-enhanced mr angiography: theory and optimization," *Magn Reson Imaging Clin N Am*, vol. 6, pp. 257–67, 1998. 1064-9689 (Print) Journal Article.

[3] M. R. Prince and J. F. Meaney, "Expanding role of mr angiography in clinical practice," *Eur Radiol*, vol. 16 Suppl 2, pp. B3–8, 2006. 0938-7994 (Print) Journal Article Review.

[4] S. Naganawa, T. Ito, E. Iwayama, H. Fukatsu, T. Ishiguchi, T. Ishigaki, and N. Ichinose, "Magnitude subtraction vs. complex subtraction in dynamic contrast-enhanced 3d-mr angiography: basic experiments and clinical evaluation," *J Magn Reson Imaging*, vol. 10, pp. 813–20, 1999. 1053-1807 (Print) Journal Article.

[5] S. Aoki, T. Yoshikawa, M. Hori, A. Nanbu, H. Kumagai, Y. Nishiyama, H. Nukui, and T. Araki, "Mr digital subtraction angiography for the assessment of cranial arteriovenous malformations and fistulas," *AJR Am J Roentgenol*, vol. 175, pp. 451–3, 2000. 0361-803X (Print) Journal Article.

[6] S. Meckel, R. Mekle, C. Taschner, S. Haller, K. Scheffler, E. W. Radue, and S. G. Wetzel, "Time-resolved 3d contrast-enhanced mra with grappa on a 1.5-t system for imaging of craniocervical vascular disease: initial experience," *Neuroradiology*, vol. 48, pp. 291–9, 2006. 0028-3940 (Print) Journal Article.

[7] S. Meckel, M. Maier, D. S. Ruiz, H. Yilmaz, K. Scheffler, E. W. Radue, and S. G. Wetzel, "Mr angiography of dural arteriovenous fistulas: diagnosis and follow-up after treatment using a time-resolved 3d contrast-enhanced technique," *AJNR Am J Neuroradiol*, vol. 28, pp. 877–84, 2007. 0195-6108 (Print) Clinical Trial Comparative Study Journal Article.

[8] K. Noguchi, E. R. Melhem, T. Kanazawa, M. Kubo, N. Kuwayama, and H. Seto, "Intracranial dural arteriovenous fistulas: evaluation with combined 3d time-of-flight mr angiography and mr digital subtraction angiography," *AJR Am J Roentgenol*, vol. 182, pp. 183–90, 2004. 0361-803X (Print) Evaluation Studies Journal Article.

[9] K. Tsuchiya, C. Aoki, S. Katase, and J. Hachiya, "Mr digital subtraction angiography with three-dimensional data acquisition in the diagnosis of brain tumors: preliminary experience," *Magn Reson Imaging*, vol. 22, pp. 149–53, 2004. 0730-725X (Print) Journal Article.

[10] S. G. Wetzel, D. Bilecen, P. Lyrer, G. Bongartz, E. Seifritz, E. W. Radue, and K. Scheffler, "Cerebral dural arteriovenous fistulas: detection by dynamic mr projection angiography," *AJR Am J Roentgenol*, vol. 174, pp. 1293–5, 2000. 0361-803X (Print) Journal Article.

[11] S. Ziyeh, R. Strecker, A. Berlis, J. Weber, J. Klisch, and I. Mader, "Dynamic 3d mr angiography of intra- and extracranial vascular malformations at 3t: a technical note," *AJNR Am J Neuroradiol*, vol. 26, pp. 630–4, 2005. 0195-6108 (Print) Journal Article.

[12] M. Bock, S. O. Schoenberg, F. Floemer, and L. R. Schad, "Separation of arteries and veins in 3d mr angiography using correlation analysis," *Magn Reson Med*, vol. 43, pp. 481–7, 2000. 0740-3194 (Print) Journal Article.

[13] T. Lei, J. K. Udupa, P. K. Saha, and D. Odhner, "Artery-vein separation via mra–an image processing approach," *IEEE Trans Med Imaging*, vol. 20, pp. 689–703, 2001. 0278-0062 (Print) Journal Article.

[14] T. Lei, J. K. Udupa, P. K. Saha, D. Odhner, R. Baum, S. K. Tadikonda, and E. K. Yucel, "3d mra visualization and artery-vein separation using blood-pool contrast agent ms-325," *Acad Radiol*, vol. 9 Suppl 1, pp. S127–33, 2002. 1076-6332 (Print) Journal Article.

[15] T. Lei, J. K. Udupa, D. Odhner, L. G. Nyul, and P. K. Saha, "3dviewnix-avs: a software package for the separate visualization of arteries and veins in ce-mra images," *Comput Med Imaging Graph*, vol. 27, pp. 351–62, 2003. 0895-6111 (Print) Journal Article.

[16] A. L. Martel, D. Fraser, G. S. Delay, P. S. Morgan, and A. R. Moody, "Separating arterial and venous components from 3d dynamic contrast-enhanced mri studies using factor analysis," *Magn Reson Med*, vol. 49, pp. 928–33, 2003. 0740-3194 (Print) Journal Article.

[17] R. M. Stefancik and M. Sonka, "Highly automated segmentation of arterial and venous trees from three-dimensional magnetic resonance angiography (mra)," *Int J Cardiovasc Imaging*, vol. 17, pp. 37–47, 2001. 1569-5794 (Print) Journal Article.

[18] X. Tizon and O. Smedby, "Segmentation with gray-scale connectedness can separate arteries and veins in mra," *J Magn Reson Imaging*, vol. 15, pp. 438–45, 2002. 1053-1807 (Print) Journal Article.

[19] C. M. van Bemmel, L. J. Spreeuwers, M. A. Viergever, and W. J. Niessen, "Level-set-based artery-vein separation in blood pool agent ce-mr angiograms," *IEEE Trans Med Imaging*, vol. 22, pp. 1224–34, 2003. 0278-0062 (Print) Clinical Trial Journal Article Validation Studies.

[20] J. Kim and R. Zabih, "Automatic segmentation of contrast-enhanced time resolved image series," *Journal of X-Ray Science and Technology*, vol. 9, pp. 1–11, 2000.

[21] H. E. Cline, C. L. Dumoulin, W. E. Lorensen, S. P. Souza, and W. J. Adams, "Volume rendering and connectivity algorithms for mr angiography," *Magn Reson Med*, vol. 18, pp. 384–94, 1991. 0740-3194 (Print) Journal Article.

# Chapter 3

# Automatic reference selection

An adapted version of this chapter is submitted to the Journal of Magnetic Resonance Imaging: Santini F, Schubert T, Patil S, Meckel S, Wetzel SG, Scheffler K, *Automatic reference selection for artery/vein separation from time-resolved 3D contrast-enhanced MRA datasets.*

## 3.1 Introduction

In this chapter, a method for automatic reference selection that is specially designed for usage with the double-reference cross-correlation algorithm introduced in chapter 2, and that is based on a modified version of the *k-means* clustering algorithm [1]. The proposed algorithm performs an approximate segmentation on a subset of the original time-resolved dataset, eventually identifying two clusters that minimize the intra-cluster correlation and maximize the inter-cluster correlation. The centroids of the identified clusters are used as reference for the double-reference correlation algorithm.

To evaluate the efficacy of the method, 10 time-resolved CE-MRA datasets of cerebral vessels, which were retrospectively selected from routine exams and showed no abnormalities, and 2 datasets from patients with dural arteriovenous fistulas were processed both manually and automatically. The quality of the extracted arteriograms and venograms was assessed independently by two radiologists who were blinded to the method for reference selection used to produce each dataset. In addition, both methods were evaluated for their diagnostic quality in vascular disease on the pathological datasets.

## 3.2 The clustering algorithm

The first step of the clustering algorithm consists of reducing the dimension of the original dataset, based on the signal variance. Considering the sparsity of an angiography dataset, voxels that show low signal variance over time are discarded, and a threshold is set so that only 1% of the dataset is retained.
On this 1%, a modified k-means clustering is performed. This procedure is explained as following:

1. Initialization of k arbitrarily-chosen vectors, which are the first estimation of the cluster centroids. In our algorithm the initial centroids are vectors of unit norm.

2. Every point in the dataset is assigned to one cluster by calculating the distance of it from all the centroids and selecting the one with minimum distance. In our implementation, eq. 4 is used as a measure of "inverse distance", meaning that the assignation is made based on maximum correlation value between the centroid unit vector and the dataset point.

3. The centroids are recalculated as the mean vector of all elements belonging to the corresponding cluster.

4. As an additional step, in our implementation of the algorithm, the length of the centroids is normalized in order to obtain unit vectors.

5. The algorithm iterates from step 2, until no more changes are made to cluster assignments.

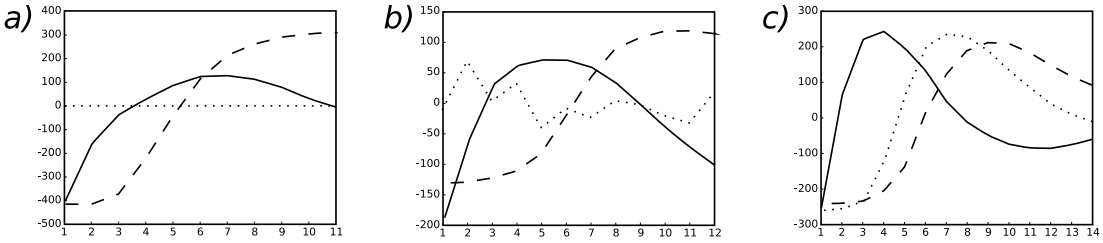


Figure 3.1: Cluster identification and rejection. Solid line is the arterial reference, dashed line is the venous reference, dotted line is the rejected cluster. The three plots show three different situations of identification of the third cluster: *a)* empty cluster; *b)* identification of static tissue (low-variance time course); *c)* identification of an intermediate time course.

Our implementation identifies three clusters to account for a possible cluster placed between the arterial and venous clusters. Examples of the three-cluster identification are shown in figure 3.1.

One of the three clusters is discarded by two criteria: if the variance of the centroid is significantly smaller than the other two (less than half of the smaller variance), then the cluster is discarded as it was not populated or only contains static tissue. If the variance is similar to the other two clusters, the two less-correlated clusters are kept. The centroid corresponding to a time course with shorter time-to-peak is selected as arterial reference, and the other as venous reference.

## 3.3 Acquisition and analysis

The datasets used for the testing of the algorithm were the same described in chapter 2 (see section 2.4.1).

The datasets were processed by applying the double-reference cross-correlation algorithm twice, once with references selected manually by a trained operator (arterial reference time course was derived from voxels in the internal carotid artery, and venous reference time course from the superior sagittal sinus), and the second time with automatic reference selection.

The datasets were randomized with respect to the reference method used and presented in separate reading sessions to two radiologists as three-directional maximum intensity projection (MIP) images of the calculated angiograms. Arteriogram and venogram were shown on the same image through a red-green-blue color coding (showing arteries in red and veins in blue). For non-pathological datasets, the both readers rated each dataset on a scale from 1 to 5, with the following criteria: 1 = "optimal performance"; 2 = "good"; 3 = "fair"; 4 = "acceptable"; 5 = "poor". The optimal performance was achieved when all the vessels were correctly classified, and no artifact was visible on the final image; a score of 2 was assigned when some minor misclassifications in smaller vessels were visible without significant artifacts; a score of 3 was assigned

when some artifacts were visible without impairment of the diagnostic quality; a score of 4 indicated that artifacts impaired other diagnostic quality of the dataset, but major vessels could still be correctly separated; a score of 5 indicated failure of the separation algorithm, with errors even in the major vessels.

The results from both readers were pooled and a two-sample Kolmogorov-Smirnov statistical test was applied to the two distributions of ratings to determine if the difference in performance of the two methods was statistically significant. Both a two-sided test (testing the alternative hypothesis of inequality) and a one-sided test (testing the alternative hypothesis that one probability distribution is greater than the other) were performed.

Pathological datasets were not included in the rating, and were qualitatively evaluated in order to assess the accuracy of depiction of the arterialized venous vessels at the site of the arteriovenous shunt, and depiction of possible arterial and venous blood mixing conditions.

## 3.4 Results

The reference waveforms selected by the automatic algorithm were similar in shape to the manually selected ones, both for tight and disperse boluses (fig. 3.2).

The evaluation of the datasets showed a better average performance of the manual selection with respect to the automatic selection (average ratings were 1.95 and 2.10, respectively). However, this difference was not statistically significant, both using the two-sided test ($p = 1.00$) and the one-sided test ($p = 0.80$). A chart showing detailed results of the evaluation is shown in fig. 3.3.

Both algorithms achieved qualitatively similar results for the pathological datasets, correctly identifying the mixed arterial and venous blood condition (fig 3.4) and depicting arterialized veins with a similar accuracy.

## 3.5 Discussion

In this paper a method for automatic reference selection for correlation-based artery/vein separation methods was presented. This method is based on a modified implementation of the well-known *k-means* clustering algorithm. The original algorithm, in an unmodified version was already used by Mouridsen *et al. [2]* for a similar task (identification of the arterial input function for perfusion imaging).

With our implementation of this algorithm the standard criterion of minimizing the intra-cluster Euclidean distance was replaced with the maximization of the intra-cluster correlation value. This approach was chosen because it adopts the same distance measure subsequently used in correlation-based methods, thus creating clusters that are coherent with the final result of segmentation. Moreover, the correlation value gives a smaller weight to the time courses with smaller variance (i.e. static tissue), privileging higher-variance time courses (i.e. vessels).

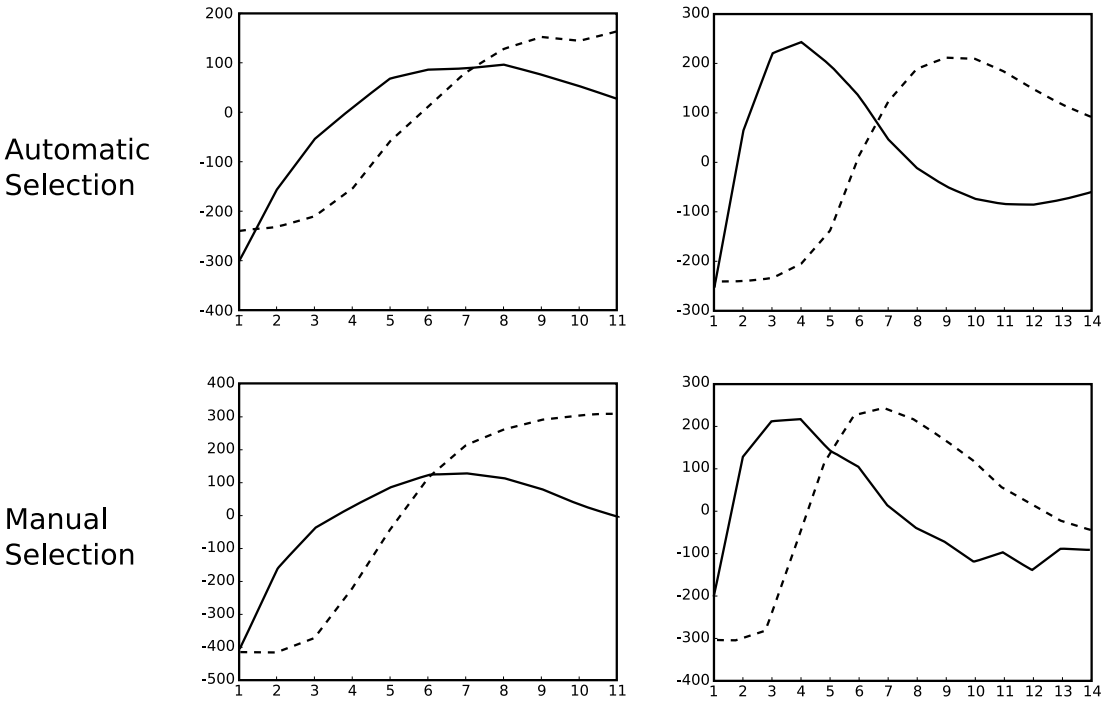


Figure 3.2: Manually and automatically selected reference time courses for arteries (solid line) and veins (dashed line) in cases of a subject with very disperse contrast agent bolus (left) and subject with tight bolus (right). X axis shows the dataset number (temporal progression) and Y axis shows signal intensity.

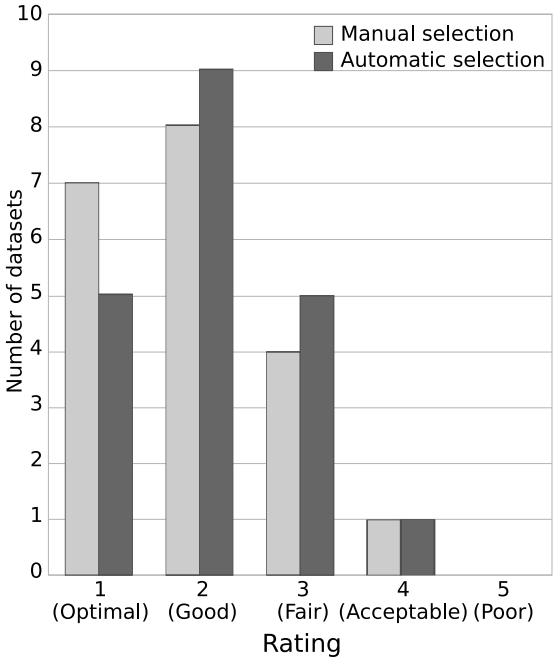


Figure 3.3: Quality evaluation of the segmented datasets. Each bar represents the number of datasets that received a specified rating.

Identification of three clusters was chosen instead of the more intuitive assumption of two-cluster identification (arteries and veins). This was necessary because many datasets contained voxels with time courses that presented both venous and arterial characteristics. This especially happened in pathological datasets with arteriovenous shunts, but also in normal subjects the time courses of venules and arterioles can be rather different from the major vessels. If only two clusters are identified, these voxel are randomly assigned to one or the other cluster, moving the centroid and generating two references with high mutual correlation.

This implementation of the clustering algorithm gave satisfactory results in all considered datasets. This allows for the implementation of an artery/vein separation algorithm that can run completely unsupervised, thus removing the bottleneck of human interaction and significantly reducing postprocessing times for CE-MRA datasets. In case the user is not satisfied with the final result, it can be refined by the manual selection of the reference points, which showed a marginally better average quality.

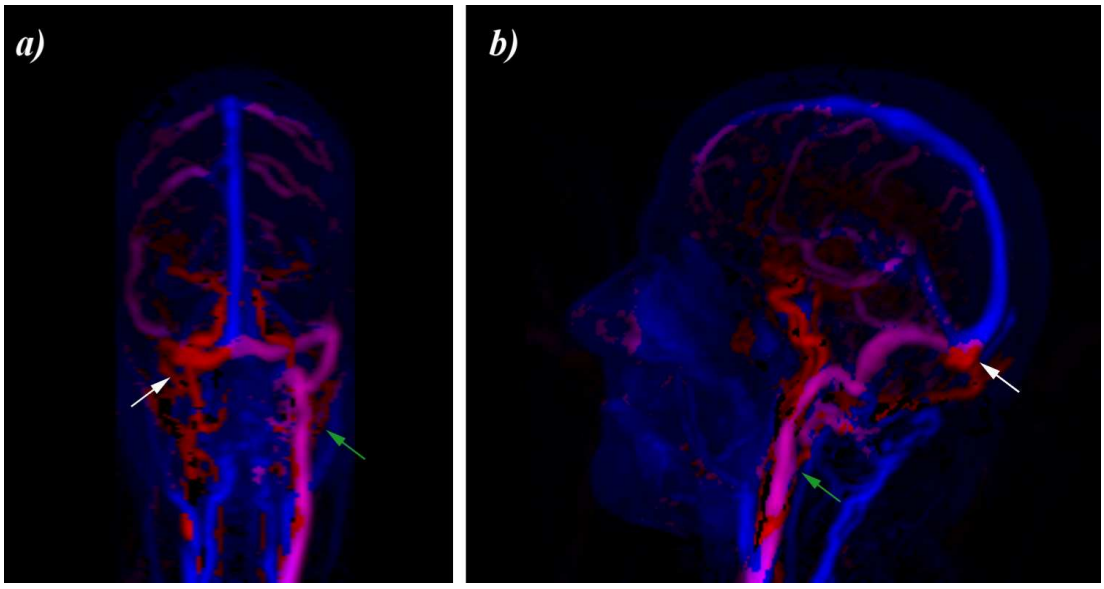


Figure 3.4: Maximum intensity projection of artery/vein separation with automatic reference, in a patient with a dural arteriovenous fistula (arteriovenous shunt from the right occipital artery to right transverse sinus); coronal (a) and sagittal (b) views. The separation correctly showed the arterialization of the right transverse sinus (white arrows) and the mixed arterial and venous blood flowing in the left transverse/sigmoid sinus and jugular vein (green arrows).

## References

[1] C. M. Bishop, *Pattern Recognition and Machine Learning*. Information Science and Statistics, New York: Springer, 2006.

[2] K. Mouridsen, S. Christensen, L. Gyldensted, and L. Ostergaard, "Automatic selection of arterial input function using cluster analysis," *Magn Reson Med*, vol. 55, pp. 524–31, 2006. Mouridsen, Kim Christensen, Soren Gyldensted, Louise Ostergaard, Leif Research Support, Non-U.S. Gov't United States Magnetic resonance in medicine : official journal of the Society of Magnetic Resonance in Medicine / Society of Magnetic Resonance in Medicine Magn Reson Med. 2006 Mar;55(3):524-31.

# Part II

# Flow quantification

# Chapter 4

# Quantitative time-resolved three-dimensional flow measurements with balanced SSFP

An adapted version of this chapter is in press as: Santini F, Wetzel SG, Bock J, Markl M, Scheffler K. *Time-resolved three-dimensional phase-contrast balanced SSFP*, Magnetic Resonance in Medicine, in press.

## 4.1 Introduction

In order to quantitatively measure flow velocities, which is useful information for the evaluation of both anatomy and function within the human circulatory system, e.g. the cardiovascular system and the cerebrospinal fluid (CSF) circulation system, the phase-contrast (PC) MRI technique can be used. It is based on the encoding of the mean velocity of an isochromat into the corresponding voxel location of the reconstructed phase image. An additional reference image is acquired to remove background effects via phase subtraction and the underlying fluid velocity or tissue motion is represented by the pixel intensity in the resulting phase difference image.

The traditional implementation consists of the acquisition of two-dimensional slices with a modified radiofrequency-spoiled sequence that is sensitive to flow in the through-plane direction [1]. More recently, time-resolved three-dimensional sequences, encoding flow in three directions, were proposed and used in research studies of thoracic and brain vessels [2–7]. Such data acquisition strategies allow for improved quantification of velocities, compared to single-direction flow encoding, which is biased if the flow is not completely parallel to the encoding direction. Furthermore, the acquisition of 3D volumes in combination with three-directional velocity encoding permits the visualization of complex flow patterns, and the estimation of other parameters such as wall shear stress or vorticity [8]. Although 3D methods suffer from longer scan times, three dimensional acquisitions also provide improved and potentially isotropic resolution related to the higher signal-to-noise ratio of a thick 3D slab compared to the signal obtained from a thin 2D slice.

One major disadvantage of typical flow quantification methods based on radiofrequency (RF) spoiled gradient echo sequences is tissue saturation that occurs when the repetition time TR is significantly shorter than T1, as in the case of blood and CSF. This disadvantage is particularly noticeable for three-dimensional acquisitions of large slabs or in cases of slow flow because of reduced in-flow enhancement. For this reason, and particularly for CSF flow which is more prone to tissue saturation, through-slice flow-sensitive balanced SSFP sequences were proposed [9–11].

Balanced SSFP (bSSFP) has the advantage of providing $T_2/T_1$ contrast for short TR, which results in high signal from blood and CSF. Nevertheless, for flow encoding, measures need to be taken in order to maintain the sensitive steady state of bSSFP. To avoid steady state disruptions leading to signal loss and artifacts as shown by Bieri and Scheffler [12], flow-related phase changes need to be rephased during each repetition time TR. Additionally, SSFP imaging requires short TR to minimize banding artifacts. Therefore, it is critical to optimize the gradient parameters to obtain the desired flow sensitivity while maintaining the shortest possible TR. Finally, stability of the bSSFP steady-state magnetization can be further enhanced by implementing intrinsic eddy current compensation into the sequence design.

In this chapter, the implementation of a time-resolved flow-sensitive 3D bSSFP sequence with three-directional velocity encoding is presented. Flow-sensitive bSSFP has to exhibit user-defined flow sensitivity at the echo time TE, and, at the same time,

has to be flow-compensated at the instants of excitation pulses. In the latter aspect, the bSSFP sequence differentiates from conventional phase-contrast sequences based on RF-spoiled gradient echo. To obtain exact gradient moments for all locations in k-space, a custom method for real-time calculation of gradient waveforms is introduced. Two eddy current compensation methods are implemented and compared: "k-space pairing", as proposed by Bieri *et al.* in [13], and "double-averaging", as presented by Markl *et al.* in [14].

*In vivo* results are presented, demonstrating the potential of flow-sensitive 3D bSSFP for the assessment of three-directional blood and CSF flow in intracranial regions. Measurements were performed with pulse sequences that normally result in low signal-to-noise ratio with standard RF-spoiled gradient echo sequences, i.e. a sagittal slab of the superior sagittal sinus for blood flow and a sagittal slab of the spine in the neck for CSF flow.

## 4.2 Optimized gradient waveforms

In a standard imaging sequence, the sampled location of the k-space is controlled by the zeroth moments $M_0$ of the gradients on the three spatial axes at acquisition time $T_a$, given by:

$$M_0 = \int_0^{T_a} G(t)dt, \tag{4.1}$$

where time 0 is considered as the center of the excitation RF pulse and $G(t)$ is the gradient amplitude over time. In a phase contrast sequence the velocity of a moving isochromat is encoded in the phase image as a phase shift equal to $\gamma v M_1$. Here, $\gamma$ is the gyromagnetic ratio of the proton, $v$ is the velocity of the isochromat in the direction of the flow sensitivity, and $M_1$ is the first moment of the gradient in the same direction, given by:

$$M_1 = \int_0^{T_a} G(t)tdt. \tag{4.2}$$

For phase-contrast imaging it is therefore crucial to control both $M_0$ and $M_1$ at the time of acquisition.
To take into account the hardware restrictions of a real MRI system, the constraints on $M_0$ and $M_1$ can be fulfilled by using a generic bipolar gradient waveform (see fig. 4.1 for variable definitions) characterized by the following moment equations :

$$\begin{cases} M_0 &= A_1(w_1 + r) + A_2(w_2 + r) \\ M_1 &= \frac{A_1}{2}\left(2r^2 + (3w_1 + 2t_0)r + (w_1 + 2t_0)w_1\right) + \\ & \quad +\frac{A_2}{2}\left(2r^2 + (3w_2 + 2\left(t_0 + 2r + w_1\right))r + \left(w_2 + 2\left(t_0 + 2r + w_1\right)\right)w_2\right) \end{cases} . \tag{4.3}$$

Equation system 4.3 can be inverted to obtain *A1* and *A2* as dependent variables:

$$\begin{cases} A_1 = \frac{(w_2+2w_1+2t_0+6r)M_0-2M_1}{(w_1+r)w_2+w_1^2+5rw_1+4r^2} \\ A_2 = -\frac{(w_1+2t_0+2r)M_0-2M_1}{w_2^2+(w_1+5r)w_2+rw_1+4r^2} \end{cases} . \tag{4.4}$$

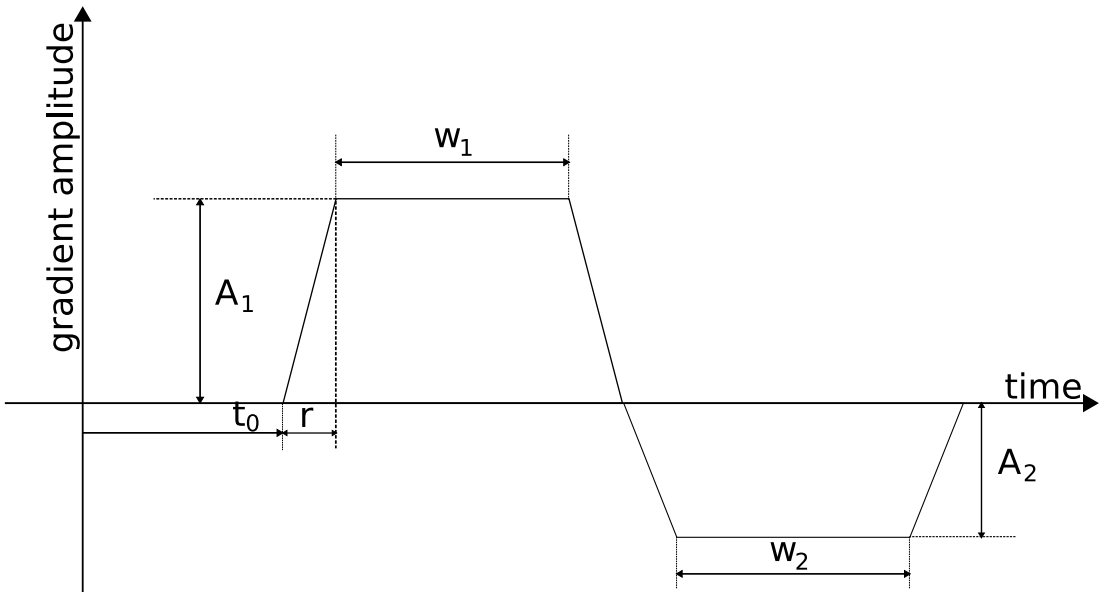


Figure 4.1: Generic bipolar gradient waveform. $A_1$, $A_2$: first and second lobe gradient amplitudes, $w_1$, $w_2$: first and second lobe flat top widths, $r$: gradient ramp times, $t_0$: gradient start time.

It is convenient to choose the amplitudes as dependent variables as they can generally be non-integer values.
To find the values for the parameters of equation system (4.4) that define gradient waveforms with the shortest possible total time, the following assumptions are made: $t_0$ is defined by sequence timings as an independent variable; $r$ is imposed as $\max(A)/s$, which is the minimum ramp time for a gradient to reach the maximum allowed amplitude. Based on these assumptions, $A_1$ and $A_2$ are quantities whose absolute values decrease when $w_1$ and $w_2$ increase, for any physically consistent values of $M_0$ and $M_1$, as shown in figure *4.2a*.
An iterative algorithm is used to identify the minimum values for $w_1$ and $w_2$ that generate a realizable gradient waveform (figure 4.3).
The algorithm ensures that the total time of the gradient waveform, given by $totalWidth + 4r$, is minimized. As shown in figure *4.2b*, $totalWidth$ as a function of $M_0$ and $M_1$ results in a convex-shaped surface. Therefore, the longest timing is needed when $M_0$ and $M_1$ are maximal, and the longest TR required by the sequence can be calculated at the edges of the k-space.

## 4.3 Sequence design

To implement a flow-sensitive bSSFP sequence, a generic sequence template was developed, consisting of a slice selection gradient, a readout gradient and generic bipolar

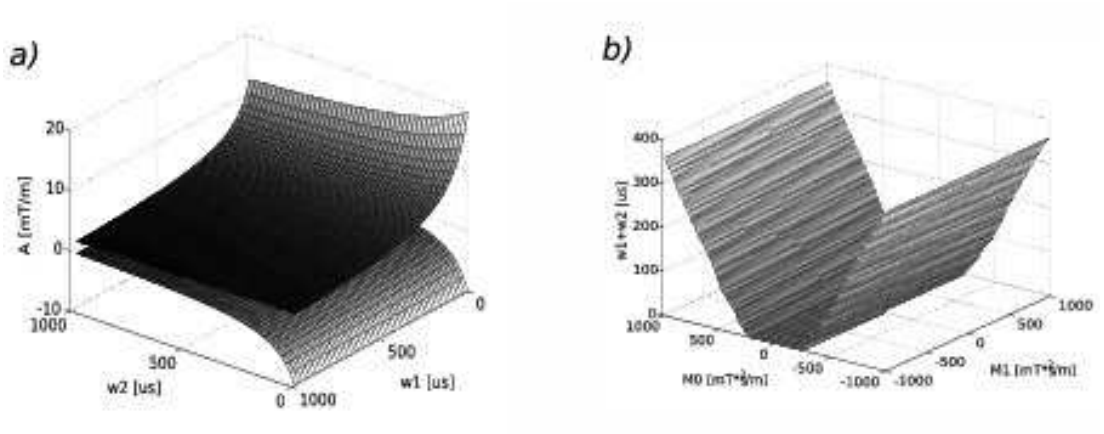


Figure 4.2: *a)* Behavior of gradient amplitudes $A_1$ (top surface) and $A_2$ (bottom surface) as functions of $w_1$ and $w_2$ for generic values of $M_0$ and $M_1$. *b)* Behavior of the minimum total gradient flat top width $w_1 + w_2$ as a function of $M_0$ and $M_1$.

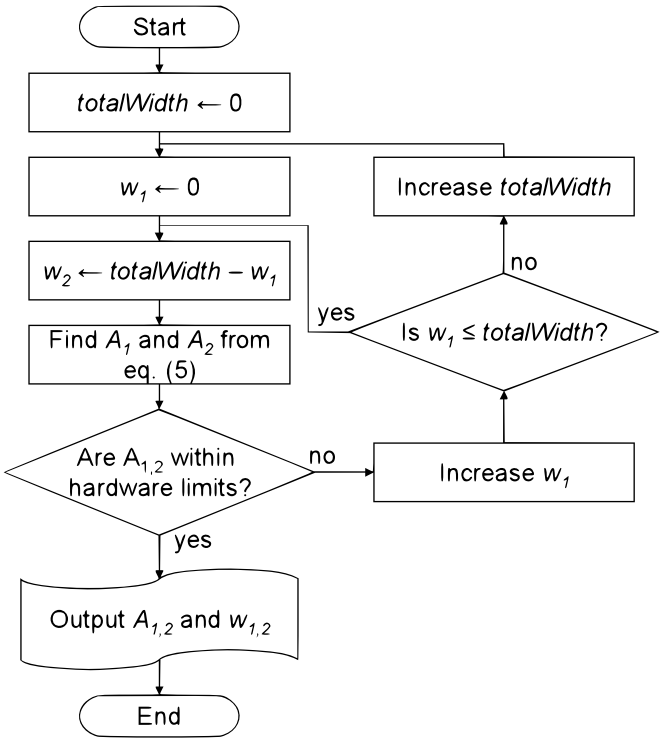


Figure 4.3: Flowchart describing the iterative algorithm used to obtain the optimal gradient parameters (see the text for a description of the symbols). The gradient timings are increased at each iteration by an amount defined by the scanner hardware characteristics.

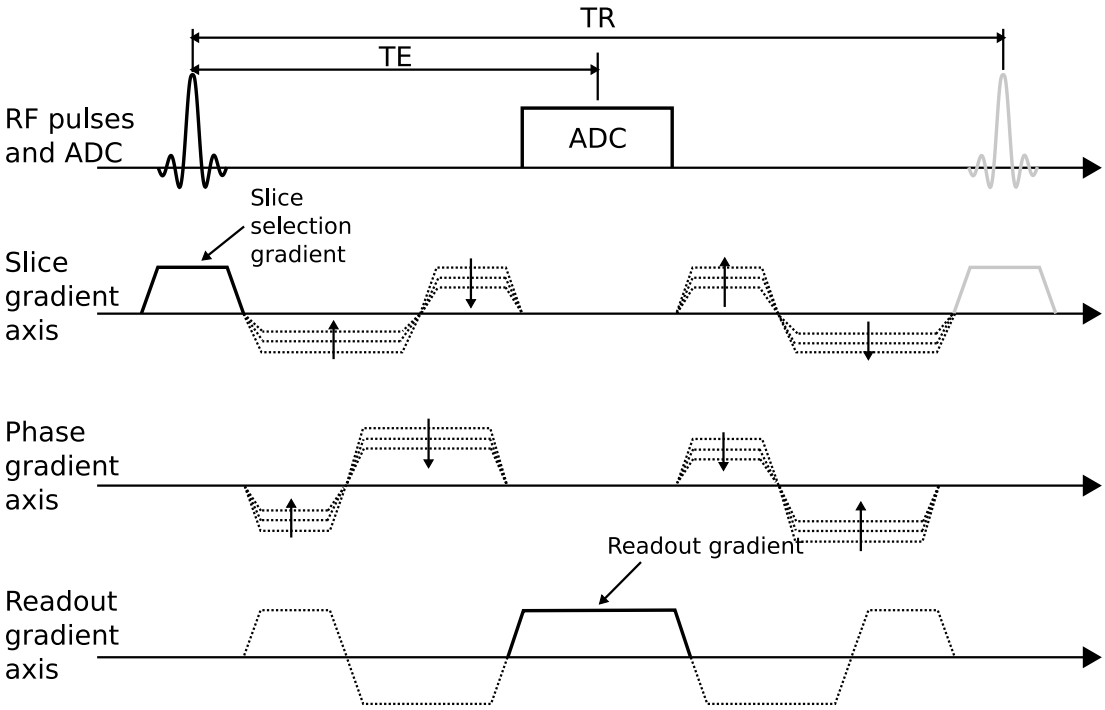


Figure 4.4: Flow-sensitive bSSFP sequence scheme. Gradient waveforms drawn in dashed lines are calculated with the proposed algorithm to satisfy the constraints on $M_0$ and $M_1$. Gradients drawn in solid lines are fixed in timings and amplitudes and depend on sequence parameters. The represented durations and amplitudes of the dashed waveforms are merely illustrative: the actual parameters are automatically calculated in real-time.

waveforms before and after the readout on all three gradient axes, as shown in figure 4.4. All gradient waveforms were calculated with the algorithm described above, to satisfy the following bSSFP-specific constraints:

1. $M_0 = 0$ at TR on all axes (to satisfy the definition of bSSFP).

2. $M_1 = 0$ at TR on all axes to provide flow compensation, needed to maintain the steady state as shown in [12, 15].

3. $M_0 = 0$ at TE on the readout axis to produce a gradient echo.

4. $M_0$ as required for phase/partition encoding at TE on phase/slice gradient axis.

5. $M_1 = \pi/\gamma \cdot v_{enc}$ at TE on all axes, where $\gamma$ is the gyromagnetic ratio and $v_{enc}$ is the desired velocity encoding anti-aliasing limit as described in 1.4.1.1.

### 4.3.1 Encoding scheme

For flow encoding balanced four-point velocity vector extraction described in [16] was chosen to maximize efficiency and signal-to noise ratio. Encoding was obtained on all axes at the same time, with alternatively positive and negative polarity. This allowed for the usage of smaller encoding moments since the encoding of the velocity on each axis was spanned over two different repetitions.

### 4.3.2 Eddy current compensation

In order to reduce artifacts generated by eddy currents, two compensation methods were implemented and compared. The first method is "k-space pairing" [13], i.e. performing each flow encoding step twice for two adjacent k-space lines. The acquisition of the second line is thus performed using similar gradient waveforms, which generates similar eddy currents. As a result, the spin population experiences two almost equal perturbations for two TRs. Due to sign alternation of the RF pulse in bSSFP imaging, the two successive perturbations mutually compensate, leading to reduced artifacts. This method introduces no penalty in the scan time, but does not completely eliminate artifacts, and imposes limits on the k-space trajectory. Figure 4.5*a* shows the acquisition scheme of the sequence implementing pairing.

The second implemented method is "double averaging" [14]: each flow encoding step is repeated twice at each k-space line. This guarantees that eddy currents are perfectly compensated over two TRs. As a result, scan time is doubled but no restrictions on the k-space trajectory are imposed. Parallel imaging algorithms can therefore easily be implemented to partially compensate for the increased scan time. The acquisition scheme for this sequence is shown in figure 4.5*b*.

### 4.3.3 Triggering

The sequence was executed with prospective cardiac triggering. For each time-frame all four encodings and two k-space lines were acquired, resulting in a temporal resolution of 8xTR. To maintain the steady state between successive RR-intervals, RF excitation was continued after the end of the acquisition of the last desired cardiac time-frame until the detection of the next trigger signal.

## 4.4 Acquisitions

### 4.4.1 Phantom studies

The sequence was tested on a static spherical phantom for image quality evaluation and on a custom flow phantom for validation.

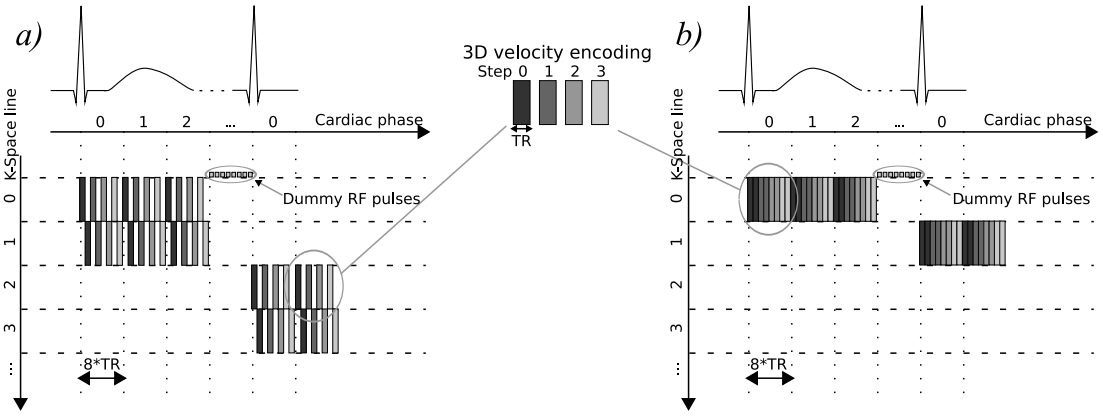


Figure 4.5: Flow encoding scheme. The four different gray levels correspond to the flow encoding steps along different directions. Before the EKG trigger dummy RF pulses are run in order to keep the steady state. *a)* "k-space pairing" implementation: every step is repeated on two adjacent k-space lines to avoid eddy current artifacts, *b)* "double-averaging" implementation: every k-space line is acquired twice.

#### 4.4.1.1 Static phantom

A single slice of a standard spherical saline solution phantom was scanned with a Venc of 10 cm/s (TE 6ms, TR 12ms, flip angle 60°, FOV 200x200mm$^2$, matrix size 256x256x1, spatial resolution 0.78x0.78x5 mm$^3$). Measurements were performed without eddy current compensation, with k-space pairing, and with double averaging, to evaluate general imaging quality and the efficiency of the chosen eddy current artifact suppression techniques.

#### 4.4.1.2 Flow phantom

Validation of flow encoding precision and accuracy was performed by using setup consisting of a steady flow pump, connected to 20 m of plastic tubing with 19 mm diameter via a quarter-turn regulating valve. The tube was deployed through the bore of the magnet, folded in a way that allowed both incoming and outgoing flow to be imaged in the field of view. Gd-doped water (0.25 mmol/L of Gd-DOTA), mimicking blood magnetic properties, was used in the circuit.

Two sets of MR images were obtained from the setup. The first dataset was acquired with a standard RF-spoiled gradient echo phase-contrast sequence, encoding flow in the through-plane direction, provided by the scanner manufacturer. A 2D slice with its normal vector aligned with the flow direction (Venc 100 cm/s, flip angle 15°, TR/TE 17.7/5.34 ms, resolution 1.17x1.17x5 mm$^3$) was used. The second dataset was acquired with the proposed sequence, with the same slice position and orientation but with a 3D acquisition (Venc 100 cm/s, flip angle 70°, TR/TE 12/6 ms, 8 partitions, and resolution 1.17x1.17x2 mm$^3$). The acquisition was repeated 10 times, at different openings of the regulating valve, from fully open to approximately 25% of the fully opened position.

Since the flow rate was constant during the scan, triggering was not activated and therefore the resulting datasets were not time-resolved.

#### 4.4.1.3 Data reconstruction and analysis

Data were reconstructed using a home built code (Matlab, The Mathworks, Natick, MA) including calculation of phase-contrast images. Two ROIs, one placed on the section of the tube with flow in the direction head-to-feet, and the other on the section of the tube with flow in the direction feet-to-head, were selected from each slice obtained from the gradient echo sequence and from the spatially corresponding 4th partition of the bSSFP sequence. Mean and standard deviation of measured phase differences and thus velocities were calculated over the ROIs. The results obtained with the gradient echo sequence were considered as reference, since the sequence is normally used in clinical routine. Linear regression was used to evaluate the performance of bSSFP compared to RF-spoiled GRE.

### 4.4.2 In vivo studies

In vivo experiments were performed on healthy volunteers. All datasets were acquired on a 1.5T Magnetom Avanto (Siemens Healthcare, Erlangen, Germany) scanner, with standard 12-channel head coil and neck coil (Siemens Healthcare, Erlangen, Germany). Maximum amplitude achievable by the gradient system was 28 mT/m and the maximum slew rate was 170 mT/(m*ms). Velocity sensitivity (Venc) ranged from 10cm/s (suitable for cerebrospinal fluid investigation) to 100cm/s (suitable for blood flow measurement). Double averaging was used as eddy current compensation method.

Ethical approval for this study was obtained from the local ethics committee and informed consent was obtained from all volunteers.

#### 4.4.2.1 Blood flow

Venous cerebral blood flow measurements (superior sagittal sinus and straight sinus) were performed in two healthy volunteers with the following imaging parameters: Venc 100cm/s, TE 4.8 ms, TR 9.6 ms, flip angle 70°, matrix size 128x128x10, spatial resolution 2.3x2.3x3 $mm^3$, temporal resolution 76.8 ms. Total scan time was dependent on heart rate, and was approximately 10 minutes.

#### 4.4.2.2 CSF flow

CSF flow measurements were performed in two healthy volunteers in the region of the neck, at the level of C3-C5 vertebrae, with the following imaging parameters: Venc 10cm/s, TE 6ms, TR 12ms, flip angle 70°, matrix size 128x128x22, spatial resolution 1.1x1.1x2$mm^3$, temporal resolution 86 ms. Total scan time was approximately 20 minutes.

#### 4.4.2.3 Postprocessing and visualization

Post-processing of the phase images was performed with a specialized tool written for the Matlab environment [17].

Noise masking, based on magnitude intensity, was applied and linear phase drifts and concomitant field effects were compensated by estimating the background phase from stationary regions, fitting it to a 2nd order 2D polynomial, and subtracting it from the phase images [18]. The modified images were further converted into three-dimensional datasets for import into commercial 3D visualization software (Ensight, CEI, Apex, NC). The tool also generated a phase-contrast angiogram.

Visualization of the 3D data was performed as described in [4, 6], with the usage of particle traces (traces of virtual massless particles released within the time-varying velocity field) and vector fields for 3D flow visualization and isosurfaces for the visualization of the vascular geometry [5].

## 4.5 Results

### 4.5.1 Image quality and eddy currents

The scanning of the static phantom showed that by implementing no eddy current correction method, the features of image were substantially obscured by artifacts (fig. 4.6*a*), whereas the pairing method resulted in a very faint residual ghosting artifact (fig. 4.6*b*), and no artifact was detectable with the double averaging method (fig 4.6*c*).

### 4.5.2 Flow phantom experiment

The quantitative comparison between velocities measured using the standard sequence (GRE) and the proposed sequence (bSSFP) demonstrated excellent agreement between both methods ($R^2 = 0.9981$, figure 4.7). The coefficient of proportionality was 0.948, thus leading to an underestimation bias in the accuracy of 5.2%. The precision of the measurement, shown by the standard deviation bars on the plot, was similar for both the techniques.

### 4.5.3 In vivo flow characteristics

The slow 3D venous blood flow in the superior sagittal sinus was successfully visualized using 3D particle traces. One volunteer presented an anatomical variation in which blood from the superior sagittal sinus flowed to the right transverse sinus only, and blood from the straight sinus was directed to the left transverse sinus. The sequence correctly depicted this anatomy (fig. 4.8). Maximum venous flow velocities of approximately 10 cm/s corresponded well to the physiological range as described in the literature [19].

The phase-contrast angiogram (yellow isosurfaces), derived from sum of squares of the velocities in all three directions, suffers from off-resonance-induced phase shifts and phase noise in the tissue of the outer skull, resulting in artifacts outside the vessels.

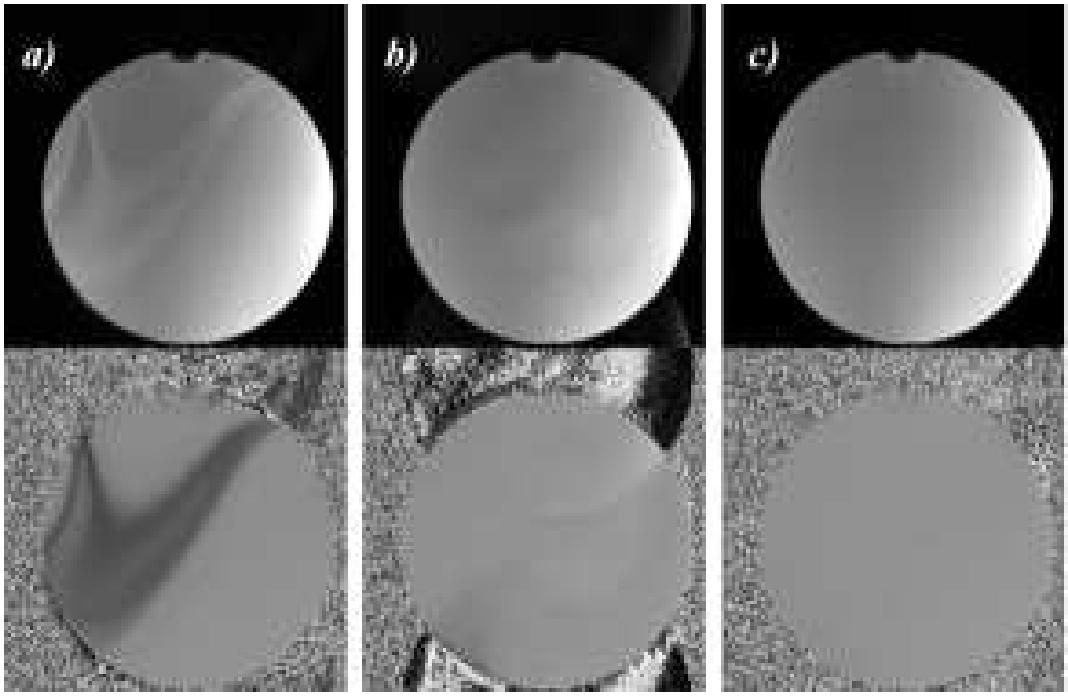


Figure 4.6: Spherical phantom scanned without eddy current compensation ($a$), with pairing ($b$) and with double averaging ($c$) using the flow-sensitive bSSFP sequence. Strong eddy current artifacts are visible in ($a$), whereas only a very faint ghosting artifact is visible on top of image ($b$), and no artifact is detectable in ($c$). Magnitude images are displayed in the top row; phase images in the bottom row.

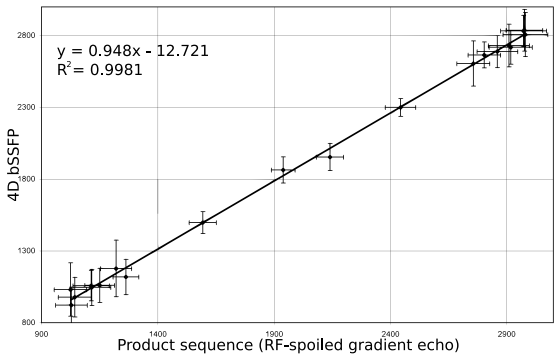


Figure 4.7: Plot of mean phase values over ROIs in the flow phantom setup measured with bSSFP sequence versus product RF-spoiled sequence. Plotted values are the gray levels of the phase-contrast images (range 0-4095). The standard deviation over the ROI is displayed as error bars. Linear fitting is shown as solid line.

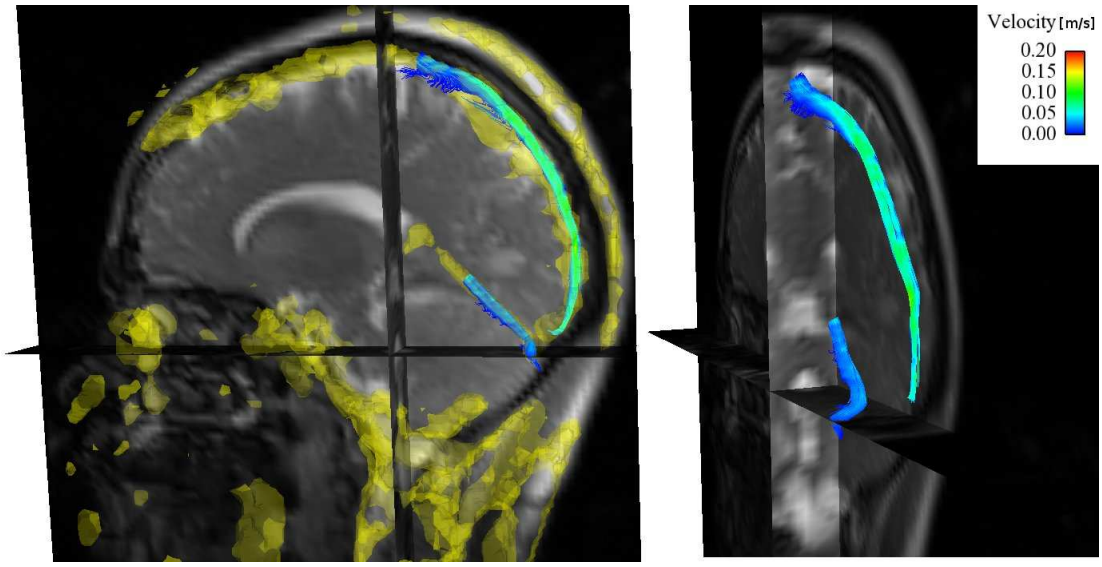


Figure 4.8: Streamline representation of blood flow in the superior sagittal sinus (red arrow) and straight sinus (light blue arrow), sagittal (left) and oblique coronal (right) views. The anatomical variant of the subject, showing that blood from the two sinuses does not mix, is visible. The structures depicted as yellow isosurfaces in the image on the left are the phase-contrast angiogram, suffering from artifacts deriving from phase shifts in the tissue of the outer skull.

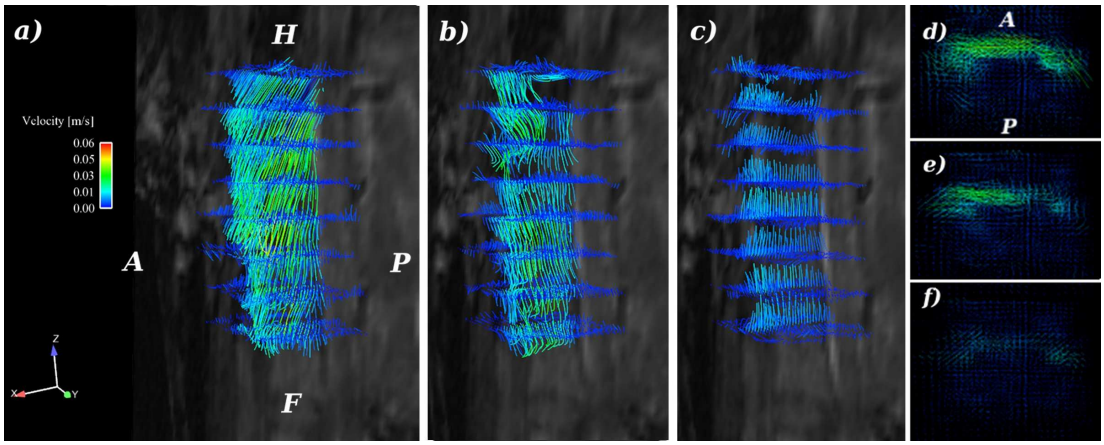


Figure 4.9: Streamlines representing CSF flow in the neck (C3-C5 sections). Eight planes are placed axially 5mm apart from each other and are chosen as emitters for the streamlines. Image view is oblique sagittal/coronal approximately 45° in the left/posterior direction (frames *a*, *b*, *c*) and axial (frames *d*, *e* and *f*). Antero-posterior and head-feet directions are represented by the A-P and H-F letters. The vectors represent magnitude and direction of velocities of each point at three different cardiac phases: second phase after R wave (*a*, *d*), third phase (*b*, *e*) and last phase (eighth phase – *c*, *f*). Non-negligible in-plane components are visible in the oblique view.

Measurements of CSF showed an initial cranio-caudally-directed flow followed by a caudo-cranial backflow during the last time-frame, as expected from the literature [20], and also in-plane flow components, as shown in figure 4.9.

## 4.6 Discussion

In this chapter, a pulse sequence for time-resolved, three-dimensional three-directional phase-contrast flow encoding, based on bSSFP, was presented. This sequence provides an alternative to RF-spoiled 3D gradient echo phase-contrast sequences, which are commonly used for velocity quantification in various parts of the body (3-7,22) [2, 4–7, 21].

Due to the long longitudinal relaxation time of blood and of other body fluids, RF-spoiled gradient echo sequences do not offer optimal contrast for imaging these tissues, particularly in cases of low flow velocities or thick imaging 3D slabs, for which inflow enhancement effects are negligible. This results in a strong saturation of magnetization and thus low signal-to-noise for both the magnitude and the phase images. In contrast, bSSFP is characterized by high signal for blood and especially CSF, and therefore provides a valid alternative for flow measurements.

For the flow cases analyzed in this study, the sequence could successfully be applied to acquire complex 3D flow patterns in-vivo even for slow venous and CSF flow. Measured velocities were within the physiological ranges. Nevertheless, a significant

underestimation of peak velocity of blood flow was found because of the low temporal resolution of 8xTR, compared to 4xTR for the conventional RF-spoiled gradient echo sequence. In order to overcome this problem, a new reconstruction method able to effectively improve the temporal resolution was developed, and presented in chapter 5.

In comparison with conventional bSSFP, relatively long repetition times are needed for this sequence. In addition to reduced temporal resolution longer TRs increase the off-resonance sensitivity of bSSFP imaging and may therefore also be a source of banding artifacts in regions with increased field inhomogeneity. In the experiments performed for this study in the regions of head and neck, we did not observe any impaired image quality in the desired region, especially if manual shimming of the magnetic field was performed. Field inhomogeneity can cause phase errors and singularities in the phase images where shimming is less accurate, which normally happens far from the region of interest. This can impair the accuracy of the phase contrast angiogram, as shown in figure 4.8.

The implementation of the sequence included the real-time calculation of the gradient waveforms which was necessary to achieve the same $M_1$ at TE for each k-space line and to ensure correct compensation at TR, which would otherwise disrupt the steady state. This approach is more computational demanding than the non-iterative approach proposed by Bernstein *et al.* [22], which is still widely used, but it is more flexible if custom moment values need to be achieved. Higher order moments are not controlled by this algorithm, so artifacts may arise in case of turbulent flow.

Two eddy current compensation methods were implemented in order to reduce artifacts in the final images: "k-space pairing" [13] and "double averaging" [14]. Both methods produced acceptable image quality, but double averaging offers the possibility for straightforward implementation of parallel imaging, due to the non-restricted k-space trajectory. Due to the high signal-to-noise ratio of fluids, parallel imaging could be useful to reduce total scan times without significant loss of precision in the flow measurement [23]. Since flow is confined to small regions (vessels, spinal canal) within the acquired volume, the application of other spatio-temporal accelerating techniques such as k-t BLAST, VIPR and variants thereof [24–26] is also possible.

In order to eliminate steady state artifacts, the sequence was designed to be flow-compensated at TR. This compensation needed additional gradients after data acquisition, which are usually not needed for RF-spoiled sequences. Furthermore, traditional bSSFP contrast is achieved when TE is equal to half of the TR, and this condition posed another constraint in the realization of the sequence, which needed longer TRs with respect to the RF-spoiled flow-sensitive sequence with equivalent parameters, as described in [27].

In order to reduce TR, a marginally more efficient implementation of the gradient optimization algorithm would consider constant slew rate $s = {}^{dA}/_{dt}$ instead of constant ramp times in equation system (4.3), imposing $r = {}^{|A|}/_{s}$. However, such a choice for maximal slew rate would result in equations that cannot be inverted through algebraic manipulation, making a direct mathematical solution of the problem impossible.

The experimental setup for the quantitative comparison of measured velocities was

chosen in order to maximize the SNR performance of the standard sequence provided by the manufacturer, i.e. exploiting in-flow effect at high flow rates and through-plane acquisition. The accordance of the result was excellent ($R^2 = 0.9981$), but a systematic error of 5.2% in the measurement of velocities was detected. We do not have access to the Siemens implementation of the standard sequence, so we cannot make precise assumptions on the origin of this discrepancy, but it can be corrected in a postprocessing step if needed.

In this study, the feasibility of 3D acquisition of CSF flow has also been demonstrated. This results showed that there are non-negligible in-plane velocity components within a transversal imaging slab, information not provided by earlier works using phase-contrast bSSFP for 2D, through-plane flow quantification of the CSF [10]. A more extensive study on the ventricular system is being performed, and preliminary results are shown in chapter (6).

In conclusion, the application of flow sensitive bSSFP allowed for the depiction of 3D flow patterns in tissues that show high signal in T2/T1-weighted sequence and low signal in T1-weighted sequences. Quantitatively, the results obtained were compatible with the physiological data present in the literature.

This technique is a valuable tool for the study of intracranial flow, especially to extend the knowledge of CSF circulation in healthy volunteers and in patients suffering from hydrocephalus [**?**, 28] and Chiari malformation.

## References

[1] E. M. Haacke, R. W. Brown, M. R. Thompson, and R. Venkatesan, *MR angiography and flow quantification*, pp. 703–741. New York: John Wiley & Sons, 1999.

[2] R. Bammer, T. A. Hope, M. Aksoy, and M. T. Alley, "Time-resolved 3d quantitative flow mri of the major intracranial vessels: initial experience and comparative evaluation at 1.5t and 3.0t in combination with parallel imaging," *Magn Reson Med*, vol. 57, pp. 127–40, 2007. 0740-3194 (Print) Comparative Study Evaluation Studies Journal Article Research Support, N.I.H., Extramural Research Support, Non-U.S. Gov't.

[3] D. N. Firmin, G. L. Nayler, P. J. Kilner, and D. B. Longmore, "The application of phase shifts in nmr for flow measurement," *Magn Reson Med*, vol. 14, pp. 230–41, 1990. 0740-3194 (Print) Journal Article Research Support, Non-U.S. Gov't.

[4] M. Markl, M. T. Draney, D. C. Miller, J. M. Levin, E. E. Williamson, N. J. Pelc, D. H. Liang, and R. J. Herfkens, "Time-resolved three-dimensional magnetic resonance velocity mapping of aortic flow in healthy volunteers and patients after valve-sparing aortic root replacement," *J Thorac Cardiovasc Surg*, vol. 130, pp. 456–63, 2005. 0022-5223 (Print) Comparative Study Journal Article Research Support, N.I.H., Extramural Research Support, Non-U.S. Gov't Research Support, U.S. Gov't, P.H.S.

[5] M. Markl, A. Harloff, T. A. Bley, M. Zaitsev, B. Jung, E. Weigang, M. Langer, J. Hennig, and A. Frydrychowicz, "Time-resolved 3d mr velocity mapping at 3t: improved navigator-gated assessment of vascular anatomy and blood flow," *J Magn Reson Imaging*, vol. 25, pp. 824–31, 2007. 1053-1807 (Print) Evaluation Studies Journal Article Research Support, Non-U.S. Gov't.

[6] S. Wetzel, S. Meckel, A. Frydrychowicz, L. Bonati, E. W. Radue, K. Scheffler, J. Hennig, and M. Markl, "In vivo assessment and visualization of intracranial arterial hemodynamics with flow-sensitized 4d mr imaging at 3t," *AJNR Am J Neuroradiol*, vol. 28, pp. 433–8, 2007. 0195-6108 (Print) Journal Article.

[7] S. Yamashita, H. Isoda, M. Hirano, H. Takeda, S. Inagawa, Y. Takehara, M. T. Alley, M. Markl, N. J. Pelc, and H. Sakahara, "Visualization of hemodynamics in intracranial arteries using time-resolved three-dimensional phase-contrast mri," *J Magn Reson Imaging*, vol. 25, pp. 473–8, 2007. 1053-1807 (Print) Journal Article.

[8] S. Meckel, A. F. Stalder, F. Santini, E. W. Radu, D. A. Rufenacht, M. Markl, and S. G. Wetzel, "In vivo visualization and analysis of 3-d hemodynamics in cerebral aneurysms with flow-sensitized 4-d mr imaging at 3 t," *Neuroradiology*, vol. 50, pp. 473–84, 2008. Meckel, Stephan Stalder, Aurelien F Santini, Francesco Radu, Ernst-Wilhelm Rufenacht, Daniel A Markl, Michael Wetzel, Stephan G Research Support, Non-U.S. Gov't Germany Neuroradiology Neuroradiology. 2008 Jun;50(6):473-84. Epub 2008 Mar 19.

[9] M. Markl, M. T. Alley, and N. J. Pelc, "Balanced phase-contrast steady-state free precession (pc-ssfp): a novel technique for velocity encoding by gradient inversion," *Magn Reson Med*, vol. 49, pp. 945–52, 2003. 0740-3194 (Print) Comparative Study Journal Article Research Support, Non-U.S. Gov't Research Support, U.S. Gov't, P.H.S.

[10] E. J. McCormack, M. R. Egnor, and M. E. Wagshul, "Improved cerebrospinal fluid flow measurements using phase contrast balanced steady-state free precession," *Magn Reson Imaging*, vol. 25, pp. 172–82, 2007. 0730-725X (Print) Journal Article Research Support, Non-U.S. Gov't.

[11] J. F. Nielsen and K. S. Nayak, "Pulse sequences for phase-contrast ssfp imaging from a single steady-state," *Proc Int Soc Magn Reson Med Sci Meet Exhib Int Soc Magn Reson Med Sci Meet Exhib*, vol. 14, p. 879, 2006. 1524-6965 (Print) Journal article.

[12] O. Bieri and K. Scheffler, "Flow compensation in balanced ssfp sequences," *Magn Reson Med*, vol. 54, pp. 901–7, 2005. 0740-3194 (Print) Evaluation Studies Journal Article Research Support, Non-U.S. Gov't.

[13] O. Bieri, M. Markl, and K. Scheffler, "Analysis and compensation of eddy currents in balanced ssfp," *Magn Reson Med*, vol. 54, pp. 129–37, 2005. 0740-3194 (Print) Comparative Study Evaluation Studies Journal Article Research Support, Non-U.S. Gov't Validation Studies.

[14] M. Markl, J. Leupold, O. Bieri, K. Scheffler, and J. Hennig, "Double average parallel steady-state free precession imaging: optimized eddy current and transient oscillation compensation," *Magn Reson Med*, vol. 54, pp. 965–74, 2005. 0740-3194 (Print) Evaluation Studies Journal Article Research Support, Non-U.S. Gov't.

[15] M. Markl, M. T. Alley, C. J. Elkins, and N. J. Pelc, "Flow effects in balanced steady state free precession imaging," *Magn Reson Med*, vol. 50, pp. 892–903, 2003. 0740-3194 (Print) Journal Article.

[16] N. J. Pelc, M. A. Bernstein, A. Shimakawa, and G. H. Glover, "Encoding strategies for three-direction phase-contrast mr imaging of flow," *Journal of Magnetic Resonance Imaging: JMRI*, vol. 1, pp. 405–13. PMID: 1790362.

[17] J. Bock, B. W. Kreher, J. Hennig, and M. Markl, *Optimized Pre-Processing of Time-Resolved 2D and 3D Phase Contrast MRI Data*. 2007.

[18] M. A. Bernstein, X. J. Zhou, J. A. Polzin, K. F. King, A. Ganin, N. J. Pelc, and G. H. Glover, "Concomitant gradient terms in phase contrast mr: analysis and correction," *Magn Reson Med*, vol. 39, pp. 300–8, 1998. Bernstein, M A Zhou, X J Polzin, J A King, K F Ganin, A Pelc, N J Glover, G H United states Magnetic resonance in medicine : official journal of the Society of Magnetic Resonance in Medicine / Society of Magnetic Resonance in Medicine Magn Reson Med. 1998 Feb;39(2):300-8.

[19] J. E. Jordan, N. J. Pelc, and D. R. Enzmann, "Velocity and flow quantitation in the superior sagittal sinus with ungated and cine (gated) phase-contrast mr imaging," *Journal of Magnetic Resonance Imaging: JMRI*, vol. 4, pp. 25–28, Feb. 1994. PMID: 8148552.

[20] V. M. Haughton, F. R. Korosec, J. E. Medow, M. T. Dolar, and B. J. Iskandar, "Peak systolic and diastolic csf velocity in the foramen magnum in adult patients with chiari i malformations and in normal control participants," *AJNR Am J Neuroradiol*, vol. 24, pp. 169–76, 2003. 0195-6108 (Print) Journal Article.

[21] A. Frydrychowicz, J. T. Winterer, M. Zaitsev, B. Jung, J. urgen Hennig, M. Langer, and M. Markl, "Visualization of iliac and proximal femoral artery hemodynamics using time-resolved 3d phase contrast mri at 3t," *Journal of Magnetic Resonance Imaging: JMRI*, vol. 25, pp. 1085–1092, May 2007. PMID: 17427916.

[22] M. A. Bernstein, A. Shimakawa, and N. J. Pelc, "Minimizing te in moment-nulled or flow-encoded two- and three-dimensional gradient-echo imaging," *J Magn Reson Imaging*, vol. 2, pp. 583–8, 1992. 1053-1807 (Print) Journal Article.

[23] P. Thunberg, M. Karlsson, and L. W. om, "Accuracy and reproducibility in phase contrast imaging using sense," *Magnetic Resonance in Medicine: Official Journal of the Society of Magnetic Resonance in Medicine / Society of Magnetic Resonance in Medicine*, vol. 50, pp. 1061–1068, Nov. 2003. PMID: 14587017.

[24] C. Baltes, S. Kozerke, M. S. Hansen, K. P. Pruessmann, J. Tsao, and P. Boesiger, "Accelerating cine phase-contrast flow measurements using k-t blast and k-t sense," *Magn Reson Med*, vol. 54, pp. 1430–8, 2005. 0740-3194 (Print) Clinical Trial Journal Article Research Support, Non-U.S. Gov't.

[25] T. Gu, F. R. Korosec, W. F. Block, S. B. Fain, Q. Turk, D. Lum, Y. Zhou, T. M. Grist, V. Haughton, and C. A. Mistretta, "Pc vipr: a high-speed 3d phase-contrast method for flow quantification and high-resolution angiography," *AJNR Am J Neuroradiol*, vol. 26, pp. 743–9, 2005. 0195-6108 (Print) Journal Article Research Support, U.S. Gov't, P.H.S.

[26] I. Marshall, "Feasibility of k-t blast technique for measuring "seven-dimensional" fluid flow," *J Magn Reson Imaging*, vol. 23, pp. 189–96, 2006. 1053-1807 (Print) Comparative Study Journal Article Research Support, Non-U.S. Gov't.

[27] M. Markl, F. P. Chan, M. T. Alley, K. L. Wedding, M. T. Draney, C. J. Elkins, D. W. Parker, R. Wicker, C. A. Taylor, R. J. Herfkens, and N. J. Pelc, "Time-resolved three-dimensional phase-contrast mri," *J Magn Reson Imaging*, vol. 17, pp. 499–506, 2003. 1053-1807 (Print) Journal Article Research Support, Non-U.S. Gov't Research Support, U.S. Gov't, P.H.S.

[28] A. A. Linninger, M. Xenos, D. C. Zhu, M. R. Somayaji, S. Kondapalli, and R. D. Penn, "Cerebrospinal fluid flow in the normal and hydrocephalic human brain," *IEEE Trans Biomed Eng*, vol. 54, pp. 291–302, 2007. Linninger, Andreas A Xenos, Michalis Zhu, David C Somayaji, MahadevaBharath R Kondapalli, Srinivasa Penn, Richard D Research Support, Non-U.S. Gov't United States IEEE transactions on bio-medical engineering IEEE Trans Biomed Eng. 2007 Feb;54(2):291-302.

# Chapter 5

# On optimal flow encoding for three-directional phase contrast sequences

Results from this chapter were presented at the 17$^{th}$ ISMRM Meeting (Honolulu, HI, 2009), electronic poster #4537

## 5.1 Introduction

Most three-directional phase contrast sequences encode flow with a scheme called "4-point balanced", first proposed by Pelc et al in [1] (see also 1.4.1.1), because it holds the highest signal-to noise ratio achievable with 4 scans, and it is independent of flow direction.

This encoding scheme uses 4 steps to simultaneously encode flow from all three spatial directions, and single components of the velocity vector are then retrieved through linear combinations of the four scans. In cardiac-gated acquisitions, the 4 steps are usually acquired in an interleaved manner during a single cardiac phase, thus limiting the temporal resolution to 4xTR, in the best case. In other situations, as for the phase contrast bSSFP sequence presented in chapter 4, the temporal resolution might be limited by other factors and be even lower; or it can be desirable to acquire more k-space lines during one cardiac cycle in order to reduce total scan time.

In this chapter it will be shown that this acquisition scheme is equivalent to a low-pass filtering of the velocity waveform, followed by a 4x downsampling. To compensate for this effect, a novel method of reconstructing the phase contrast images based on view sharing along the velocity direction is presented. The proposed technique eliminates the downsampling step and provides a more accurate reconstruction of the signal. In vivo acquisitions with low temporal resolution are performed and compared with a fully sampled velocity waveform.

## 5.2 Theory

In a phase-contrast acquisition the phase component of the MR signal is proportional to the velocity of the moving isochromat and to the first moment of the applied gradients. In order to compensate for static phase errors, a reference scan or a "two-sided" acquisition scheme, where encoding is performed using bipolar gradients with opposite first moments, is used [2].

In the case of three-directional acquisitions, the optimal encoding scheme consists of 4 steps, sensitive to motion in all directions, with changing polarities so that the three components are linearly separable from the four scans. At the end of the acquisition, every component of the velocity vector is encoded twice with positive polarity, and twice with negative polarity. The acquisition scheme is shown in figure 5.1*a*.

The reconstruction of the velocities along each axis is obtained by the following equations:

$$\begin{aligned} v_x &= ((v_1+v_2)-(v_0+v_3))/4 \\ v_y &= ((v_2+v_3)-(v_0+v_1))/4, \\ v_z &= ((v_1+v_3)-(v_0+v_2))/4 \end{aligned} \tag{5.1}$$

where $v_x$, $v_y$ and $v_z$ are the velocities along the readout, phase and slice selection direction respectively, and $v_0$, $v_1$, $v_2$ and $v_3$ are the velocities corresponding to the phase values acquired in each step.

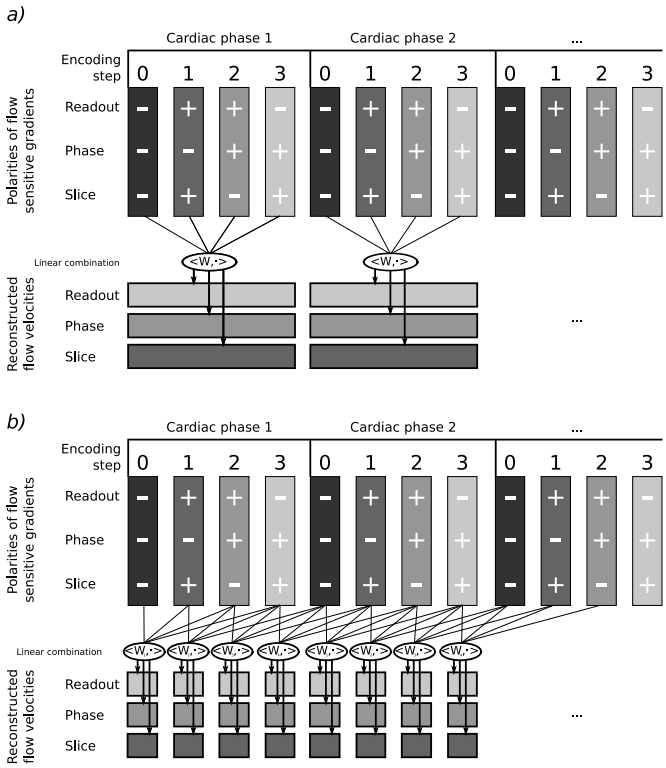


Figure 5.1: Encoding schemes for a three-directional flow encoding sequence. A "+" sign represents positive encoding moment; a "-" sign represents negative encoding moment. *a)* Acquisition scheme with conventional reconstruction; *b)* Acquisition scheme with "view sharing" reconstruction.

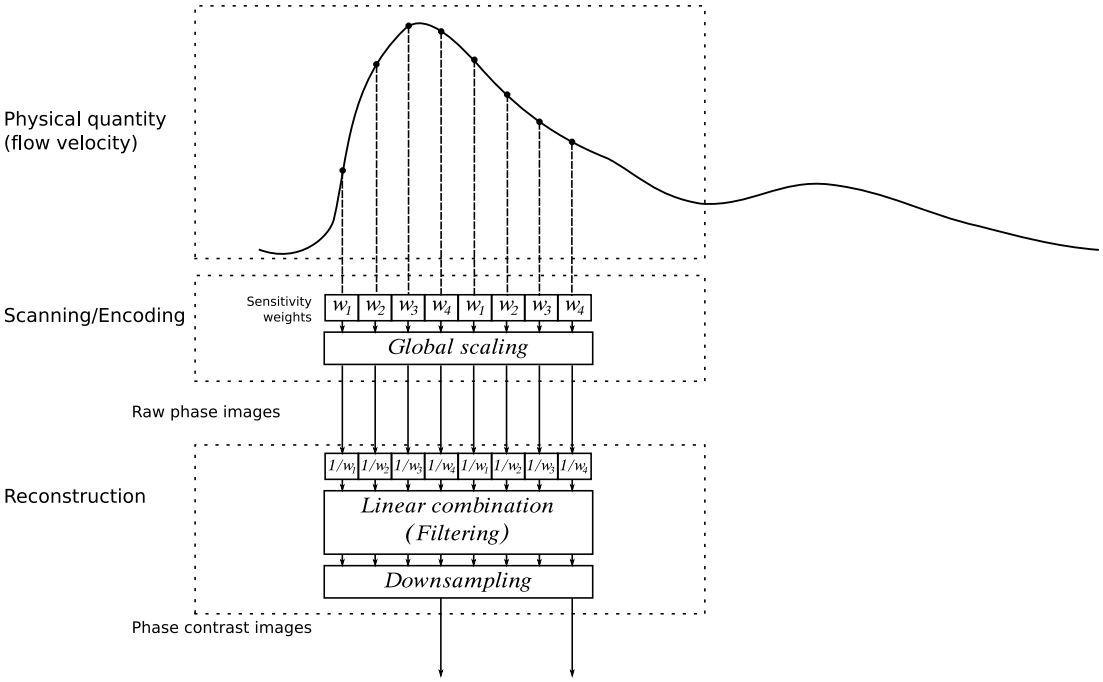


Figure 5.2: Encoding of velocity from a phase contrast sequence represented as a FIR filtering followed by a downsampling step.

The coefficients by which each encoding step is multiplied serve the purpose of compensating for the different polarity of the flow-sensitizing gradients. From a signal processing point of view, this sum corresponds to a simple 4-tap finite impulse response (FIR) low-pass filtering of each component, where all the filter coefficients are set to 1/4. A single image is retrieved from the sum of four encoding steps, and this corresponds to a downsampling of the signal by a factor of four. A schematic representation of the acquisition method is shown in fig. 5.2.

The frequency response of the filter is shown in fig. 5.3. Attenuation is -3.7dB at 0.25 normalized frequency, and -11.3dB in the stop-band. The downsampling cuts the available band at 0.25 normalized frequency, therefore the signal components at higher frequencies will cause aliasing noise in the resulting waveform.

In order to avoid the downsampling, a "sliding window" approach to velocity waveform reconstruction can be used: the first sample is obtained from the four encoding steps from the first cardiac phase, then the second, third and fourth steps from the first phase and the first step from the second phase are used to produce the second sample, and so on (fig. 5.1*b*). This is equivalent to filtering the signal with the aforementioned filter, while maintaining same sampling rate.

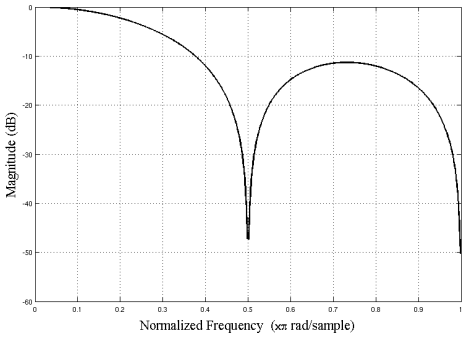


Figure 5.3: Filter frequency response.

## 5.3 Acquisitions

A pulse-gated phase-contrast scan of an axial slice of the neck was acquired in a healthy volunteer on a whole-body 3T scanner (Magnetom Verio, Siemens Healthcare, Erlangen, Germany) with a 12-channel head coil and dedicated neck coil. A through-plane 2D SPGR sequence was used (Venc: 100cm/s, matrix size 256x216x1, resolution 0.94x0.94x5 $mm^3$, TR/TE 9.0/5.5 ms, temporal resolution 18 ms). A slower three-directional acquisition was acquired with a custom SPGR implementing the 4-point balanced encoding scheme (same slice and scanning parameters, temporal resolution 72 ms). Reconstruction was performed with the "standard" and with the "time shared" algorithms. A region of interest was placed on the left internal carotid artery, and time course of the pixel intensity of the phase images across the different datasets (high temporal resolution, standard and time shared reconstruction) was compared.

## 5.4 Results

The downsampling caused the missing of the sharper velocity peak in the waveform, which was more accurately followed by the view-shared reconstruction, as shown in figure 5.4. Low-pass effect is clearly visible in the lower temporal resolution, where the slope of the curve is much less steep than the high-resolution waveform. In principle, some information could be retrieved by interpolating the downsampled signal, but the aliasing noise added by the inefficient low-pass filtering would still be present, and the higher-frequency components of the original signal could not be retrieved.

## 5.5 Discussion

In this chapter, a novel method for the reconstruction of phase contrast images was presented. This method is applicable with all sequences that use a four-point balanced acquisition scheme, because information about the original waveform are acquired at

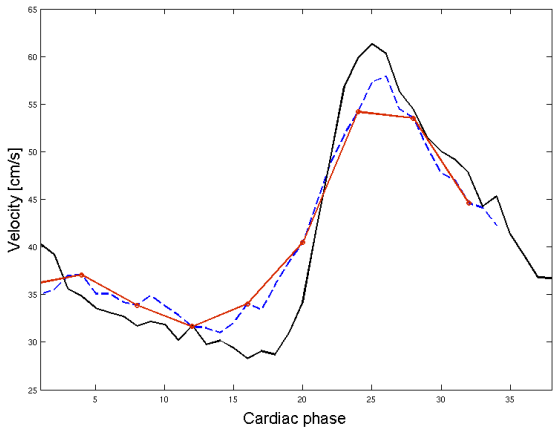


Figure 5.4: Flow waveform. Black: high-temporal-resolution acquisition; dashed-blue: reconstruction with view-sharing; red: standard reconstruction.

every encoding step. In this sequences, the traditional method of reconstruction of the phase contrast images is equivalent to a low-pass filtering followed by a downsampling of the signal.

Avoiding the downsampling is an operation that comes at no additional cost after acquiring the flow-encoded images, as it can be achieved by the proposed simple reconstruction algorithm. If the attenuation of the higher-frequency components of the signal is not acceptable, a correction through inverse filtering could be applied, but this would come at the cost of possible amplification of noise.

This reconstruction method is especially beneficial when high temporal resolution is not achievable by the sequence, because of restrictions in the total acquisition time (as could happen in breathhold acquisitions), or because of other restrictions posed by the sequence design itself (as the case of the bSSFP sequence presented in chapter 4).

## References

[1] N. J. Pelc, M. A. Bernstein, A. Shimakawa, and G. H. Glover, "Encoding strategies for three-direction phase-contrast mr imaging of flow," *Journal of Magnetic Resonance Imaging: JMRI*, vol. 1, pp. 405–13. PMID: 1790362.

[2] M. A. Bernstein, A. Shimakawa, and N. J. Pelc, "Minimizing te in moment-nulled or flow-encoded two- and three-dimensional gradient-echo imaging," *J Magn Reson Imaging*, vol. 2, pp. 583–8, 1992. 1053-1807 (Print) Journal Article.

# Chapter 6

# Cerebrospinal fluid flow

Results from this chapter were presented at:

- 25$^{th}$ ESMRMB Meeting (Valencia, Spain, 2008), oral presentation #179 (healthy volunteers).
- 17$^{th}$ ISMRM Meeting (Honolulu, HI, 2009), electronic poster #3348 (patient results).

## 6.1 Introduction

Cerebrospinal fluid (CSF) flow in the ventricular system and subarachnoid space presents complex dynamics that are yet to be fully understood by the scientific community. Obstructions in the outflow path of the fluid produced inside the ventricles lead to compression of the brain parenchyma and to conditions that can significantly impact the quality of life of the patient, like obstructive hydrocephalus and Chiari malformation. Also in the absence of obstructions, which is the case of normal pressure hydrocephalus (NPH), CSF flow can reflect pathological conditions, and the study of the dynamics can improve the knowledge of this class of pathologies [1, 2].

Magnetic resonance imaging (MRI) is often the technique of choice for the study of the CNS in general and of CSF in particular, because it is non-invasive, holds high soft-tissue contrast and can provide some functional details about flow dynamics. However, due to the long T1 relaxation time of CSF, and due to the slow velocity of the fluid, conventional MR flow quantification techniques were never used for direct measurement of three dimensional flow patterns.

The most common approach present in the literature is to and measure through-plane flow in one location [3] and to apply computational fluid dynamics to MRI anatomical data.

In this chapter, preliminary results of in vivo three-dimensional flow quantification of CSF in the ventricular system are presented. This acquisitions were performed using the bSSFP sequence presented in chapter 4, which presents a high SNR even for three-dimensional acquisitions. The results from healthy volunteers are shown and compared to a case of three-ventricular obstructive hydrocephalus.

## 6.2 Materials and methods

Three healthy volunteers and one patient suffering from a long standing three-ventricular hydrocephalus were included in the study. The patient was scanned twice: before surgery and after a ventriculostomy that opened the lamina terminalis, the treatment of choice for this condition [4].

### 6.2.1 MRI acquisitions

The 3D time-resolved phase contrast bSSFP sequence presented in chapter 4 was used for the scan of all subjects.

The scanned region was a sagittal slab containing the third ventricle, the aqueduct of Sylvius, the foramina Monroi and part of the lateral ventricles. The magnetic field was manually shimmed in order to obtain less than 20Hz of total signal bandwidth in the region of interest. The chosen scanning parameters were: Venc 10cm/s, number of averages 2, TR/TE 14/7 ms, resolution 1x1x1.5mm$^3$, bandwidth 965Hz/px. Generalized autocalibrating partially parallel acquisitions (GRAPPA) [5] algorithm for parallel imaging with an acceleration factor of 2 was used, in order to compensate for the scan

time penalty deriving from the averaging. Due to the characteristics of the sequence, the time footprint for data acquisition was 8*TR (112ms). The effective time resolution of the final dataset was reduced to 2*TR (28ms), by implementing the view sharing approach of the flow encoding steps shown in chapter 5. Prospective cardiac gating was used, and the number of acquired cardiac phases was adjusted in order to have maximum possible coverage of the cardiac cycle. Total scan time was around 20 minutes, with small variations depending on the heart rate of the subject.

### 6.2.2 Image preprocessing

The phase contrast images acquired were preprocessed using a software tool [6] developed in Matlab (The Mathworks, Natick, MA). Noise masking, based on magnitude intensity, was applied and linear phase drifts and concomitant field effects were compensated by estimating the background phase from stationary regions, fitting it to a 2nd order 2D polynomial, and subtracting it from the phase images [7].

The tool converted the modified images into three-dimensional datasets for import into commercial 3D visualization software for engineering (Ensight, CEI, Apex, NC).

### 6.2.3 Data visualization

The dataset was visually inspected using 3D visualization software, and two kind of representation of the velocity field were obtained:

1. *Streamlines*: lines showing the ideal path of massless particles released in the ventricular space, under the assumption that the velocity field is constant in time. They give a representation of the velocity field at each cardiac phase.

2. *Pathlines*: lines showing the ideal path of massless particles in a time-resolved velocity field. These lines can be animated in order to depict the actual behavior of a particle released in the ventricular space, and can be visualized as videos.

Emitter planes for these particles were placed inside the third ventricle, cutting it axially, to visualize the flow patterns of the CSF inside the ventricle itself, and in the foramina of Monro and in the fourth ventricle to visualize feeding flow inside the third ventricle.

## 6.3 Results

### 6.3.1 Healthy volunteers

he results showed the presence of two counter-rotating vortices in the third ventricle, which keep the same direction of rotation throughout the whole cardiac cycle, and are alternatively fed from the foramina of Monro (during systole, fig. 6.1 - left) and the aqueduct of Sylvius (during diastole, fig. 6.1 - right). Peak flow velocities are up to 5 cm/s in the aqueduct, but flow pulsatility is very high, resulting in little net flow in the cranio-caudal direction, which is compatible with the observation of physiological CSF production.

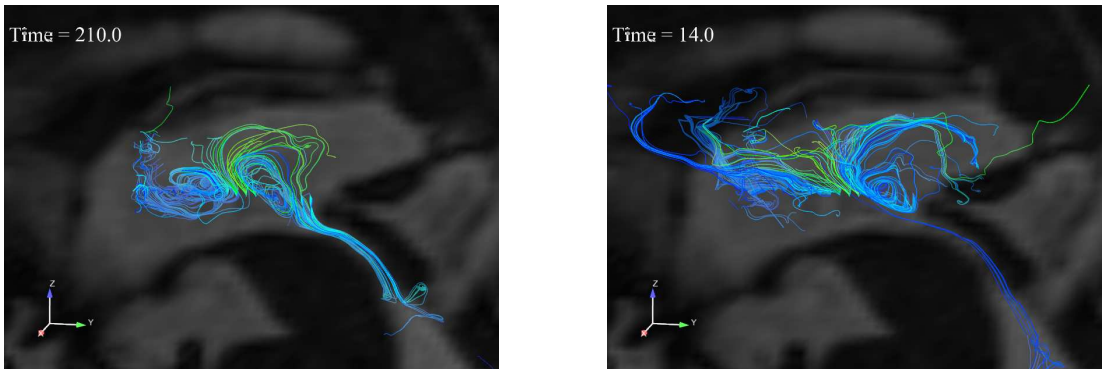


Figure 6.1: Flow patterns in healthy volunteer: *left* - systole; *right* - diastole. Time shown is in ms after R peak.

Figure 6.2: Schematic model of flow in the third ventricle: *left* - systole; *right* - diastole.

A proposed model of CSF flow for healthy volunteers is presented in fig. 6.2.

### 6.3.2 Patient

Despite the absence of any obstruction visible on T2-weighted anatomical imaging, no flow through the aqueduct was observed. This finding was confirmed by the endoscopic investigation that was performed after the imaging, and revealed obstructive membranes. The complex flow patterns within the third ventricle visible in the healthy volunteers were not present, merely a slow pulsation in the cranio-caudal direction, with no significant net flow was visualized. Flow was traced to transverse the floor of the third ventricle, indicating a spontaneous ventriculostomy, but not large enough to compensate for the production of CSF (figure 6.3 - left). After surgery, the rupture of the the lamina terminalis is confirmed by higher flow from the third ventricle to the

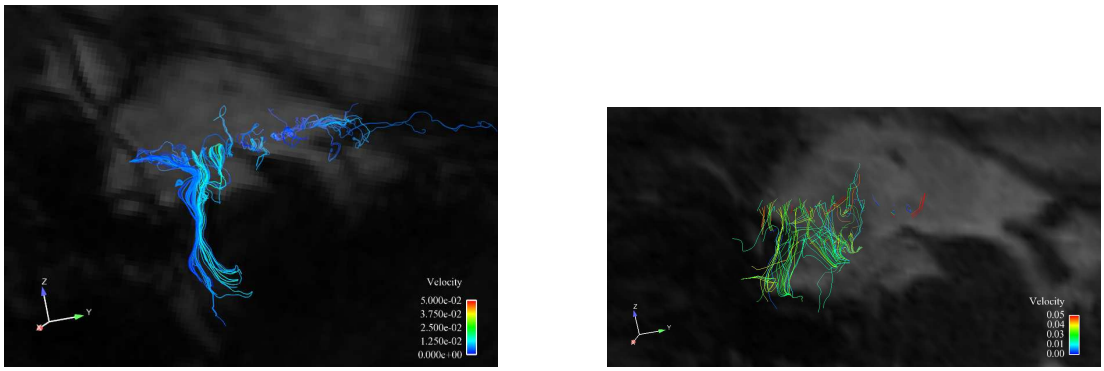


Figure 6.3: Systolic flow in the third ventricle of an obstructive hydrocephalus patient before surgery (*left*) and after surgery (*right*).

extraventricular space (figure 6.3 - right).

## 6.4 Discussion

Three-dimensional, time-resolved, three-directional flow-sensitive balanced SSFP sequence was able to produced high SNR and enabled a comprehensive study of flow patterns and velocities. The comparison of the three-dimensional flow patterns between healthy volunteers and a patient with hydrocephalus revealed significant differences that might become helpful in the definition of the diagnosis and the therapy. In particular, the spontaneous rupture of the lamina terminalis was a finding that other imaging technique would not have shown, but it is reported to happen in patients with similar conditions [8–10].

The results presented in this chapter are still preliminary and based on a very restricted cohort of subjects, but the techniques here presented offer the possibility of starting a more complete study of the various forms of hydrocephalus and different pathologies related to CSF flow.

## References

[1] G. Petrella, M. Czosnyka, N. Keong, J. D Pickard, and Z. Czosnyka. How does csf dynamics change after shunting? *Acta Neurol Scand*, 2008. Journal article Acta neurologica Scandinavica Acta Neurol Scand. 2008 May 27.

[2] H. Williams. The venous hypothesis of hydrocephalus. *Med Hypotheses*, 70:743–7, 2008. Williams, Helen Scotland Medical hypotheses Med Hypotheses. 2008;70(4):743-7. Epub 2007 Oct 4.

[3] V. Kurtcuoglu, M. Soellinger, P. Summers, K. Boomsma, D. Poulikakos, P. Boesiger, and Y. Ventikos. Computational investigation of subject-specific cerebrospinal fluid flow in the third ventricle and aqueduct of sylvius. *J Biomech*, 40:1235–45, 2007.

[4] Michael D Jenkinson, Caroline Hayhurst, Mohammed Al-Jumaily, Jothy Kandasamy, Simon Clark, and Conor L Mallucci. The role of endoscopic third ventriculostomy in adult patients with hydrocephalus. *Journal of Neurosurgery*, 110:861–866, May 2009. PMID: 19284240.

[5] M. A Griswold, P. M Jakob, R. M Heidemann, M. Nittka, V. Jellus, J. Wang, B. Kiefer, and A. Haase. Generalized autocalibrating partially parallel acquisitions (grappa). *Magn Reson Med*, 47:1202–10, 2002.

[6] J. Bock, B. W Kreher, J. Hennig, and M. Markl. *Optimized Pre-Processing of Time-Resolved 2D and 3D Phase Contrast MRI Data*. 2007.

[7] M. A Bernstein, X. J Zhou, J. A Polzin, K. F King, A. Ganin, N. J Pelc, and G. H Glover. Concomitant gradient terms in phase contrast mr: analysis and correction. *Magn Reson Med*, 39:300–8, 1998.

[8] A Alonso, D Taboada, J A Alvarez, C Paramo, and M Vila. Spontaneous ventriculostomy and ventricular diverticulum. *Radiology*, 133:651–654, December 1979. PMID: 315578.

[9] R Bhatia, A K Banerji, and M Rao. Spontaneous rupture of the third ventricle in obstructive hydrocephalus: a radiographic diagnosis. *Acta Neurochirurgica*, 39:159–165, 1977. PMID: 304657.

[10] Amit Parmar, Kristian Aquilina, and Michael R Carter. Spontaneous third ventriculostomy: definition by endoscopy and cerebrospinal fluid dynamics. *Journal of Neurosurgery*, 2009. PMID: 19199451.

# Chapter 7

# Summary and conclusion

The main goal of this thesis was to present novel methods for the study of physiological and pathological conditions associated to intracranial flow. Flow inside the central nervous system occurs in two compartments: the blood, confined to the vessels and the microvasculature, and the cerebrospinal fluid, which circulates in the ventricular and subarachnoid space.

There is a physiological link between CSF and blood, both from a biochemical point of view, as the CSF is produced by filtration of the blood and reabsorbed in the venous system, and from a mechanical point of view, as the blood pulsation inside the brain drives the pulsation of the CSF itself. Therefore, blood and CSF flow dynamics are deeply linked.

## 7.1 Blood flow

In order to study the blood flow, magnetic resonance angiography is a widely used technique, both by means of non-contrast-enhanced sequences and first-pass gadolinium-enhanced angiography. In this thesis, the focus was set on time-resolved contrast-enhanced angiography, because it is a widely used method for the evaluation of blood dynamics [1–10], able to identify many relevant pathologies.

In order to improve the image quality, some algorithm able to separate the arteriogram and the venogram from the acquired datasets is important [11]. In chapter 2, a novel algorithm to achieve this separation, termed "double-reference cross-correlation", was introduced. This method is based on the analysis of the time course of the signal intensity of each voxel in the acquired dataset, which reflects the passage of the contrast agent bolus at the observed location. This time course is then compared both to an arterial and a venous reference time courses, by means of a cross-correlation analysis. The cross-correlation values are then mapped onto a two-dimensional vector space, which is subsequently color-coded by an adapting red-green-blue colormap that depends on the mutual correlation of the reference time courses. The final result of color-coding is a single three-dimensional RGB dataset, which depicts the arteriogram and the venogram at the same time, by conventionally assigning a "red" color to the vessels identified as arteries, and a "blue" color to vessels identified as veins. This representation is able to provide diagnostically useful information in one single dataset, without the need to separately analyze and compare the arteriogram and venogram. Moreover, it can easily highlight potentially pathological conditions, as mixing of arterial and venous flow. The method was validated quantitatively on normal datasets, and was proven to be superior in quality with respect to the established cross-correlation method [12], and qualitatively on datasets from healthy and pathological subjects, and good diagnostic quality was achieved in both cases.

In order to improve the performance, and to remove the dependance on a manual choice of reference time courses, a clustering-based automatic reference selection method was introduced in chapter 3. This technique relies on a modified version of the *k-means* algorithm for unsupervised clustering. The results obtained by separating arteries and veins with the automatic reference selection were found to be equivalent

to the separation based on manual identification of reference. The usage of the double-reference cross-correlation algorithm together with automatic reference selection is able to improve the workflow of time-resolved contrast enhanced angiography examinations, allowinga direct implementation of the method on the scanner workstation in the future.

The novel flow quantification sequence introduced in chapter 4, especially when coupled with the reconstruction method presented in chapter 5 to enhance the temporal resolution, can also be used for quantification of flow inside the vessels. Nevertheless, when inflow-enhancement effects can be exploited, standard sequences based on radiofrequency-spoiled gradient echo [13] can be more suitable for this purpose because of inherently shorter TRs and therefore higher temporal resolution. However, relaxation characteristics of fluids make the bSSFP-based sequence a valid alternative from a signal-to-noise point of view, when inflow enhancement effects are not available, as it is mostly the case of CSF flow.

## 7.2 CSF flow

Cerebrospinal fluid flow is still an open question for the scientific community. Several studies [14–19] have been trying to provide a flow model, based on two-dimensional velocity acquisitions, anatomical information, and computational fluid dynamics. A direct in vivo measurement of the three-dimensional flow patterns is proven to be difficult due to the peculiar relaxation characteristics of this fluid, which shows virtually no signal on conventional $T_1$-weighted sequences.

For these reasons, a novel method based on balanced SSFP, which shows a $T_2/T_1$ contrast, has been introduced in this thesis. The characteristic of this sequence is that the transversal magnetization is refocused at the end of TR, building a steady-state condition, which results in a very strong signal received from CSF at short repetition times. High signal-to-noise allows high accuracy in the velocity measurements and also allows the usage of acceleration techniques to reduce acquisition times.

Chapter 4 describes the implementation of this three-dimensional, three-directional, time-resolved phase contrast balanced SSFP sequence. Because of the sensitivity of the steady state to dephasing effects due to flow and to eddy currents, special measures needed to be taken in order to avoid artifacts arising from these issues. Flow compensation at TR was implemented, in order to compensate for flow-related spin dephasing, which causes instability in the steady-state [20, 21], and, to achieve this consistently for every k-space line, a custom iterative algorithm for the calculation of gradient shapes was introduced. Eddy currents issues were addressed by the implementation of two different strategies: k-space pairing [22] and double averaging [23]. The double averaging approach was finally chosen, as it provided better image quality and allowed easier implementation of arbitrary k-space trajectories, useful for enabling parallel imaging methods.

The applicability to CSF acquisition to healthy volunteers and patients was shown in chapters 4 and 6. The preliminary results from volunteers show that the flow dynamics of CSF inside the ventricular system can be very complex, and pathologies can potentially

alter them. In particular, the measurements allowed the identification of a simplified circulation model of CSF inside the third ventricle, consisting of two counter-rotating vortices, whose rotation direction does not change throughout the cardiac cycle, and which are fed from the foramina Monroi during systole, and from the aqueduct of Sylvius during diastole.

In the clinical environment, the most important pathology to be focused on is hydrocephalus, which presents itself as an abnormal enlargement of the ventricles with subsequent compression of the cerebral parenchyma, and severe disability. It is believed that hydrocephalus, when not linked to obstructions in the normal CSF outflow channels (ie aqueduct of Sylvius, foramen magnum), can be caused by a potential link between venous outflow, stiffness of the brain parenchyma and CSF production [24]. All these parameters can be directly or indirectly evaluated by the techniques presented in this thesis, possibly linked with anatomical information and computational fluid dynamics.

## 7.3 Outlook

Future work will be focused on bringing the methods proposed in this thesis to a clinical level, so that physicians will benefit from valuable additional information for the diagnosis and follow-up of patients. The double-reference cross-correlation technique could be directly implemented on the scanner workstation, and could be a valuable addition to the conventional observation of time-resolved CE-MRA datasets at virtually no additional cost, as it can effectively highlight arteriovenous malformations and vessels with mixed arterial and venous blood.

Three-dimensional flow measurements would require an extension of the current clinical protocols, and a penalty for this is the long scan time required to obtain a dataset. However, a flow examination can add valuable information in the diagnosis of obstructive hydrocephalus, and also as a non-invasive tool for surgery follow-up, after a ventriculostomy or a ventricular shunting.

The techniques presented in this thesis will also be used for more basic clinical research: the mechanics of CSF flow and hydrocephalus, and the relationship between CSF and blood, are not yet fully understood and both time-resolved angiography data and quantitative flow measurement could be helpful for increasing the knowledge of this system. For this purpose, a large cohort of healthy volunteers and patients will be needed for the determination of the whole spectrum of possible flow patterns, and for the determination of how specific flow patterns can be linked to physiological o pathological parameters.

Quantitative flow measurements could also be acquired together with high-resolution anatomical datasets, and computational fluid dynamics analysis could be performed, using the flow data as boundary conditions, in order to achieve high spatial and temporal resolutions.

In conclusion, this thesis aimed to offer a set of new tools to be applied to the analysis of intracranial flow, with the potential to be directly useful both in clinics and in basic research. The hope is that my work will in the future be able to expand the

knowledge and the possibility of diagnosis for important diseases and malformations as the one cited, and improve the chances of recovery for patients.

# References

[1] T. Lei, J. K. Udupa, P. K. Saha, D. Odhner, R. Baum, S. K. Tadikonda, and E. K. Yucel, "3d mra visualization and artery-vein separation using blood-pool contrast agent ms-325," *Acad Radiol*, vol. 9 Suppl 1, pp. S127–33, 2002. 1076-6332 (Print) Journal Article.

[2] S. Meckel, R. Mekle, C. Taschner, S. Haller, K. Scheffler, E. W. Radue, and S. G. Wetzel, "Time-resolved 3d contrast-enhanced mra with grappa on a 1.5-t system for imaging of craniocervical vascular disease: initial experience," *Neuroradiology*, vol. 48, pp. 291–9, 2006. 0028-3940 (Print) Journal Article.

[3] S. Meckel, M. Maier, D. S. Ruiz, H. Yilmaz, K. Scheffler, E. W. Radue, and S. G. Wetzel, "Mr angiography of dural arteriovenous fistulas: diagnosis and follow-up after treatment using a time-resolved 3d contrast-enhanced technique," *AJNR Am J Neuroradiol*, vol. 28, pp. 877–84, 2007. 0195-6108 (Print) Clinical Trial Comparative Study Journal Article.

[4] C. A. Mistretta, T. M. Grist, F. R. Korosec, R. Frayne, D. C. Peters, Y. Mazaheri, and T. J. Carrol, "3d time-resolved contrast-enhanced mr dsa: advantages and tradeoffs," *Magn Reson Med*, vol. 40, pp. 571–81, 1998. 0740-3194 (Print) Journal Article.

[5] M. R. Prince, "Contrast-enhanced mr angiography: theory and optimization," *Magn Reson Imaging Clin N Am*, vol. 6, pp. 257–67, 1998. 1064-9689 (Print) Journal Article.

[6] M. R. Prince and J. F. Meaney, "Expanding role of mr angiography in clinical practice," *Eur Radiol*, vol. 16 Suppl 2, pp. B3–8, 2006. 0938-7994 (Print) Journal Article Review.

[7] K. Tsuchiya, C. Aoki, A. Fujikawa, and J. Hachiya, "Three-dimensional mr digital subtraction angiography using parallel imaging and keyhole data sampling in cerebrovascular diseases: initial experience," *Eur Radiol*, vol. 14, pp. 1494–7, 2004. 0938-7994 (Print) Journal Article.

[8] K. Tsuchiya, C. Aoki, S. Katase, and J. Hachiya, "Mr digital subtraction angiography with three-dimensional data acquisition in the diagnosis of brain tumors: preliminary experience," *Magn Reson Imaging*, vol. 22, pp. 149–53, 2004. 0730-725X (Print) Journal Article.

[9] E. Unlu, O. Temizoz, S. Albayram, H. Genchellac, M. K. Hamamcioglu, I. Kurt, and M. K. Demir, "Contrast-enhanced mr 3d angiography in the assessment of brain avms," *Eur J Radiol*, 2006. 0720-048X (Print) Journal article.

[10] S. G. Wetzel, D. Bilecen, P. Lyrer, G. Bongartz, E. Seifritz, E. W. Radue, and K. Scheffler, "Cerebral dural arteriovenous fistulas: detection by dynamic mr projection angiography," *AJR Am J Roentgenol*, vol. 174, pp. 1293–5, 2000. 0361-803X (Print) Journal Article.

[11] M. Miyazaki and V. S. Lee, "Nonenhanced mr angiography," *Radiology*, vol. 248, pp. 20–43, July 2008. PMID: 18566168.

[12] M. Bock, S. O. Schoenberg, F. Floemer, and L. R. Schad, "Separation of arteries and veins in 3d mr angiography using correlation analysis," *Magn Reson Med*, vol. 43, pp. 481–7, 2000. 0740-3194 (Print) Journal Article.

[13] M. Markl, F. P. Chan, M. T. Alley, K. L. Wedding, M. T. Draney, C. J. Elkins, D. W. Parker, R. Wicker, C. A. Taylor, R. J. Herfkens, and N. J. Pelc, "Time-resolved three-dimensional phase-contrast mri," *Journal of Magnetic Resonance Imaging: JMRI*, vol. 17, pp. 499–506, Apr. 2003. PMID: 12655592.

[14] S. Gupta, M. Soellinger, P. Boesiger, D. Poulikakos, and V. Kurtcuoglu, "Three-dimensional computational modeling of subject-specific cerebrospinal fluid flow in the subarachnoid space," *Journal of Biomechanical Engineering*, vol. 131, p. 021010, Feb. 2009. PMID: 19102569.

[15] L. Howden, D. Giddings, H. Power, A. Aroussi, M. Vloeberghs, M. Garnett, and D. Walker, "Three-dimensional cerebrospinal fluid flow within the human ventricular system," *Computer Methods in Biomechanics and Biomedical Engineering*, vol. 11, pp. 123–133, Apr. 2008. PMID: 18297492.

[16] V. Kurtcuoglu, M. Soellinger, P. Summers, K. Boomsma, D. Poulikakos, P. Boesiger, and Y. Ventikos, "Computational investigation of subject-specific cerebrospinal fluid flow in the third ventricle and aqueduct of sylvius," *J Biomech*, vol. 40, pp. 1235–45, 2007.

[17] A. A. Linninger, M. Xenos, D. C. Zhu, M. R. Somayaji, S. Kondapalli, and R. D. Penn, "Cerebrospinal fluid flow in the normal and hydrocephalic human brain," *IEEE Trans Biomed Eng*, vol. 54, pp. 291–302, 2007.

[18] A. Linninger, B. Sweetman, and R. Penn, "Normal and hydrocephalic brain dynamics: The role of reduced cerebrospinal fluid reabsorption in ventricular enlargement," *Annals of Biomedical Engineering*, Apr. 2009. PMID: 19373558.

[19] R. D. Penn and A. Linninger, "The physics of hydrocephalus," *Pediatric Neurosurgery*, vol. 45, pp. 161–174, May 2009. PMID: 19440003.

[20] M. Markl and N. J. Pelc, "On flow effects in balanced steady-state free precession imaging: pictorial description, parameter dependence, and clinical implications," *J Magn Reson Imaging*, vol. 20, pp. 697–705, 2004. 1053-1807 (Print) Journal Article Research Support, Non-U.S. Gov't Research Support, U.S. Gov't, P.H.S.

[21] M. Markl, M. T. Alley, C. J. Elkins, and N. J. Pelc, "Flow effects in balanced steady state free precession imaging," *Magn Reson Med*, vol. 50, pp. 892–903, 2003. 0740-3194 (Print) Journal Article.

[22] O. Bieri, M. Markl, and K. Scheffler, "Analysis and compensation of eddy currents in balanced ssfp," *Magn Reson Med*, vol. 54, pp. 129–37, 2005. 0740-3194 (Print) Comparative Study Evaluation Studies Journal Article Research Support, Non-U.S. Gov't Validation Studies.

[23] M. Markl, J. Leupold, O. Bieri, K. Scheffler, and J. Hennig, "Double average parallel steady-state free precession imaging: optimized eddy current and transient oscillation compensation," *Magn Reson Med*, vol. 54, pp. 965–74, 2005. 0740-3194 (Print) Evaluation Studies Journal Article Research Support, Non-U.S. Gov't.

[24] H. Williams, "The venous hypothesis of hydrocephalus," *Med Hypotheses*, vol. 70, pp. 743–7, 2008. Williams, Helen Scotland Medical hypotheses Med Hypotheses. 2008;70(4):743-7. Epub 2007 Oct 4.

# Acknowledgment

A PhD thesis is an original work, presented by one candidate. However, achievement in research are never the result of the efforts of one single person. During the years spent working on this project, I received help and support by many people, and I would like to express my gratitude to all of them.

First of all, I need to thank my advisor, Prof. Klaus Scheffler, for his insight and inspiration, and, maybe most importantly, for trusting me and my ideas, even when they sounded strange or hopeless.

I would like to acknowledge all the people who helped me, providing ideas, knowledge, and practical help. These people are:

- all my colleagues of the Radiological Physics group in Basel, for countless hours spent helping, discussing, or just chatting;
- the components of the MR research group lead by Prof. Jürgen Hennig, in Freiburg im Breisgau, and especially Dr. Michael Markl, Jelena Bock and Aurélien Stalder, for an extremely interesting collaboration on flow measurements;
- the clinical partners here in the Basel University Hospital, Dr. Stephan Meckel and Dr. Tilman Schubert, for helping me with patients, volunteers, and for anything actually related to medicine, and the MTRAs, for their help and patience.

I also need to specially acknowledge Dr. Stephan Wetzel, a wonderful collaborator and mentor from "the clinical side": his motivation and enthusiasm for my work were invaluable.

My deepest gratitude to Sunil Patil, more than a colleague and collaborator, he is a loyal friend. I wish we could keep in touch and achieve great things together in the future.

Finally, but not of less importance, I would like to thank all my friends: my "old" friends in Italy, who never forgot me, as I never forgot them; and my "new" friends in Basel, who welcomed me and made me feel at home. And of course the biggest "thank you" goes to Tessa, and to my family, for being there, always.

*Francesco Santini*